Abstract

Reducing the losses of the fluxonium artificial atom

Nicholas Adam Masluk

2012

Fluxonium is a highly anharmonic artificial atom, which makes use of an array of large Josephson junctions to shunt the junction of a Cooper-pair box for protection from charge noise. At microwave frequencies the array forms a "superinductance", a superconducting inductance whose impedance exceeds the resistance quantum $h/(2e)^2 \simeq 6.5$ kOhm. The first excited state transition frequency is widely tunable with flux, covering more than five octaves, yet the second excited state remains well within one octave. This unique spectrum permits a dispersive readout over the entire flux tunable range, in contrast to the flux qubit.

By measuring the energy relaxation time of the qubit over the full range of flux dependent transition energies, it is possible to determine the dominant loss mechanisms, and therefore implement design changes to reduce their contribution. The losses in several fluxonium samples are explored, with progressive improvements made towards reducing capacitive loss, the dominant loss mechanism. Additionally, the detailed characterization of Josephson junction array superinductances is examined.

Reducing the losses of the fluxonium artificial atom

A Dissertation
Presented to the Faculty of the Graduate School
of
Yale University
in Candidacy for the Degree of
Doctor of Philosophy

by
Nicholas Adam Masluk

Dissertation Director: Professor Michel H. Devoret

November, 2012

Contents

List of Figures

List of Tables

List of Symbols

$a, a^\dagger$	photon annihilation and creation operators
c	speed of light in vacuum
C_c	qubit–readout coupling capacitance
C_e	readout external coupling capacitance
C_g	gate capacitance
C_J	junction capacitance
C_l	capacitance per unit length
C_R	readout LC oscillator capacitance
C_S	shunt capacitance
C_x	cross coupling capacitance
C_0	parasitic capacitance to ground
C_Σ	total shunt capacitance
C_σ	total junction shunt capacitance excluding that from coupling capacitors
e	electron charge, qubit first excited state
E_C	charging energy, $E_C = e^2/2C_\Sigma$
E_J	Josephson energy, $E_J = I_c\phi_0 = \Delta R_K G_T/8$
E_L	inductive energy, $E_L = \phi_0^2/L$
E_{SA}	phase slip energy of an array junction
f	qubit second excited state

g	coupling constant, qubit ground state
G	conductance
G_t	tunnel junction conductance
h	Planck's constant
$\hbar$	reduced Planck's constant, $\hbar = h/2\pi$
i	"physicist's" imaginary unit, $i = +\sqrt{-1} = -j$
I	current
I_c	critical current
I_0	current amplitude, zero point fluctuation current
I^+	forward propagating wave current
I^-	backward propagating wave current
j	"engineer's" imaginary unit, $j = -\sqrt{-1} = -i$
k	resonant mode index
k_B	Boltzmann constant
l	resonator state variable
L_A	array inductance
L_c	coupling inductance
L_J	Josephson inductance, $L_J = \phi_0/I_c$
L_l	inductance per unit length
L_R	readout LC oscillator inductance
L_Σ	total shunt inductance
m	fluxon index
n	charge number operator, number of photons
n_g	dimensionless gate potential
n_S	number of photons sampled
P	power

P'	power at room temperature (versus the power at cold seen by the sample)
Q	charge operator
Q_{ext}	external quality factor, also referred to as "coupling" quality factor
Q_{int}	internal quality factor
Q_{tot}	total quality factor, also referred to as "loaded" quality factor, $Q_{\text{tot}}^{-1} = Q_{\text{int}}^{-1} + Q_{\text{ext}}^{-1}$
R_K	resistance quantum, $R_K = h/e^2 \simeq 26$ kΩ
R_q	reduced superconducting resistance quantum, $R_q = \hbar/(2e)^2 \simeq 1.0$ kΩ
R_Q	superconducting resistance quantum, $R_Q = h/(2e)^2 \simeq 6.5$ kΩ
t	time
T	temperature/voltage transmission coefficient
t_S	sampling time
T_1	energy relaxation time
T_2	decoherence time, $T_2^{-1} = (2T_1)^{-1} + T_\phi^{-1}$
T_2^*	Ramsey fringe decoherence time
T_ϕ	dephasing time
V	voltage
v_p	phase velocity
V_0	voltage amplitude, zero point fluctuation voltage
V^+	forward propagating wave voltage
V^-	backward propagating wave voltage
x_{qp}	quasiparticle density normalized to Cooper-pair density
Y	admittance
Z	impedance
Z_0	characteristic impedance
α	qubit state variable, coherent state, attenuation constant
β	qubit state variable, propagation constant

γ	complex propagation constant, $\gamma = \alpha + j\beta$
Γ	energy transition rate/voltage reflection coefficient
Δ	superconducting gap
ϵ	dielectric constant
ϵ_r	relative dielectric constant, $\epsilon_r = \frac{\epsilon}{\epsilon_0}$
ϵ_0	dielectric constant of vacuum
η	transition efficiency
η_I	current division ratio
θ	angle
λ	wavelength
λ_0	wavelength of fundamental mode
μ	permittivity of free space
ν	frequency, used when f may be confused with second excited qubit state
ν_R	readout resonator fundamental frequency
ϕ_0	reduced flux quantum, $\phi_0 = \hbar/2e$
φ	superconducting phase
Φ_0	flux quantum, $\Phi_0 = h/2e$
χ	dispersive shift
ψ	wavefunction
ω	angular frequency, $\omega = 2\pi f$
ω_p	plasma frequency
ω_R	readout resonator fundamental angular frequency, $\omega_R = 2\pi f_R$
ω_0	fundamental mode angular frequency, $\omega_0 = 2\pi f_0$

List of Abbreviations

AWG	Arbitrary Waveform Generator
CPS	CoPlanar Stripline
CPW	CoPlanar Waveguide
CW	Continuous Wave
FWHM	Full Width at Half Maximum
GPIB	General Purpose Interface Bus, also known as IEEE-488
HEMT	High Electron Mobility Transistor
IF	Intermediate Frequency
LO	Local Oscillator
OFHC	Oxygen Free High Conductivity, a type of copper
PCB	Printed Circuit Board
PTFE	PolyTetraFluoroEthylene, commonly known by trade name Teflon® (DuPont™)
Q	Quality factor
QND	Quantum Non-Demolition
RF	Radio Frequency
SNR	Signal to Noise Ratio
SOLT	Short Open Load Through
SSB	Single SideBand, a type of modulation
STIRAP	STImulated Raman Adiabatic Passage

Acknowledgements

This thesis work has been the collaborative effort of many people, to whom I am happy to share credit with. I would first like to thank my advisor, Michel Devoret, for helping me develop as a scientist. His knowledge of the field, and physics in general, is truly remarkable. In addition, I would like to thank my other committee members, Rob Schoelkopf, Steve Girvin and Jack Harris, for taking the time to review my work and provide insightful feedback.

The fluxonium project was started by Michel Devoret, Leonid Glazman, Jens Koch and Vladimir Manucharyan. By the time I started working on the project, much of the theory was developed, and a working sample was in the fridge. I have learned much from each of the pioneering members of the fluxonium team, and am especially thankful to Vlad who took the time to immerse me into the project.

I had the privilege of working alongside Archana Kamal, who provided the theoretical backbone and assisted with many of the measurements. Ioan Pop, who has been a pleasure to work with, joined the lab during my final year and was vital in the experiments on Josephson junction array superinductances. Zlatko Minev assisted with simulations used in designing the superinductance experiments. During compilation of this manuscript, Ioan and Kurtis Geerlings have made great strides in developing fluxonium in a three-dimensional readout cavity.

I am grateful to Luigi Frunzio for introducing me to nanofabrication, and always

being willing to assist when something inevitably goes wrong. I thank Dan Prober for many interesting discussions. I have been fortunate to share my graduate experience in the lab with Flavius Schackert. I have learned much from other members of Michel and Rob's lab, and would like to acknowledge especially Markus Brink, Chad Rigetti, Hanhee Paik and Dave Schuster.

Finally, and above all, I would like to thank my family.

Chapter 1

Introduction

The main goal of this thesis work is the reduction of losses in the fluxonium qubit, a unique superconducting artificial atom. Losses in each of the elements which make up the qubit are explored, as well as methods of improvement. As this thesis is compiled, progress has continued to further refine the purity of the environment that the qubit is subject to, with significant gains in qubit lifetime.

In this chapter, we start with a brief overview of superconducting qubits, describing the basics of the various superconducting qubits that make up the field. Viewing the fluxonium in this context should exemplify its rich structure and desirability for further study. Next, the flux dependent relaxation time of five samples will be examined, gaining insights on the impurities in the system, as well as methods for removing them. Lastly, we discuss detailed characterization of Josephson junction array superinductances, a crucial component of the fluxonium circuit. Later chapters go into further details and theory behind these experiments, as well as information that should prove useful for future experiments on fluxonium or other quantum electronics.

1.1 Superconducting Qubits

A desirable qubit has a number of conflicting requirements in order to meet the DiVincenzo criteria for implementation of a quantum computer [4]; large anharmonicity, efficient reset, long coherence times, reliable control and high readout fidelity. In order to perform rapid operations, the qubit must be sufficiently anharmonic such that the spacing between energy levels is not too uniform; the frequency components of short pulses could couple unwanted transitions. Coherence times must be long enough to be able to perform a desired algorithm or implement error correction before the qubit is likely to dephase or relax. Qubits which are well isolated from the environment will be better protected from relaxation or dephasing, however the qubit must be sufficiently coupled to control and readout mechanisms to be practical. Reset may be implemented through good thermalization and methods like sideband cooling (Section 5.2).

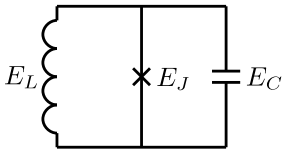

Figure 1.1: Schematic of a generic qubit, with inductive energy E_L, Josephson energy E_J and capacitive energy E_C. An external flux bias may be applied to the loop formed by the inductor and Josephson junction to tune the Josephson energy.

On the surface, all superconducting qubits are nothing more than LC oscillators which have been made non-linear through the addition of a Josephson element [5, 6] (although it may be possible to use a phase slip element to provide the non-linearity [7]). Anharmonicity is required in order to isolate two energy levels to create a "qubit", a quantum two-level system representing a quantum bit (for instance, the qubit "0" and "1" will be the ground state and first excited state of the system, respectively). Throughout this thesis the term "qubit" will be used a bit more

loosely and often replaced by "atom", as higher levels are often utilized (for example, the readout mechanism in fluxonium relies on the second excited state). The qubit itself (ignoring any auxiliary circuitry for control or readout) consists of Josephson junctions, capacitors and inductors. The schematic of a generic qubit is shown in Figure 1.1. Each of the components have an associated energy scale which describe the qubit; the Josephson energy for a junction with critical current I_c is $E_J = I_c\phi_0$, the charging energy for capacitance C is $E_C = e^2/2C$, and the inductive energy for inductance L is $E_L = \phi_0^2/L$. $\phi_0 = \hbar/2e$ is the reduced flux quantum.

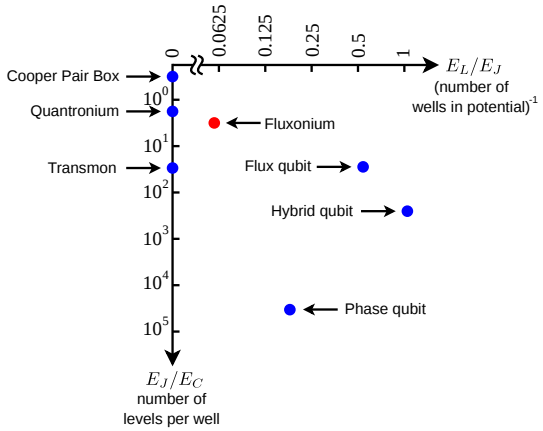

Figure 1.2: The "Mendeleev" table of superconducting qubits.

Since coherent oscillations were first observed in a Cooper pair box [8] in 1999 [9], a variety of superconducting qubits have been introduced [10, 11, 12, 13, 14, 3]. The various qubit implementations may be organized by their energy scales in a "Mendeleev" table, as shown in Figure 1.2. Superconducting qubits may be placed in two classes, "charge" qubits, which have a superconducting island that is galvanically isolated from ground with the exception of a Josephson junction that allows the tunneling of Cooper pairs, and "inductively shunted" qubits, where the island has an inductive shunt to ground. Charge qubits do not have a shunting inductance, and therefore have $E_L = 0$ and lie on the y-axis of Figure 1.2.

Like the chemical properties of elements in the periodic table, the table in Figure 1.2 exhibits trends in the qubit properties. As E_J/E_C increases or E_L/E_J decreases, qubits show more anharmonicity. In the reverse direction (decreasing E_J/E_C or increasing E_L/E_C), charge noise is reduced. And as loop inductance increases (E_L/E_J decreases), flux noise is reduced. Because of the wide parameter space available, it is important to explore the various regions. In time, there may not be one qubit architecture that wins, but several whose properties are exploited depending on the application. Fluxonium is unique amongst all other superconducting qubits utilized to date, having protection from charge noise while still displaying high anharmonicity, with an accessible multi-level structure over wide flux tunability.

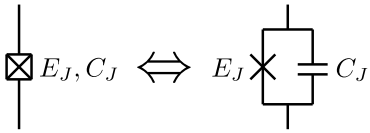

Figure 1.3: Schematic symbols for a Josephson junction. A cross with a box includes the junction capacitance, while an unboxed cross represents the Josephson element only (non-linear inductance).

To give a quick taste of the qubit varieties, and place the fluxonium qubit in the context of superconducting qubits as a whole, each qubit type will be briefly described below. More detailed information may be gained from the references therein, or from other superconducting qubit overviews: [15, 16]. In the schematics presented below (and elsewhere in this manuscript), the Josephson element is represented as a cross, while a box with a cross represents the physical implementation of a Josephson junction including the capacitance of the junction, as shown in Figure 1.3.

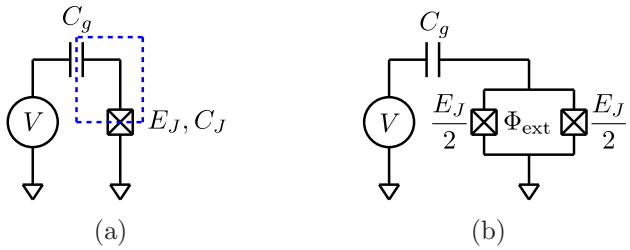

Figure 1.4: (a) Schematic of the Cooper pair box. The dashed box encloses the island. (b) Split Cooper pair box, allowing flux tunability of E_J.

1.1.1 Charge Qubits

Cooper Pair Box

The Cooper pair box is a charge qubit that consists of a Josephson junction voltage biased through a gate capacitor (see Figure 1.4) [8]. An island is formed between the gate capacitor and Josephson junction, where Cooper pairs may tunnel on and off through the Josephson junction. The Josephson junction may be replaced with a SQUID (referred to as the split Cooper pair box) to allow flux tunability of the Josephson energy $E_J = E_{J,\max}|\cos(\pi\Phi_{\text{ext}}/\Phi_0)|$, where $E_{J,\max}$ is twice the Josephson energy of the individual junctions.

The capacitance of the island $C_\Sigma = C_g + C_J$, is the sum of the gate capacitance C_g and the capacitance of the Josephson junction C_J. The electrostatic part of the Hamiltonian for the Cooper pair box is given by

$$H_{\text{el}} = 4E_C(\hat{n} - n_g)^2, \tag{1.1}$$

where $E_C = e^2/2C_\Sigma$ is the charging energy of the island (Coulomb energy to add one electron to the island), $\hat{n}$ is the integer number of excess Cooper pairs on the island, $n_g = C_gV/(2e)$ is the dimensionless gate voltage, and V is the bias voltage applied to the gate capacitor. Any offset charge on the capacitors can be lumped into V.

In addition to the electrostatic Hamiltonian, there is a term due to the Josephson element

$$H_J = -E_J \cos\hat{\phi}, \tag{1.2}$$

where $E_J = I_c\phi_0 = \Delta R_K G_t/8$ is the Josephson energy, which is proportional to the area of the tunnel junction, and $\hat{\phi}$ is the superconducting phase across the junction, which is canonically conjugate to the island charge ($[\hat{\phi}, \hat{n}] = i$). $R_K = h/e^2 \simeq 26$ kΩ is the resistance quantum, G_t is the junction tunnel conductance, and Δ is the superconducting gap (180 μeV for aluminum). The Cooper pair box is operated in the regime where $E_J < E_C$, where phase fluctuations exceed charge fluctuations, making n the better quantum number. Writing the full Hamiltonian, we have:

$$H = 4E_C(\hat{n} - n_g)^2 - E_J \cos\hat{\phi}. \tag{1.3}$$

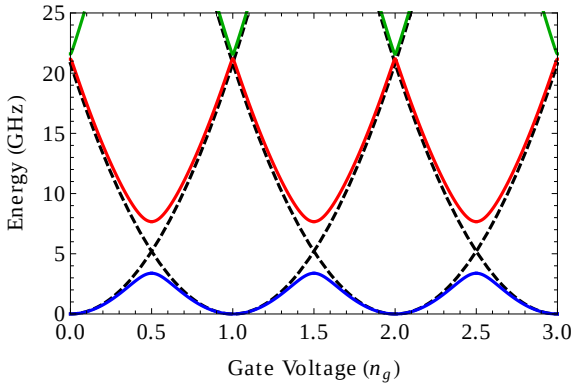

Figure 1.5: Cooper pair box levels for $E_J/E_C = 4.3$ GHz / 5.2 GHz $= 0.83$, same as the split Cooper pair box measured in reference [1] at maximum E_J. Dashed black parabolas are the electrostatic energy, while solid lines are the total energy of the box.

The electrostatic part of the Hamiltonian produces a set of parabolas in energy versus the gate voltage, shown in Figure 1.5. For half integer n_g there exists degeneracies between these parabolas, crossing at energy E_C. Adding in the Josephson

Hamiltonian the degeneracy is lifted, resulting in avoided crossings. The level splitting is $\sim E_J$ at the degeneracy.

When utilizing this circuit as a qubit, there is a distinct advantage in setting the bias voltage V such that n_g is a half integer. At this spot, known as the "sweet spot", the qubit is first-order insensitive to charge fluctuations [15], a notorious problem in charge qubits. Relaxation times as high as 0.2 ms have been achieved in a Cooper pair box in a compact resonator on sapphire [17], however coherence times continue to be plagued with charge noise. Charge noise has led to the development of the transmon, where having $E_J/E_C \gg 1$ exponentially suppresses charge dispersion [13].

The quantronium qubit is a variation on the Cooper pair box which adds circuitry for separating the control and readout ports, and is operated in the regime where $E_J \simeq E_C$ [11, 18].

Transmon

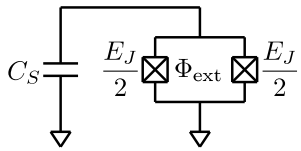

Figure 1.6: Schematic of the transmon qubit. Shunting capacitance C_S reduces the charging energy E_C of the island.

Topologically, the transmon qubit (shown schematically in Figure 1.6) is identical to the Cooper pair box. However in the transmon, the ratio of the Josephson energy E_J to the charging energy E_C is made significantly larger through the addition of a large shunting capacitance across the junction (the energy ratio is typically several tens). The increase in E_J/E_C exponentially reduces charge dispersion, and therefore sensitivity to charge noise, while anharmonicity is more weakly dependent on the

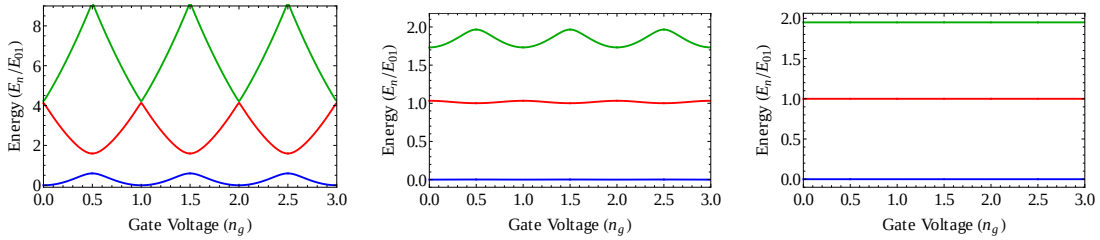

(a) $E_J/E_C = 1$ (b) $E_J/E_C = 10$ (c) $E_J/E_C = 70$

Figure 1.7: Charge dispersion versus E_J/E_C ratio. As E_J/E_C increases, the effect of offset charge on transition energy is reduced exponentially, suppressing charge noise and eliminating the need to bias at the sweet spot. Energy levels are divided by the transition energy between the ground and first excited states baised at the degeneracy point $n_g = 0.5$.

energy ratio through a power law [13, 19]. The strong effect on charge dispersion is shown in Figure 1.7, and has been experimentally demonstrated in reference [20].

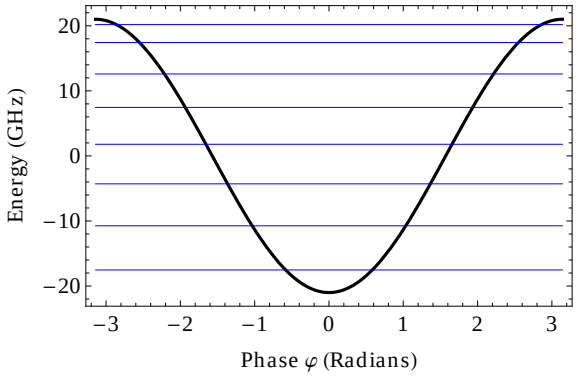

Figure 1.8: Transmon potential (black) with eigenenergies (blue lines) for E_J/E_C = 21 GHz / 0.3 GHz = 70.

For the E_J/E_C ratios in the transmon, the superconducting phase becomes the better quantum number, and the circuit may be thought of as an anharmonic oscillator where the Josephson junction acts as a nonlinear inductance producing the potential shown in Figure 1.8. As a result of the potential which widens faster than a parabola, the energy levels are spaced closer together at higher energies. At a given E_J, E_C dictates how many levels will fit in the potential. For higher E_J/E_C ratios,

more levels fit in the well (and charge dispersion is suppressed), but anharmonicity between levels is reduced.

The transmon has remained a popular qubit, and with the advent of using three-dimensional cavity resonators for readout over planar resonators to reduce substrate surfaces losses [21], coherence times have been pushed towards the 0.1 ms range [22].

1.1.2 Inductively Shunted Qubits

In inductively shunted qubits, the Hamiltonian of the Cooper pair box (Equation (1.3)) gains an added term due to the shunt inductance:

$$H = 4E_C(\hat{n} - n_g)^2 - E_J \cos\hat{\phi} + \frac{1}{2}E_L\left(\hat{\phi} + 2\pi\frac{\Phi_{\text{ext}}}{\Phi_0}\right)^2, \tag{1.4}$$

with E_L given by the shunt inductance L:

$$E_L = \frac{(\Phi_0/2\pi)^2}{L}. \tag{1.5}$$

Because of the change in circuit topology, $\hat{\phi}$ is no longer a compact variable as it is in the Cooper pair box and transmon. We may therefore redefine $\hat{\phi}$ to move the flux dependence to the Josephson term:

$$\hat{\varphi} = \hat{\phi} + 2\pi\frac{\Phi_{\text{ext}}}{\Phi_0}. \tag{1.6}$$

In addition, the offset charge n_g may be removed through a gauge transformation $\psi'(\varphi) = \mathrm{e}^{in_g\varphi}\psi(\varphi)$. Physically this has been made possible through the vanishing dc impedance provided by the shunt inductance [23]. With these changes, we may

rewrite the Hamiltonian as

$$H = 4E_C\hat{n}^2 + \frac{1}{2}E_L\hat{\varphi}^2 - E_J\cos\left(\hat{\varphi} - 2\pi\frac{\Phi_{\text{ext}}}{\Phi_0}\right). \tag{1.7}$$

The last two terms in this Hamiltonian give us an inductive potential which is parabolic with phase, due to the shunting inductance, made non-linear with corrugations due to the Josephson junction.

Flux Qubits

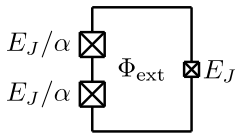

Figure 1.9: Schematic of the flux qubit, with two large junctions serving to increase the loop inductance.

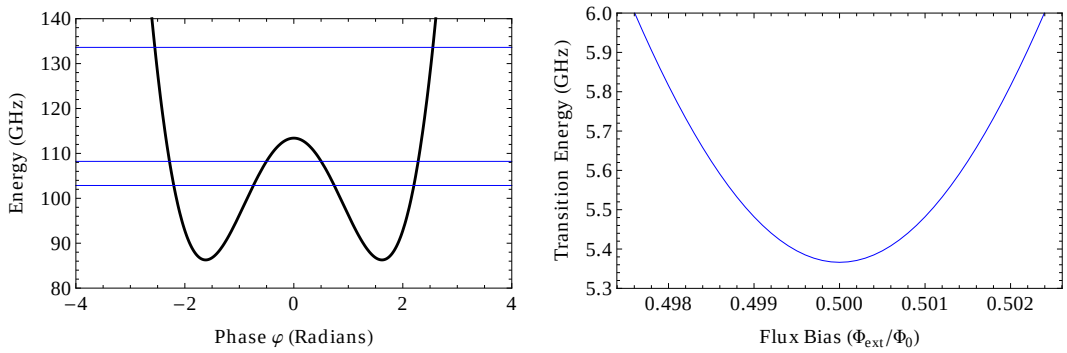

(a) (b)

Figure 1.10: (a) Flux qubit potential (black) at $\Phi_{\text{ext}} = \Phi_0/2$, with lowest three energy levels (blue). (b) Ground to first excited state transition energy versus flux bias. Qubit parameters used are $E_J/h = 113$ GHz, $E_C/h = 3.18$ GHz, $E_L/h = 70$ GHz, that of the qubit measured in [2].

The flux qubit consists of a superconducting loop interrupted by a Josephson junction. The loop often contains two [10, 24, 25] or three [2] additional junctions of

larger area which serve to increase the inductance of the loop (the ratio of the critical current between the small and large junctions is often quoted as "α"), although the loop may contain only one junction [26]. A schematic of a flux qubit is shown in Figure 1.9. The Josephson energy exceeds the inductive energy ($E_J > E_L$). When biased around $\Phi_{\text{ext}} = \Phi_0/2$ the small inductance of the loop results in a steep inductive potential with two wells due to the Josephson junction, as shown in Figure 1.10. The ground and first excited states of the qubit respectively correspond to the symmetric and antisymmetric combination of current flowing clockwise and counterclockwise in the loop. The small loop inductance, and therefore steep inductive potential, make flux qubits very sensitive to flux bias, and therefore susceptible to flux noise.

Phase Qubits

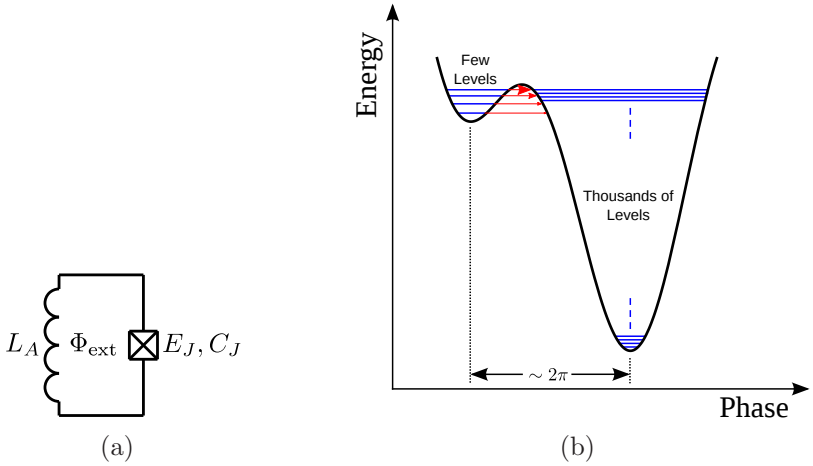

(a) (b)

Figure 1.11: (a) Schematic of the phase qubit. (b) Potential (black) and energy levels (blue). The shallow well on the left contains the qubit levels. The higher levels in the left well have greater transition rates for tunneling into the deep well on the right.

In phase qubits [27], a large Josephson junction is current biased just under the critical current to produce a shallow anharmonic well that is approximately cubic

[28]. The higher energy states in the well are exponentially more likely to tunnel out. Originally, flux qubits were read out by sending an excitation tone between the first and second excited states, and detecting if the junction switched into the voltage state after tunneling out of the second excited state [12] (if the junction switches to the voltage state, the qubit was likely in the first excited state). However, this destructive measurement scheme generated quasiparticles [29], so the design was modified by shunting the Josephson junction with an inductor, and applying an external flux bias to produce a shallow well with a few levels, and a larger well that the qubit may tunnel into, as illustrated in Figure 1.11. The qubit state is read out by monitoring changes in flux with a SQUID to indicate whether a tunneling event occurred. Tunneling is initiated by either sending an excitation tone between the first excited state and a higher level with a faster tunneling rate [30], or by pulsing the flux bias to temporarily reduce the barrier height and increase the tunneling rate of the first excited state [31]. However, the readout still has the disadvantage that it is strictly non-QND.

Hybrid Qubits

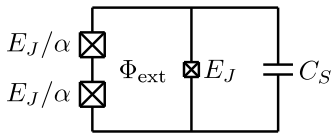

Figure 1.12: Schematic of the hybrid qubit.

Also known as a low-Z flux qubit, hybrid qubits are flux qubits in the regime $E_J < E_L$, resulting in a potential with a single well [3]. Additionally, by shunting the small junction with a large capacitance, both charge and flux noise are considerably suppressed [32]. Transition energy dependence on flux is much weaker than in tradi-

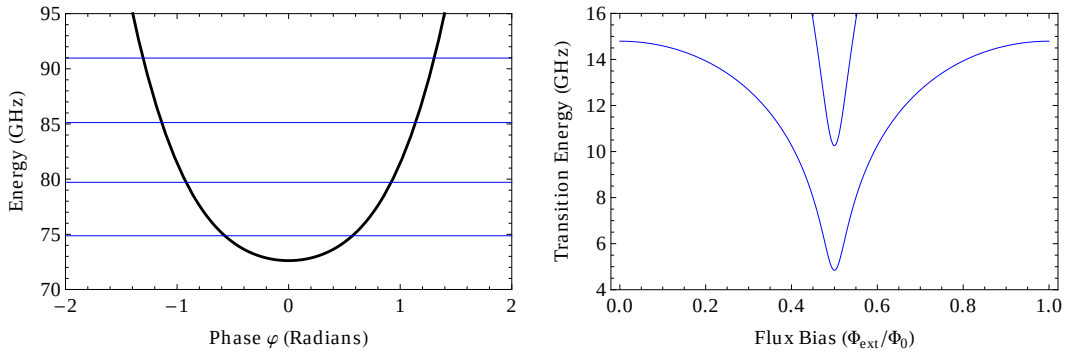

(a) (b)

Figure 1.13: (a) Hybrid qubit potential (black) at $\Phi_{\text{ext}} = \Phi_0/2$, with lowest four energy levels (blue). (b) Single photon transition energies from the ground state versus flux bias. Qubit parameters used are $E_J/h = 73$ GHz, $E_C/h = 0.18$ GHz, $E_L/h = 84$ GHz, that of the qubit measured in reference [3].

tional flux qubits, with flux sensitivities comparable to the phase qubit. The hybrid qubit is shown schematically in Figure 1.12, and a representative potential is shown in Figure 1.13. When biased near $\Phi_{\text{ext}} = \Phi_0/2$, the hybrid qubit exhibits an anharmonicity opposite that of the transmon qubit, such that higher transitions become further separated. As the qubit is biased away from $\Phi_{\text{ext}} = \Phi_0/2$ the anharmonicity reverses, as illustrated in Figure 1.14.

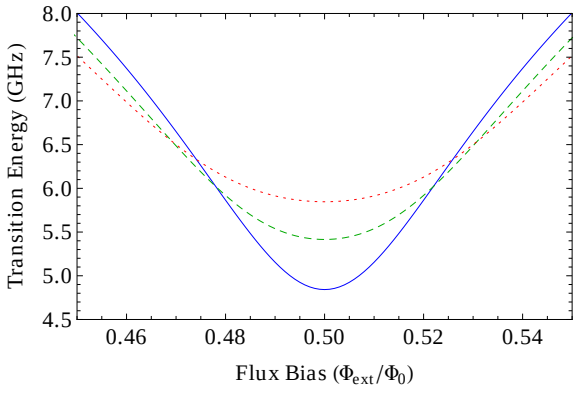

Figure 1.14: The qubit anharmonicity near $\Phi_{\text{ext}} = \Phi_0/2$ is inverted. g–e (solid blue), e–f (dashed green), f–h (dotted red).

Fluxonium

Fluxonium is unique amongst all superconducting qubits demonstrated to date. The Cooper pair box and quantronium have fallen out of favor as viable superconducting qubits for quantum computation due to their inherent sensitivity to charge noise. Transmon and hybrid qubits are both weakly anharmonic oscillators. Flux and phase qubits are extremely sensitive to flux noise, and usually limited to operating in the ground and first excited states. By contrast, fluxonium is highly anharmonic with multiple accessable levels, and can be read out and manipulated over its entire flux tunable range, with the g–f transition spanning over 5 octaves while the g–f remains fixed well within one octave. Fluxonium a true multi-level artificial atom with a spectrum unlike any other superconducting qubit. These properties make fluxonium an attractive qubit for further study.

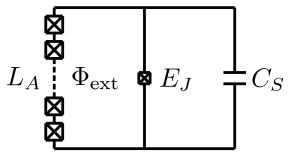

Figure 1.15: Schematic of the fluxonium qubit. An array of large junctions forms the shunt inductance, L_A. Note that C_S is not a capacitance deliberately added to shunt the small junction, rather it is the stray capacitance from connecting wires and coupling to the readout resonator. This added capacitance is shown here because it is comparable to the capacitance of the small junction, and is a significant portion of the total shunt capacitance C_Σ.

In the fluxonium qubit, shown in Figure 1.15, a small Josephson junction is shunted by a large inductance. The large inductance L_A is formed by an array of larger area Josephson junctions, and has a microwave impedance exceeding the resistance quantum $R_Q = h/(2e)^2 \simeq 6.5$ kΩ in the frequency range of interest. Such an inductance, whose impedance exceeds the resistance quantum at microwave frequencies below its self-resonant frequency, is termed a "superinductance". Such an

inductance is not realizable using conventional inductors due to the inherent stray capacitance between windings (or equivalently, due to the small value of the fine structure constant). We discuss superinductance and its implementation below in Section 1.4.

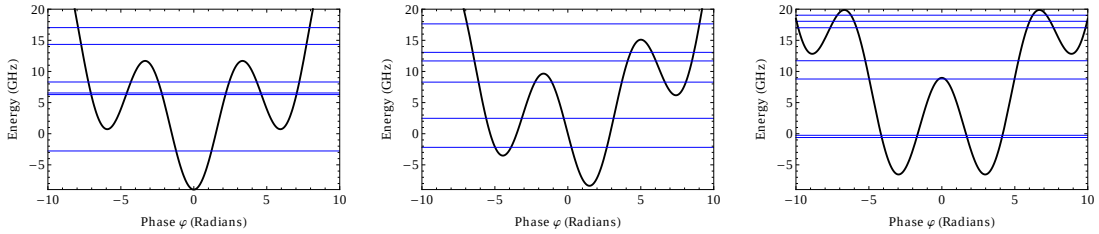

(a) $\Phi_{\text{ext}} = 0$ (b) $\Phi_{\text{ext}} = \Phi_0/4$ (c) $\Phi_{\text{ext}} = \Phi_0/2$

Figure 1.16: Fluxonium potential (black) and energy levels (blue) for $E_J/h = 8.97$ GHz, $E_C/h = 2.47$ GHz, $E_L/h = 0.520$ GHz.

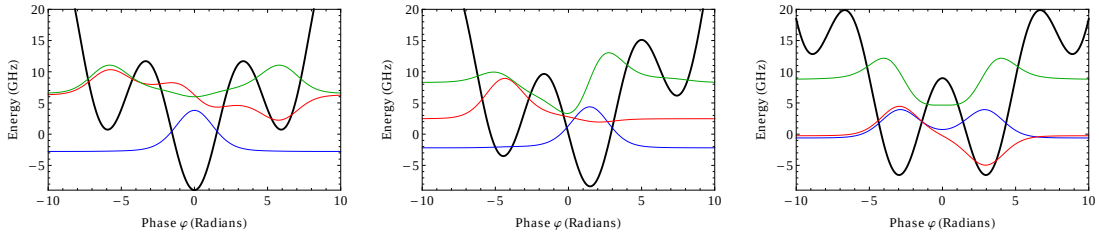

(a) $\Phi_{\text{ext}} = 0$ (b) $\Phi_{\text{ext}} = \Phi_0/4$ (c) $\Phi_{\text{ext}} = \Phi_0/2$

Figure 1.17: Fluxonium potential (black) and wavefunctions for the states g (blue), e (red) and f (green). Qubit energies are $E_J/h = 8.97$ GHz, $E_C/h = 2.47$ GHz, $E_L/h = 0.520$ GHz.

Fluxonium exists in the energy regime where $E_J > E_C > E_L$. The large inductance results in a shallow inductive potential with corrugations from the small junction, as shown in Figure 1.16. The wavefunctions for the lowest three energy levels are shown in Figure 1.18. Biased near $\Phi_{\text{ext}} = 0$, the g, e and f states form a V system, while a Λ system is formed near $\Phi_{\text{ext}} = \Phi_0/2$. For intermediate flux bias, the g and e are fluxon modes localized in two different wells, as seen in Figure 1.17(b).

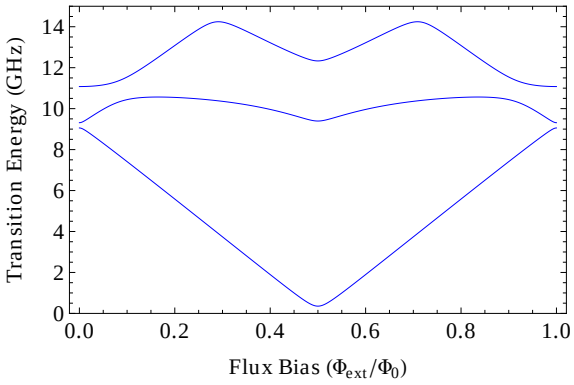

Figure 1.18: Single photon transition energy spectrum of fluxonium from the ground state for $E_J/h = 8.97$ GHz, $E_C/h = 2.47$ GHz, $E_L/h = 0.520$ GHz.

As flux is swept, the g–e transition varies linearly with a slope proportional to $1/L_A$, as seen in Figure 1.18. The f state remains relatively stable with flux bias, as it is more of a plasmon mode, which is an excitation between the shunt inductance and capacitance. At $\Phi_{\text{ext}} = \Phi_0/2$ the potential resembles that of the flux qubit, where the g and e states become the symmetric and antisymmetric superpositions of the degenerate fluxon modes.

The stability of the g–f transition is exploited for reading out the qubit state. By placing the readout resonator frequency near the g–f transition frequency, the state of the qubit may be observed over the entire flux tunable range in a dispersive measurement, even when the g–e transition is hundreds of megahertz (see Section 2.2). This unique property also allows protection from the Purcell effect by tuning the g–e transition far from the readout frequency.

1.2 Fluxonium Samples

[1]This is the total coupling capacitance

Property	Sample 1	Sample 2	Sample 3	Sample 4	Sample 5
Substrate	300 μm Si	500 μm Si	500 μm Si	500 μm Si	250 μm Si
Silver Backing	No	No	No	No	1.2 μm thick
E_J/h	8.97 GHz	10.2 GHz	12.0 GHz	9.11 GHz	4.68 GHz
E_C/h	2.47 GHz	2.46 GHz	2.57 GHz	2.59 GHz	3.11 GHz
E_L/h	0.520 GHz	0.545 GHz	0.892 GHz	1.04 GHz	0.567 GHz
Array Inductance, L_A	314 nH	300 nH	183 nH	157 nH	289 nH
Readout Frequency, f_R	8.175 GHz	8.093 GHz	8.131 GHz	8.114 GHz	7.589 GHz
Readout Loaded Q	410	550	2200	400	390
Readout Line Impedance	78 Ω	110 Ω	110 Ω	110 Ω	100 Ω
Qubit–Readout Coupling	Capacitive	Capacitive	Capacitive	Capacitive	Inductive
Coupling Strength, g/h	0.18 GHz	0.21 GHz	0.22 GHz	0.17 GHz	0.045 GHz
Coupling Capacitance[1]	0.8 fF	0.6 fF	0.6 fF	0.3 fF	—
Coupling Inductance	—	—	—	—	6.5 μH

Table 1.1: Device parameters for fluxonium samples

Five different fluxonium samples were measured in the course of this thesis work. A summary of parameters for the samples is presented in Table 1.1. Sample 1 is the original fluxonium device studied in references [14, 23, 33, 34]. Samples 2 and 3 were fabricated two years after the original sample in order to test the reproducibility of the original device. These samples were fabricated to be nominally identical to the original, with the exception that a 500 μm silicon substrate was used due to the unavailability of 300 μm substrates. Sample 2 was very similar to the original, and sample 3 had reduced oxidation which made it useful as a control experiment for phase-slip dephasing in reference [33].

When the relaxation times of the first three samples indicated limiting due to capacitive losses, all with similar capacitor quality factors, sample 4 was fabricated with the qubit to readout resonator interdigitated finger coupling capacitors replaced with capacitor pads with a wider separation. This change in geometry reduced the surface participation of the substrate with the electric field in the coupling capacitors. Sample 4 showed a significant improvement in the capacitor quality factor, however the relaxation times were still limited by capacitive loss. Samples 2–4 were fabricated

on the same silicon wafer from cleaved chips after e-beam resist was spun. Samples 2 and 3 were fabricated within two weeks of one another, while sample 4 was fabricated 8 months later.

Rather than capacitively coupling the qubit to the readout resonator, sample 5 utilized inductive coupling through a large Josephson junction (acting as a linear inductance), eliminating coupling capacitors altogether. This sample was fabricated on a double polished silicon wafer with 1.2 μm of silver evaporated on the back to facilitate thermalization of the device. Details on device fabrication are in Appendix B.

1.3 Losses in Fluxonium

The energy relaxation time, T_1, is an important quantity, as it limits the coherence time, T_2, of a qubit ($T_2^{-1} = [2T_1]^{-1} + T_\phi^{-1}$, where T_ϕ is the pure dephasing time). Since the ultimate goal is to produce a usable quantum computer, the energy relaxation time must be long enough that it does not limit T_2 to a point where using the qubit in a computer is impractical. Successful implementation of a quantum computer requires the ability to perform a large number of gates, with an error per gate probability on the order of 10^{-4} needed for quantum error correction [35]. In order to minimize the error per gate, qubit operations must be fast with respect to T_2. The anharmonicity of a qubit sets a limit on how fast an operation can be, as the large spectral content of fast pulses will result in coupling to states out of the computational space. But once fast operations on a particular qubit have been optimized, the only way to improve the error per gate probability is to improve T_2. The error per gate has not yet been studied in fluxonium, however it is likely to be a couple orders of magnitude away from the threshold required for quantum error correction (transmons with comparable T_2 have error per gate probabilities on the

order of 10^{-2} [36, 37]).

The energy relaxation time in a given qubit may be limited by a number of factors; inductive losses, quasiparticles in the small junction, capacitive losses, the Purcell effect, etc. The rate of each of these loss mechanisms sum together to give the total energy relaxation rate, setting the T_1 time:

$$T_1 = \frac{1}{\Gamma^{\text{ind}}_{e\to g} + \Gamma^{\text{qp}}_{e\to g} + \Gamma^{\text{cap}}_{e\to g} + \Gamma^{\text{Purcell}}_{e\to g} + \ldots}. \tag{1.8}$$

When a T_1 time is measured, the most that can be said about any particular loss mechanism is that it is no worse than some particular value. Since the contributions from other loss mechanisms are unknown, only a bound can be placed on each loss mechanism. In quantifying losses in the inductance and capacitance, a quality factor, or Q, may be used. The quality factor for an inductor is the ratio of the reactance to the resistance of the inductor, while the quality factor for a capacitor is given by the ratio of the susceptance to the conductance of the capacitor. The higher the quality factor, the lower the losses. Measuring T_1 places a lower bound on quality factors. In the case of quasiparticle loss, the quasiparticle density to Cooper pair density ratio is the key parameter, and measured T_1 times place upper bounds on the number of quasiparticles. Relaxation due to the Purcell effect may be calculated from circuit parameters, and is only significant when the qubit is tuned near the readout resonator.

While measuring a single T_1 time does little to explain what the dominant losses are, each loss mechanism has a different flux dependent coupling to the qubit, due to the noise spectral density and matrix elements pertaining to the loss mechanism. Therefore, by measuring the T_1 time versus flux bias, the trend in T_1 can reveal the dominant loss mechanisms. The theoretical expressions for losses are detailed

in Section 2.3, but in this section it is sufficient to understand that each loss has a different flux dependence.

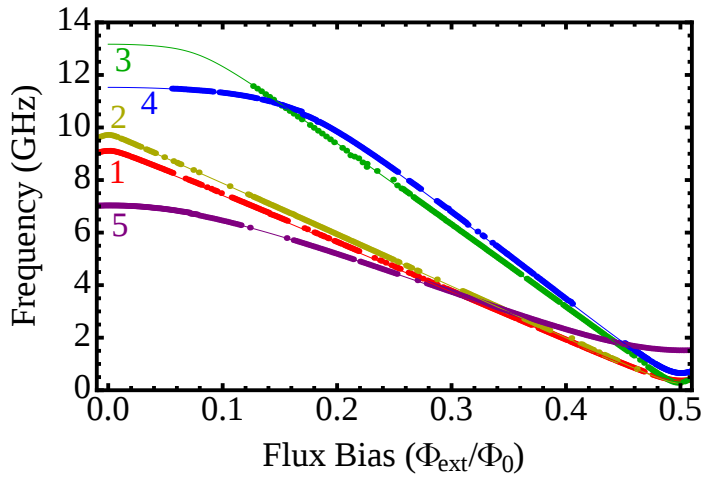

Figure 1.19: Flux dependence on the g–e transition for the fluxonium samples. Points are spectroscopic data, and solid lines are theory fits (free parameters are E_L, E_J and E_C).

Energy relaxation data versus flux bias for the five fluxonium samples was obtained through an automated process. First, a flux bias is set. A spectroscopy measurement is performed to locate the g–e transition frequency. A relaxation measurement is then performed, sending a saturation tone at the located transition frequency. The flux bias is stepped to the next value, and the process continues. Using a saturation pulse simplifies the procedure, as tuning up a π-pulse in an automated fashion in fluxonium is complicated by the range of probe tone coupling strengths to the qubit and readout contrasts versus flux bias. Spectroscopy of the g–e transition versus flux bias acquired in this method is shown in Figure 1.19. Each point on the plot represents a data point where the energy relaxation time, T_1, was measured as well. Data points where exponential fits to the relaxation data had large uncertainties in the fit have been discarded (generally where the uncertainty in T_1 exceeds the magnitude). Discarded points generally occur when the automation incorrectly

determines the g–e frequency at locations with small dispersive shifts in the readout.

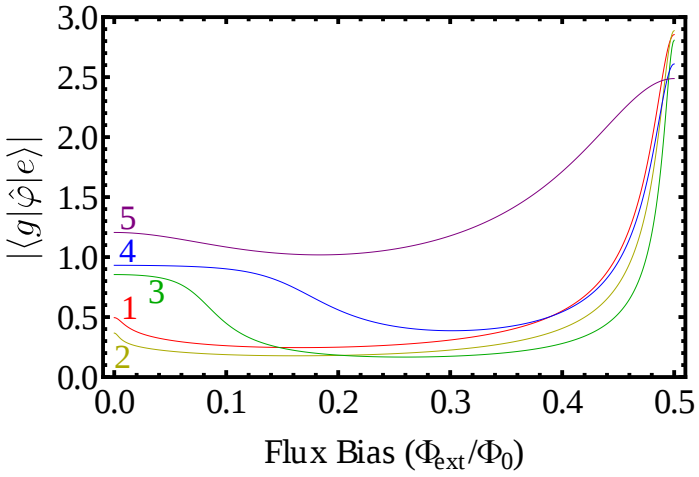

Figure 1.20: Phase matrix element between g and e for the fluxonium samples.

From the qubit parameters (E_L, E_J and E_C) extracted from spectroscopy, the g–e phase matrix elements of the five samples versus flux bias are shown in Figure 1.20. The phase matrix element describes how strongly the qubit interacts with the environment and sources of relaxation, as given in Equation (2.68) (with the exception of quasiparticle loss, which depends on $\langle \sin \frac{\hat{\varphi}}{2} \rangle$). By choosing qubit parameters that minimize the matrix elements, coupling to loss is reduced, however coupling to the readout resonator is also reduced as described by Equation (2.30) and Equation (2.17) (capacitive coupling) and Equation (2.33) (inductive coupling). Therefore, parameters must be carefully chosen such that the qubit may be reliably read out, but does not couple too strongly to losses.

The first three fluxonium samples (samples 1–3) were nominally identical samples, with slightly different qubit parameters mainly due to changes in oxidation during fabrication. Geometrically the samples were identical, with the exception of a thinner silicon substrate in sample 1. The relaxation times versus flux bias acquired for the three samples, shown in Figure 1.21, closely follows the trend predicted for relaxation

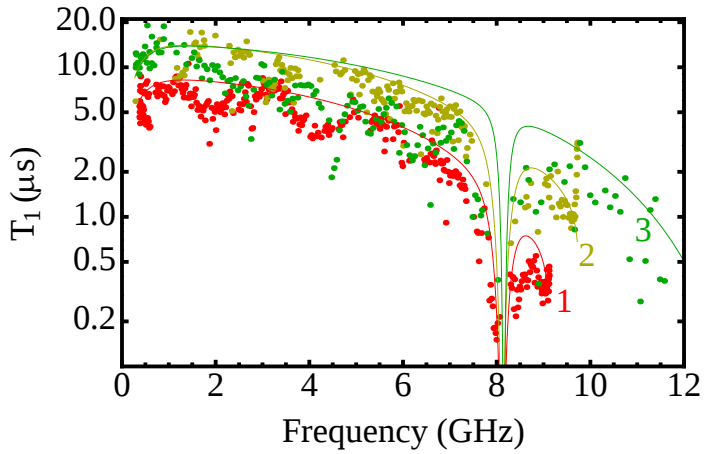

Figure 1.21: Relaxation time, T_1, of samples 1–3 versus g–e transition frequency. Points represent data, and solid lines are theory for capacitive loss, set to the 90$^{\text{th}}$ percentile (10% of points lie above the solid line). The dip near 8.1 GHz is due to Purcell loss through the readout resonator, which has been included in the theory curves. From the 90$^{\text{th}}$ percentile, $Q_{\text{cap}} > 5600$ for sample 1 (red), $Q_{\text{cap}} > 5700$ for sample 2 (yellow) and $Q_{\text{cap}} > 6000$ for sample 3 (green).

dominated by capacitive loss. Scatter in the T_1 times comes from time dependent fluctuations of roughly a factor of two (further explained in Subsection 1.3.1), as well as coupling to two-level systems at particular flux biases [38, 39]. As a conservative lower bound on the capacitive quality factor, the 90$^{\text{th}}$ percentile Q is found for each sample. For every T_1 time measured in a sample, the capacitive Q is calculated which represents the quality factor that would be required if capacitive loss were solely responsible for relaxation of the qubit. The 90$^{\text{th}}$ percentile Q is the quality factor such that 10% of the quality factors extracted were greater.

The 90$^{\text{th}}$ percentile capacitive quality factors for the three samples were comparable, ranging from 5600 to 6000. The surface of substrates have often been suspected of being lossy from a distribution of two-level systems, as evidenced by planar microwave resonator losses [40, 41, 42, 43]. With this in mind, it appeared that the finger capacitors used to couple the qubit to the readout resonator may be the dominant source of capacitive loss. This suspicion was tested by replacing the finger

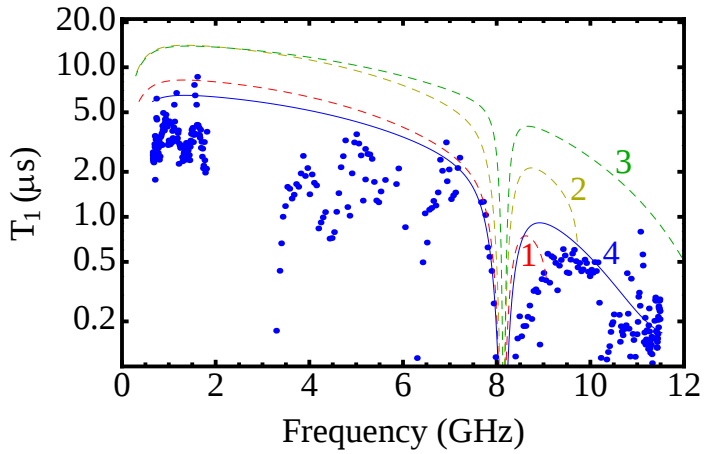

Figure 1.22: Relaxation time, T_1, of sample 4 versus g–e transition frequency. Points represent data, and solid line is theory for capacitive loss, set to the 90$^{\text{th}}$ percentile (10% of points lie above the solid line), where $Q_{\text{cap}} > 12000$. Dashed lines are the 90$^{\text{th}}$ percentile capacitive loss for samples 1–3, from Figure 1.21.

capacitors with wider gap capacitors in sample 4. The finger coupling capacitors in samples 1–3 have a 720 nm gap, shown in Figure 4.1(a), which was increased to 4 μm in sample 4, shown in Figure 4.1(b). With this change in design, the electric field in the capacitors penetrates deeper into the substrate, reducing the surface participation ratio in the capacitance.

The T_1 data for sample 4 is shown in Figure 1.22. While the T_1 times do not show a noticeable improvement, the parameters of sample 4 resulted in larger matrix elements than the previous samples (see Figure 1.20). Additionally, several two-level systems coupled to the qubit, resulting in several localized drops in T_1. But given this sample's enhanced coupling to losses, with the change in capacitor layout the 90$^{\text{th}}$ percentile Q improved by a factor of two.

This result supports the theory that substrate surfaces are lossy, and their participation in storing energy should be minimized. However, the improvement by enlarging the capacitor gap was only a step towards improving capacitive loss. Rather than increasing the gap between capacitor fingers even further, it was decided to eliminate

coupling capacitors and couple the qubit and readout resonator inductively through a shared Josephson junction. From the work of reference [17], it has been shown that the barrier in $Al/AlO_x/Al$ junctions can have loss tangents below 4×10^{-8} ($Q > 25 \times 10^6$).

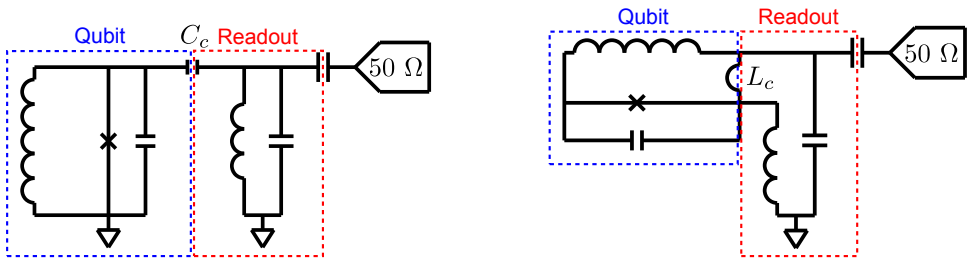

Figure 1.23: Schematic representations of (a) capacitive coupling between the qubit and readout resonator, and (b) inductive coupling.

In capacitive coupling, the qubit shunts the readout resonator via a coupling capacitor C_c, as shown in Figure 1.23(a). The qubit presents a state dependent load to the resonator. As a result, the resonant frequency shifts with qubit state, and the state of the qubit may be inferred through the phase of microwaves reflected off the readout resonator. Further details on qubit to readout resonator coupling are explained in Chapter 2. In inductive coupling, shown in Figure 1.23(b), a small inductance L_c is shared between the qubit loop and resonator. When the readout resonator is excited, a fraction of the current will divert through the small junction of the qubit. The state dependent impedance of the qubit results in shifts in the resonant frequency of the readout.

In sample 5, a large Josephson junction was used to implement the shared inductance. To ensure the coupling junction acts as a linear inductance, the junction was fabricated to be as large in area as possible using the Dolan bridge technique [44] while still producing all of the other junctions in the qubit in a single double-angle

evaporation step. By switching to a bridge-free technique [45, 46] in later samples, the coupling junctions can be made much larger in area to ensure they remain linear even when the readout is strongly driven. Several large junctions may be placed in series to increase the inductance.

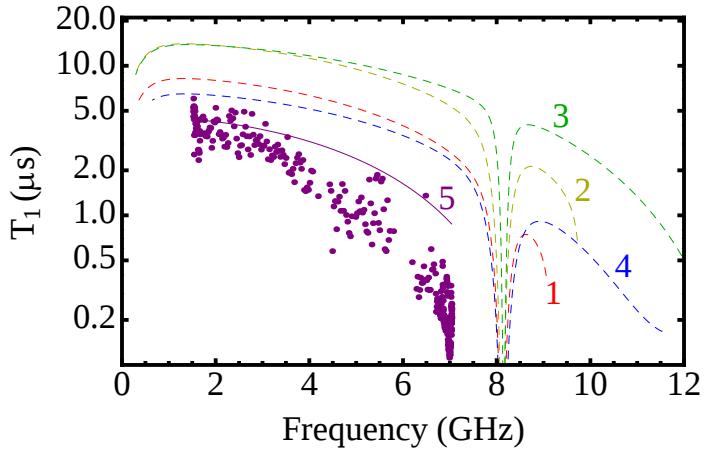

Figure 1.24: Relaxation time, T_1, of sample 5 versus g–e transition frequency. Points represent data, and solid line is theory for capacitive loss, set to the 90$^{\text{th}}$ percentile (10% of points lie above the solid line), where $Q_{\text{cap}} > 32000$. Dashed lines are the 90$^{\text{th}}$ percentile capacitive loss for samples 1–4, from Figure 1.21 and Figure 1.22.

The result of switching to inductive coupling in sample 5 was further improvement in the 90$^{\text{th}}$ percentile capacitive quality factor. However, as seen in Figure 1.22, capacitive loss alone no longer explains the trend in T_1. The deviation between the 90$^{\text{th}}$ percentile loss curve and data at higher frequencies indicates some other loss mechanism is playing a singificant role. This deviation is most closely resolved by including the effect of a population of quasiparticles, shown in Figure 1.25, with a quasiparticle density to Cooper pair density ratio of $x_{\text{qp}} < 2.6 \times 10^{-5}$ (90$^{\text{th}}$ percentile bound). Quasiparticles in thermal equilibrium are exponentially suppressed at low temperatures; at 50 mK, the equilibrium quasiparticle density is $x_{\text{qp}}^{\text{eq}} = 3 \times 10^{-19}$ The presence of non-equilibrium quasiparticles indicates the need for further filtering and shielding in the measurement setup, as the quasiparticles are likely produced from

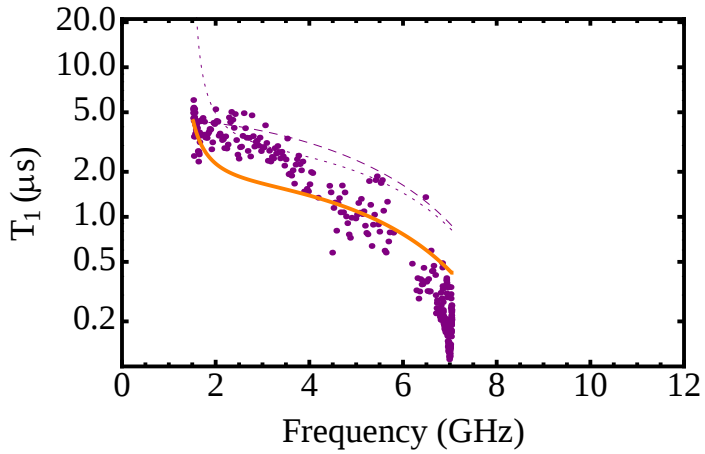

Figure 1.25: Relaxation time, T_1, of sample 5 versus g–e transition frequency. Points represent data, dashed line is theory for capacitive loss at the 90$^{\text{th}}$ percentile, and dotted line is theory for quasiparticle loss at the 90$^{\text{th}}$ percentile, where $Q_{\text{cap}} > 32000$ and $x_{\text{qp}} < 2.6 \times 10^{-5}$. The thick orange solid line is the combined capacitive and quasiparticle loss. The fact that roughly half of the T_1 points lie above the total loss curve indicate the bounds on capacitive and quasiparticle loss are very conservative.

infrared radiation leaking in.

At this stage, we see that the current limitations on the relaxation time are capacitive loss and the presence non-equilibrium quasiparticles. Inductive loss has not appeared to be a problem, so separate tests on the superinductance were performed to characterize it. These tests are detailed in the next section. Capacitive loss may be further improved by switching to a sapphire substrate. Measurement on transmons with a planar readout resonator on sapphire found to be limited by an intrinsic Q of 70,000 [47]. Further improvement may be gained by switching to a three-dimensional readout cavity architecture. Quasiparticle loss may be alleviated with the addition of Eccosorb® or copper powder filtering (see Section 4.6), and ensuring sample boxes are light-tight, and additionally shielding the area surrounding the sample box with absorptive materials like Eccosorb®, or Stycast® 2850 mixed with lampblack. Indeed, such changes have been implemented in the course of writing this manuscript through continued work by the lab, which at the present date have found evidence

that T_1 times may exceed those in other superconducting qubit implementations [48].

1.3.1 Fluctuations

In each of the samples measured, energy relaxation times were found to fluctuate by roughly a factor of two over repeated measurements. These fluctuations are observed to evolve over the course of several minutes, sometimes telegraphic in nature, and other times displaying slower drifts. Correlations are frequently observed with T_2 Ramsey and echo experiments, as exhibited in Figures 1.26–1.32. In these measurements, relaxation, Ramsey and echo experiments were performed simultaneously by interlacing pulse sequences for the three experiments.

The data show fluctuations in all five samples. Aside from what is presented here, no further studies were performed to determine the exact nature of these fluctuations. Lightly tapping the cryostat (helium was transferred during some of these measurements) or bringing small permanent magnets nearby did not have a noticeable effect. Similar fluctuations have been observed in transmon qubits when limited by dielectric loss [49], including transmons using a three-dimensional cavity readout [50]. However, some transmons with three-dimensional cavity readouts are much more stable (see supplemental material of reference [21]).

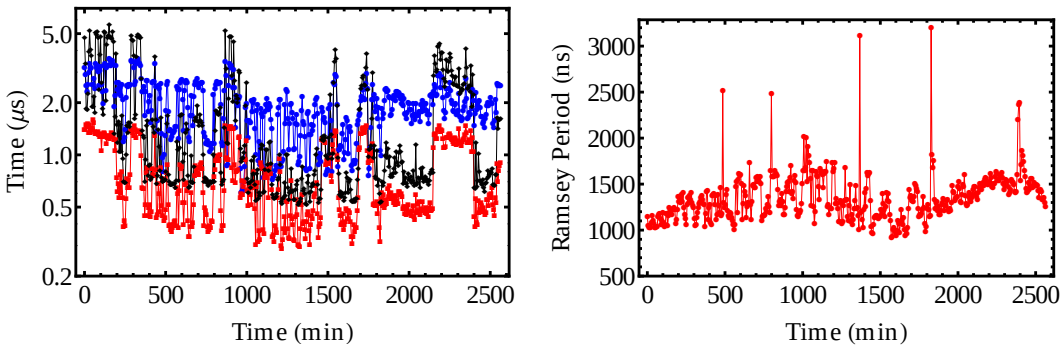

(a) (b)

Figure 1.26: (a) Fluctuations in T_1 (blue), T_2 Ramsey (red) and T_2 echo (black) of sample 1 flux biased at $\Phi_{ext}/\Phi_0 = 0.216$. (b) Period of the Ramsey fringes during the same time interval.

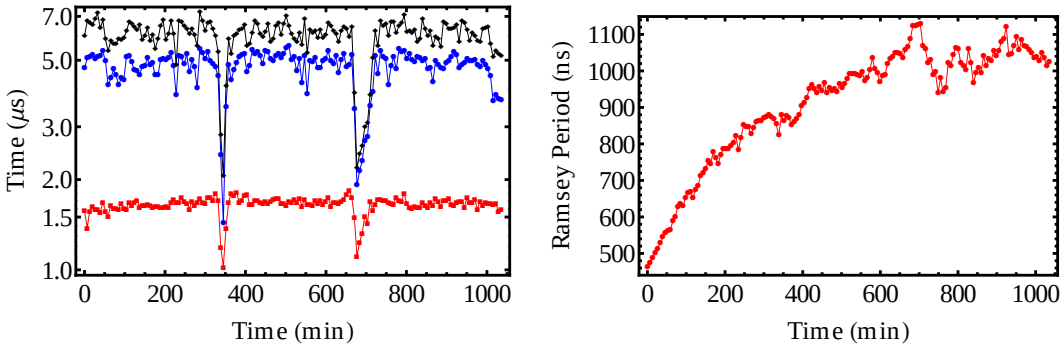

(a) (b)

Figure 1.27: a) Fluctuations in T_1 (blue), T_2 Ramsey (red) and T_2 echo (black) of sample 2 flux biased at $\Phi_{ext}/\Phi_0 = 0.146$. (b) Period of the Ramsey fringes during the same time interval.

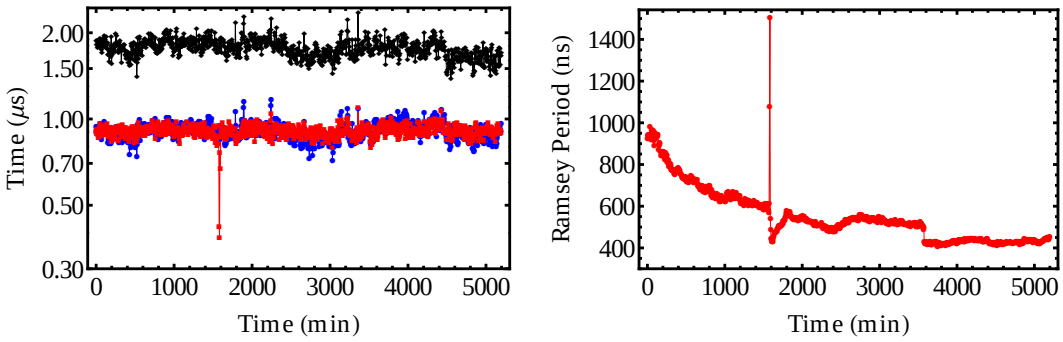

(a) (b)

Figure 1.28: (a) Fluctuations in T_1 (blue), T_2 Ramsey (red) and T_2 echo (black) of sample 2 flux biased at $\Phi_{\text{ext}}/\Phi_0 = 0.019$. (b) Period of the Ramsey fringes during the same time interval.

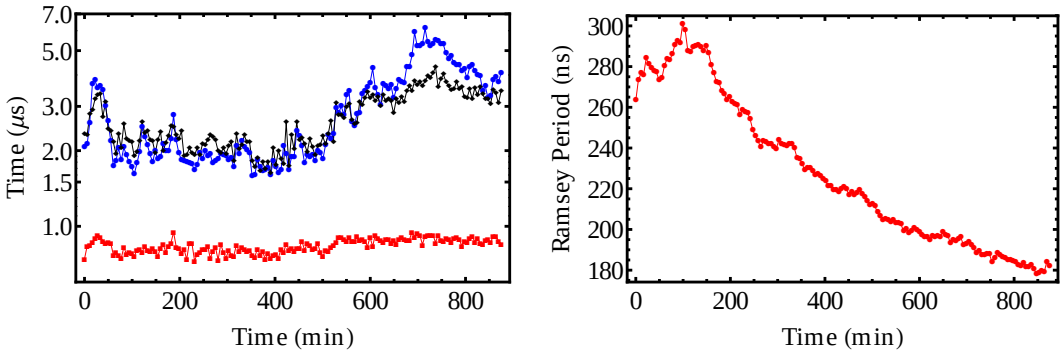

(a) (b)

Figure 1.29: (a) Fluctuations in T_1 (blue), T_2 Ramsey (red) and T_2 echo (black) of sample 3 flux biased at $\Phi_{\text{ext}}/\Phi_0 = 0.396$. (b) Period of the Ramsey fringes during the same time interval.

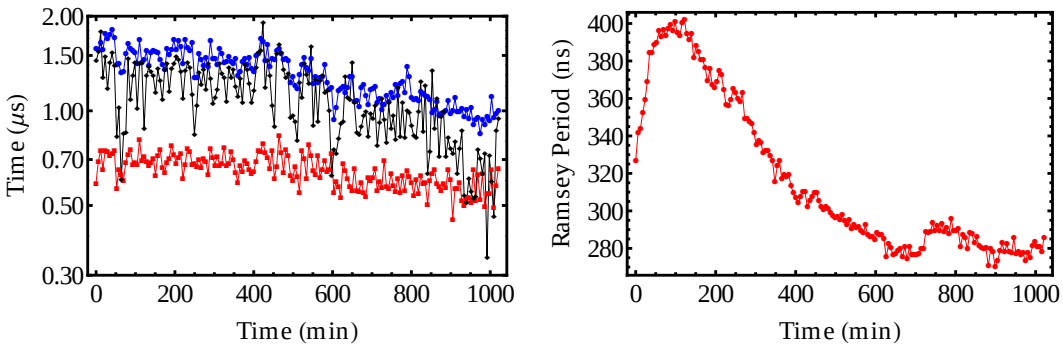

(a) (b)

Figure 1.30: (a) Fluctuations in T_1 (blue), T_2 Ramsey (red) and T_2 echo (black) of sample 3 flux biased at $\Phi_{\text{ext}}/\Phi_0 = 0.281$. (b) Period of the Ramsey fringes during the same time interval.

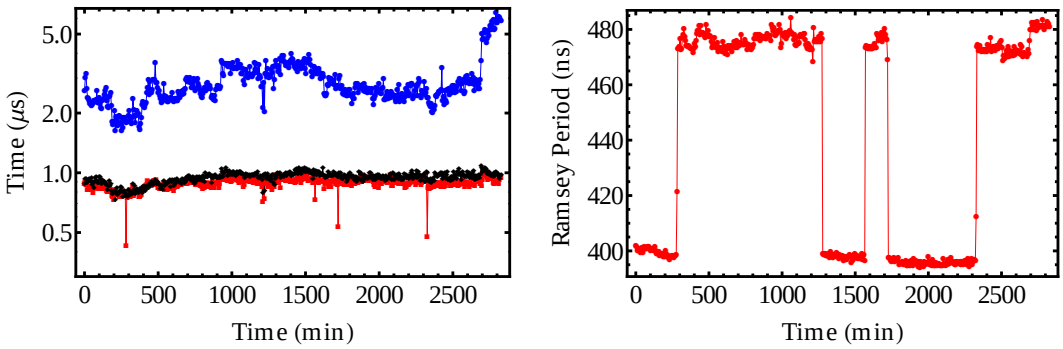

(a) (b)

Figure 1.31: (a) Fluctuations in T_1 (blue), T_2 Ramsey (red) and T_2 echo (black) of sample 4 flux biased at $\Phi_{\text{ext}}/\Phi_0 = 0.4999$. (b) Period of the Ramsey fringes during the same time interval.

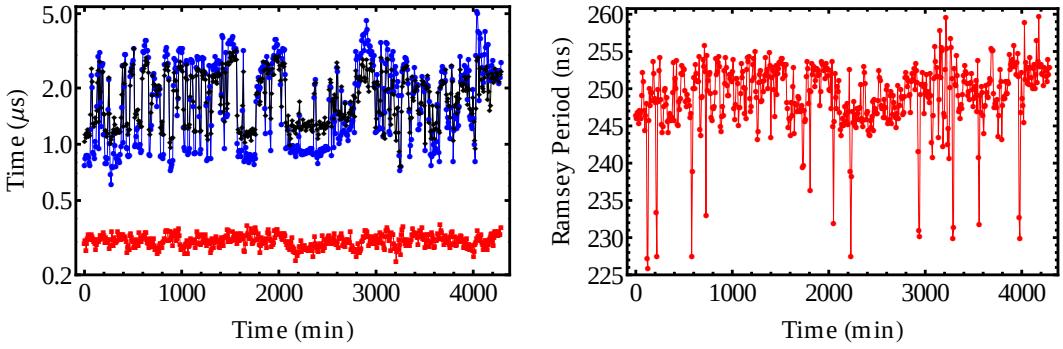

(a) (b)

Figure 1.32: (a) Fluctuations in T_1 (blue), T_2 Ramsey (red) and T_2 echo (black) of sample 5 flux biased at $\Phi_{\text{ext}}/\Phi_0 = 0.4997$. (b) Period of the Ramsey fringes during the same time interval.

1.4 Testing the Superinductance

Up to now, we have seen the effect of lossy capacitors and quasiparticles in the small qubit junction limit the relaxation time of the fluxonium qubit. As discussed at the end of Section 1.3, we know how to resolve these problems. However, we have not observed losses due to the shunt inductance. Therefore, it was decided to perform separate tests on the Josephson junction arrays to verify their performance, and look for possible weaknesses.

The Josephson junction array in the fluxonium forms a "superinductance", which is an inductance whose impedance exceeds the resistance quantum $h/(2e)^2 \simeq 6.5\ \mathrm{k}\Omega$ at microwave frequencies well below its self-resonant frequency. Due to the parasitic capacitance of wire-wound inductors, it is not possible to create a superinductance relying on magnetic inductance, as the parasitic capacitance inevitably limits the self-resonant frequency of the device [34]. Instead, the kinetic inductance of superconducting nanowires [51, 7] or Josephson junction arrays [52] may be utilized. Arrays of Josephson junctions have been used previously to test the existence of Bloch oscillations [53, 54, 55], for parametric amplifiers [56], and to test the Aharonov-Casher effect [57].

In implementing a superinductance for fluxonium, there are three requirements which must be met. First, the superinductance must be low loss. High impedance environments which are dissipative have been implemented [53, 58, 59], but such implementations would destroy quantum coherence in a qubit. Large arrays of Josephson junctions do show the appearance of a superconducting to insulating transition with decreasing Josephson energy [60, 61, 62]. Previous measurements of resonators with inductance dominated by Josephson junction arrays have had quality factors in the thousands [56, 63], while we require quality factors in at least the hundreds

of thousands to maintain similar relaxation times. Second, we require self-resonant frequencies to be above 10 GHz, so the device acts as an inductor at operational frequencies of the qubit. Third, we require low phase slip rates. Phase slips result in decoherence of the fluxonium qubit, with T_2 inversely proportional to the phase slip rate. This effect is described in Section 2.4. The following sections discuss the results of testing these three requirements.

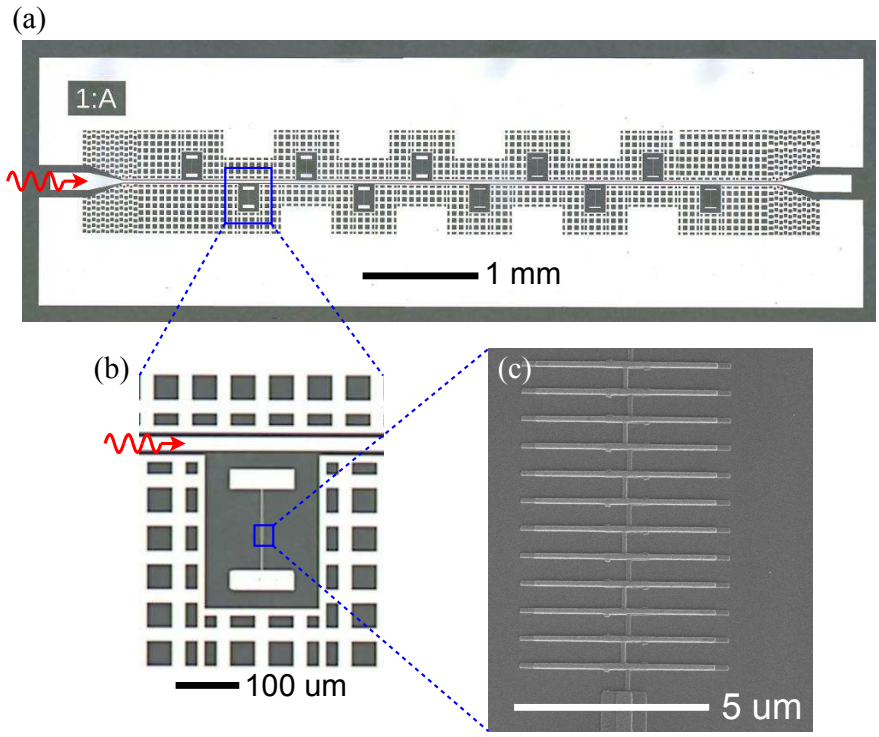

Figure 1.33: (a) Optical microscope image of the sapphire chip containing array resonators using single arrays. In the 10 devices coupled to a CPW through line, the number of junctions in each array is swept (20, 34, 50, 64 and 80 junctions) over two different sized capacitor pads (left five are 30 μm $\times$ 90 μm, right five are 10 μm $\times$ 90 μm). Holes are placed in the aluminum film near the devices to act as flux vortex traps. (b) Close-up optical image of an array resonator, with the CPW through passing above. (c) SEM image of a typical Josephson junction array.

To perform the tests, LC resonators were fabricated where the array forms the resonator inductance. The arrays are made up of Josephson junctions 5 μm $\times$ 140 nm in size, with $E_J/E_C \simeq 180$. Pads connected to the ends of the array form the

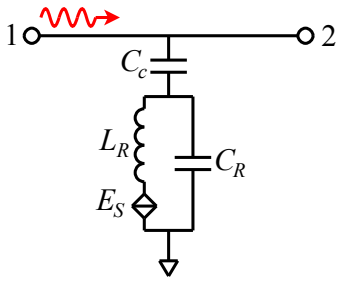

Figure 1.34: Schematic of array LC resonator. L_R and C_R are the resonator inductance and capacitance, with coupling capacitance C_c to the CPW transmission line. E_S is the characteristic energy of the phase slip element in the array.

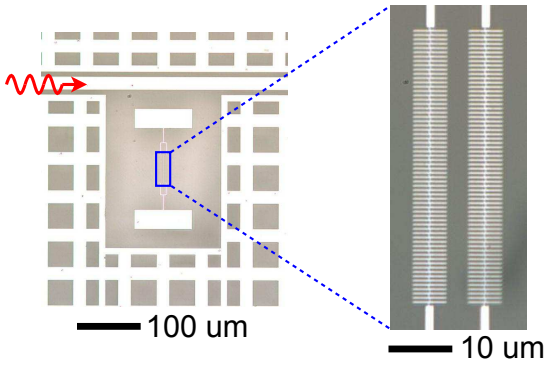

Figure 1.35: Optical microscope images of an array resonator using parallel 80-junction arrays, forming a loop.

resonator capacitance, as well as serve to couple to a coplanar waveguide (CPW) transmission line. Several resonators with varying array lengths and capacitor pad sizes were fabricated on the chip. Images of the device are shown in Figure 1.33, with the low frequency model shown in Figure 1.34. Additionally, a device with two 80-junction arrays in parallel was measured, shown in Figure 1.35. The parallel arrays form a loop, through which an external flux bias is applied. By monitoring the resonant frequency of the device with an applied flux, information is gained about the phase slip rate.

As the fabrication of fluxonium is moving towards the use of sapphire substrates, the arrays were tested on sapphire. Additionally, a bridge-free fabrication technique

was used, which allows for arbitrarily shaped junctions with very thin connecting wires. These modifications have shown a 60% reduction in parasitic capacitance to ground through computer simulations, due to the reduced use of metal deposited between junctions. An array formed using the bridge-free technique shown in Figure 1.33(c) may be compared to the array formed using the Dolan bridge technique in Figure 4.3(b). The bridge-free process and sapphire substrate also allow for more aggressive cleaning of the substrate before aluminum deposition. More information on the sample fabrication is detailed in Section 4.2.

1.4.1 Internal Loss

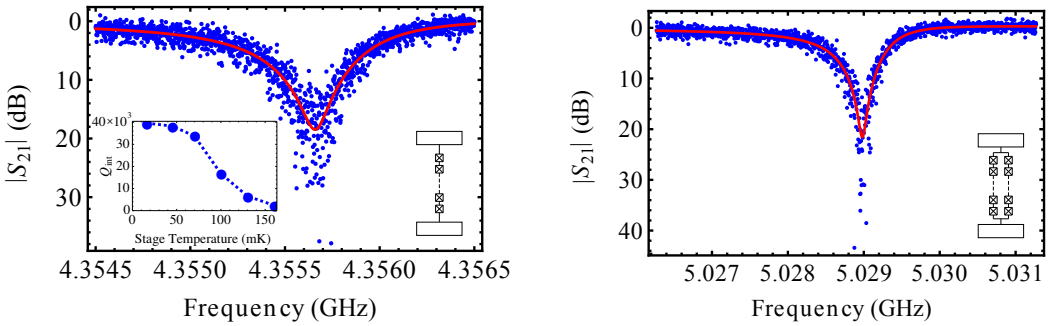

(a) (b)

Figure 1.36: Microwave transmission data for resonators containing (a) an 80-junction array and (b) two 80-junction arrays in parallel. Red lines are theory corresponding $Q_{\text{int}} > 37,000$ for (a) and $Q_{\text{int}} > 56,000$ for (b). $Q_{\text{ext}} = 5,000$ for both resonators. Measurements were taken such that on average one photon populates the resonator. The inset of (a) shows the internal quality factor of the 80-junction device versus the mixing chamber stage temperature. The saturation of internal quality factor at low temperatures may indicate the presence of non-equilibrium quasiparticles, but is likely due to the noise floor of the measurement setup.

The internal quality factor of the resonators are found through a standard transmission measurement. Measured with single photon excitation, all resonators had internal quality factors in the tens of thousands, with the data for the highest inter-

nal quality factor devices shown in Figure 1.36. Quality factors were extracted by fitting to the response function [43]

$$S_{21}(\nu) = 1 - \frac{Q_{\text{ext}}^{-1} - 2i\frac{\delta\nu}{\nu_R}}{Q_{\text{tot}}^{-1} + 2i\frac{\nu-\nu_R}{\nu_R}}, \tag{1.9}$$

where Q_{tot} and Q_{ext} are the total and external quality factors, ν_R is the resonant frequency, and $\delta\nu$ characterizes asymmetry in the transmission response profile. The internal quality factor is given by $Q_{\text{int}} = \frac{Q_{\text{ext}}Q_{\text{tot}}}{Q_{\text{ext}}-Q_{\text{tot}}}$. Since the internal quality factor of the resonator is set by both the inductive and capacitive losses, the internal loss places a lower bound on the inductive quality. Capacitive losses likely dominate, so future measurements aimed towards pushing up the inductive quality bound may consider embedding the arrays within a three-dimensional cavity resonator in bulk metal.

1.4.2 Self-resonant Frequencies

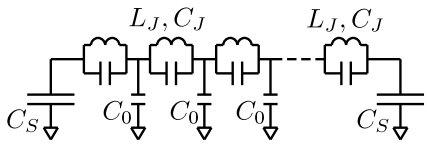

Figure 1.37: Transmission line model of the array and shunting capacitances. The Josephson junctions have an inductance L_J in parallel with a capacitance C_J. The islands between junctions have a parasitic capacitance C_0 to ground, while the ends of the array have capacitive terminations C_S from the pads.

We wish to determine the self-resonant frequency of the bare array, to ensure it functions as an inductance at our frequencies of interest (1–10 GHz). However, we have a device which has a self-resonant frequency which was deliberately lowered through the addition of shunting capacitances to form a resonator coupled to a transmission line. The array and end capacitors may be modeled as a dispersive

transmission line with capacitive terminations, as shown schematically in Figure 1.37. By measuring the first few resonant modes of the device, we may determine the values of the components in Figure 1.37, and therefore we can determine the lowest resonant mode of the bare array.

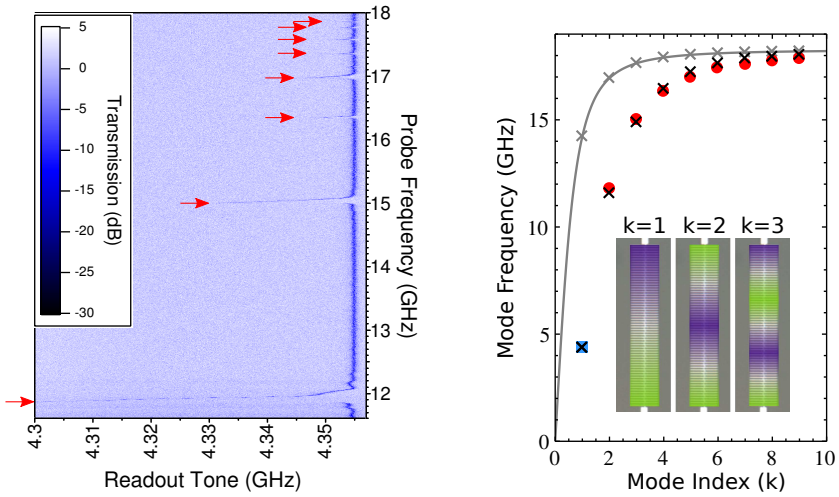

(a) (b)

Figure 1.38: (a) Shift of the fundamental ($k = 1$) mode of the 80-junction resonator in response to application of a probe tone. Drops due to excitations of higher modes are marked with red arrows. (b) Plasma mode frequencies versus mode index k of the resonances found in (a). Red circles correspond to the modes denoted with red arrows in (a), while the blue square is the fundamental resonant frequency. Black crosses show a theoretical fit to the data, while the gray curve represents theory for the dispersion relation upon removal of the array shunt capacitors C_S, leaving the ends open. The inset illustrates the voltage profile along the array for the lowest three modes.

The higher modes of the resonator may not be measured directly, as the components in the output measurment lines are out of band (see Section 4.4 for the measurement setup). Instead, the nonlinearity of the junctions was utilized to observe the excitations of higher modes through observation of shifts in the fundamental mode frequency. As a network analyzer scans across the fundamental resonance, an auxiliary probe tone is simultaneously sent to the sample. When the probe tone frequency matches a resonant mode of the array, the induced currents result in an

increase in array inductance due to junction nonlinearity. As a result, higher modes of the array are witnessed by a drop in frequency of the fundamental mode. Plasma modes up to the nineth were unambiguously identified, shown in Figure 1.38.

The calculation of plasma modes for the model in Figure 1.37 are described in Section 3.1. Using this model, the circuit parameters may be determined given the mode frequencies. The theoretical fits in Figure 1.38 were obtained with the free parameters as the array shunting capacitance $C_S = 1.2$ fF, island capacitance to ground $C_0 = 0.04$ fF, and junction inductance $L_J = 1.9$ nH. The junction capacitance $C_J = 40$ fF is inferred by the junction area, using 50 fF/μm^2 for the aluminum oxide barrier. Replacing the array shunt capacitance C_S with an open in the theory results in a dispersion relation for the bare array. This dispersion relation gives the lowest self-resonant mode of the array as 14 ± 1 GHz, which is sufficiently high for our purpose.

1.4.3 Phase Slip Rates

To measure phase slips in the arrays, a device with two 80-junction arrays in parallel was measured while sweeping a flux applied to the loop formed by the arrays. Upon application of an externally applied flux, a persistent current is induced in the loop. As a result of nonlinearity in the junctions, the inductance of the arrays increases causing the resonant frequency to decrease. This phenomena is described quasi-classically in Section 3.2. Data for this experiment is shown in Figure 1.39(a). The flux is swept to several flux quanta before phase slips become likely, with phase slips extremely rare when biased with only a couple flux quanta. The sweeps are taken over the course of several hours, with only 1–2 phase slips occurring per hour. The extremely low phase slip observed is well under 1 mHz, significantly less than previously measured phase slip rates in arrays [64, 33], and effectively solves the

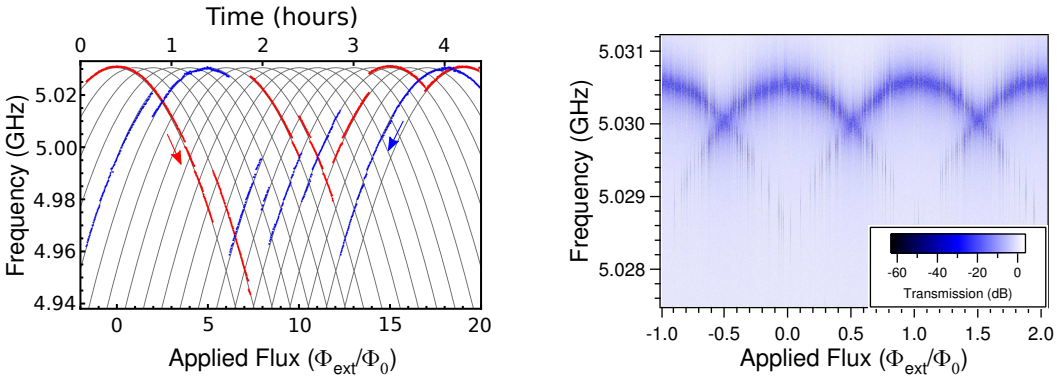

Figure 1.39: (a) Fundamental mode frequency of 160-junction array loop device versus externally applied flux. Flux bias was swept up (red) and down (blue) over the course of several hours. Gray lines are theoretical curves for the frequency with different integer number of flux quanta in the loop. As flux is swept, the resonant frequency follows one of the curves until a phase slip causes one or more quanta of flux to enter or leave the loop. (b) Data for the same experiment as performed in (a), but with the addition of a high-powered microwave pulse applied at one of the plasma modes of the array before each measurement. The pulse causes the resonator to reset into the lowest flux state.

phase slip problem in fluxonium.

To perform unambiguous calibration of the flux bias, a similar experiment was performed with the addition of a high-power microwave pulse before measurement. The microwave pulse was applied near the $k = 6$ mode at 17.0 GHz, which has the effect of resetting the device into the lowest flux state. The resultant data, shown in Figure 1.39(b), clearly demonstrates flux quantization in the loop. Interestingly, by applying microwave pulses at the $k = 3$ and $k = 4$ modes it was found that flux states may be excited. This unexpected phenomena has possible applications for tunable resonators and biasing of qubits without DC lines, and is discussed further in Section 3.3.

1.5 Concluding Words

We have provided, in the work described in this thesis, evidence that shared inductance between the qubit and readout resonator is a viable qubit-readout coupling method, which reduces the qubit's coupling to dielectric losses on the surface of the silicon substrate. Further decoupling to surface losses may be obtained by adopting a three-dimensional readout cavity. The quasiparticle losses which appear in the inductively coupled sample indicate the need for heavier filtering of microwave lines and shielding of samples. Heavier filtering and shielding, as well as three-dimensional cavity readouts, have been implemented in the latest fluxonium experiments. Recent fluxonium samples also integrate the same style Josephson junction array superinductances on sapphire which have been tested to show the low loss, high self-resonant frequencies, and low phase slip rates that fluxonium requires. Measurements performed at Yale as this thesis is edited indicate that the relaxation rate of fluxonium may have the potential to surpass that of other presently developed superconducting qubits. When sufficiently high relaxation times are readily achieved in fluxonium, topologically protected qubit designs may be explored to increase the coherence time [65].

Chapter 2

Fluxonium Theory

2.1 Computing Energies, Wavefunctions and Matrix Elements

The Hamiltonian of the fluxonium qubit is given by Equation (1.7). For the purpose of numerically computing the wavefunctions and matrix elements of fluxonium, it is simpler to start off in the plasmon (harmonic oscillator) basis where we temporarily ignore the E_J term, so that we are left with an ordinary LC oscillator of the form

$$H = 4E_C\hat{n}^2 + \frac{E_L}{2}\hat{\varphi}^2. \tag{2.1}$$

At very high energy levels, the fluxonium wavefunctions approach those of the harmonic oscillator wavefunctions, as the corregations in the potential from the Josephson term become irrelevant. The commutation relation is for phase and charge is

$$[\hat{\varphi}, \hat{n}] = i, \tag{2.2}$$

and

$$\hat{n} = -i\frac{\partial}{\partial\varphi}. \tag{2.3}$$

In the phase basis, we have a harmonic oscillator given by

$$H = -4E_C\frac{\partial^2}{\partial\varphi^2} + \frac{E_L}{2}\varphi^2. \tag{2.4}$$

The solutions to the harmonic oscillator are Hermite polynomials [66]

$$\psi_l(\varphi) = \frac{1}{\sqrt{2^l l!\sqrt{\pi}\phi_0}}\mathrm{e}^{-\frac{1}{2}\left(\frac{\varphi}{\phi_0}\right)^2}H_l(\varphi/\phi_0), \tag{2.5}$$

where l is the state (ground state is $l = 0$), and ϕ_0 is the zero point motion

$$\phi_0 = \left(\frac{8E_C}{E_L}\right)^{1/4}. \tag{2.6}$$

The eigenenergies of the harmonic oscillator are given by

$$E_l = \hbar\omega_p\left(l + \frac{1}{2}\right), \tag{2.7}$$

where $\hbar\omega_p = \sqrt{8E_LE_C}$.

To build up the Hamiltonian matrix for fluxonium in the plasmon basis, the harmonic oscillator eigenenergies form the diagonal elements. The Josephson term in the Hamiltonian produces off-diagonal ($l \neq m$) elements

$$\begin{aligned}&\left\langle\psi_m(\varphi)\left|E_J\cos\left(\hat{\varphi} - 2\pi\frac{\Phi_{\text{ext}}}{\Phi_0}\right)\right|\psi_l(\varphi)\right\rangle \\ &= \begin{cases} E_J\sin\left(2\pi\frac{\Phi_{\text{ext}}}{\Phi_0}\right)\langle\psi_m(\varphi)|\sin\hat{\varphi}|\psi_l(\varphi)\rangle, & \text{if } l+m \text{ odd} \\ E_J\cos\left(2\pi\frac{\Phi_{\text{ext}}}{\Phi_0}\right)\langle\psi_m(\varphi)|\cos\hat{\varphi}|\psi_l(\varphi)\rangle, & \text{if } l+m \text{ even} \end{cases}\end{aligned} \tag{2.8}$$

where $\psi_n(\varphi)$ are the plasmon wavefunctions, and the trigonometric identity $\cos(a-b) = \sin(a)\sin(b) + \cos(a)\cos(b)$ was applied, and the elements split by symmetry. The integrals evaluate to [67]

$$\begin{aligned}&\langle\psi_m(\varphi)|\sin\hat{\varphi}|\psi_l(\varphi)\rangle = \\ &\frac{1}{\sqrt{2^{l+m}l!m!}}2^{\mathrm{Min}[l,m]}(\mathrm{Min}[l,m])!(-1)^{(|m-l|-1)/2}\phi_0^{|m-l|}\mathrm{e}^{-\phi_0^2/4}L_{\mathrm{Min}[l,m]}^{|m-l|}\left(\frac{\phi_0^2}{2}\right),\end{aligned} \tag{2.9}$$

and

$$\begin{aligned}&\langle\psi_m(\varphi)|\cos\hat{\varphi}|\psi_l(\varphi)\rangle = \\ &\frac{1}{\sqrt{2^{l+m}l!m!}}2^{\mathrm{Min}[l,m]}(\mathrm{Min}[l,m])!(-1)^{|m-l|/2}\phi_0^{|m-l|}\mathrm{e}^{-\phi_0^2/4}L_{\mathrm{Min}[l,m]}^{|m-l|}\left(\frac{\phi_0^2}{2}\right),\end{aligned} \tag{2.10}$$

where $L_n^k(x)$ are the associated Laguerre polynomials.

Typically, a 50×50 Hamiltonian matrix is built up, which is sufficiently large that the fluxonium Hamiltonian is well approximated for the lowest levels, but not so large that computations are impractically slow. The Hamiltonian in the plasmon basis is then diagonalized to produce the Hamiltonian in the fluxonium basis. The diagonal elements give the fluxonium eigenenergies, while the eigenvectors give the coefficients to construct the fluxonium wavefunctions from the plasmon wavefunctions in Equation (2.5).

With the fluxonium wavefunctions in hand, we may now compute the phase and charge matrix elements. Since the fluxonium wavefunctions are given as linear combinations of harmonic oscillator wavefunctions, it is useful to have the phase and charge operators in terms of the harmonic oscillator ladder operators. The harmonic oscillator ladder operators are given by

$$\hat{a}_\pm = \left(\frac{2E_C}{E_L}\right)^{1/4}\left(\mp i\hat{n} + \sqrt{\frac{E_L}{8E_C}}\hat{\varphi}\right). \tag{2.11}$$

Using the ladder operators, the phase and charge operators are

$$\hat{\varphi} = \frac{1}{\sqrt{2}} \left(\frac{8E_C}{E_L} \right)^{1/4} (\hat{a} + \hat{a}^\dagger), \tag{2.12}$$

and

$$\hat{n} = \frac{i}{\sqrt{2}} \left(\frac{E_L}{8E_C} \right)^{1/4} (\hat{a}^\dagger - \hat{a}), \tag{2.13}$$

where $\hat{a} = \hat{a}_-, \hat{a}^\dagger = \hat{a}_+$.

A simple relationship exists between the phase and charge matrix elements. By taking the derivative of the phase matrix element, one obtains

$$\begin{aligned} \frac{d}{dt}\langle\beta|\hat{\varphi}|\alpha\rangle &= \frac{d}{dt}\langle\beta|\frac{2e}{\hbar}\hat{\Phi}|\alpha\rangle \\ &= \frac{2e}{\hbar}\langle\beta|\hat{V}|\alpha\rangle \\ &= \frac{(2e)^2}{\hbar C_\Sigma}\langle\beta|\hat{n}|\alpha\rangle, \end{aligned} \tag{2.14}$$

where $\hat{V} = \frac{2e}{C_\Sigma}\hat{n}$ is the voltage operator across the qubit, and α and β are states of the qubit. Additionally, the time derivative of the expectation value of an observable $\hat{A}$ is given by [68]

$$\frac{d}{dt}\langle\hat{A}\rangle = \frac{i}{\hbar}\langle[\hat{H}, \hat{A}]\rangle + \left\langle \frac{\partial \hat{A}}{\partial t} \right\rangle, \tag{2.15}$$

so

$$\begin{aligned} \frac{d}{dt}\langle\beta|\hat{\varphi}|\alpha\rangle &= \frac{i}{h}\langle\beta|\hat{H}\hat{\varphi} - \hat{\varphi}\hat{H}|\alpha\rangle \\ &= \frac{i}{h}(E_\beta - E_\alpha)\langle\beta|\hat{\varphi}|\alpha\rangle \\ &= i\omega_{\beta\alpha}\langle\beta|\hat{\varphi}|\alpha\rangle. \end{aligned} \tag{2.16}$$

Equating Equation (2.14) and Equation (2.16) we obtain the simple relation between

the phase and charge matrix elements

$$\hat{\varphi}_{\beta\alpha} = \frac{(2e)^2}{i\hbar\omega_{\beta\alpha}C_\Sigma}\hat{n}_{\beta\alpha}. \tag{2.17}$$

So, given one matrix element, the corresponding matrix element for the conjugate variable may be readily obtained without directly computing it.

2.2 Fluxonium to Readout Resonator Coupling

In order for the fluxonium atom to have some practical use in experiments, we require a way to probe the state of the qubit. This is achieved through coupling the qubit to a microwave resonator. The state-dependent impedance of the qubit loads the readout resonator, resulting in slight shifts in the resonant frequency of the resonator. By sending in microwave pulses near the resonant frequency of the resonator, the phase of the reflected pulse contains information about the state of the qubit.

2.2.1 Capacitive Coupling to a Resonator

A schematic of a fluxonium qubit capacitively coupled to a quarter wavelength balanced transmission line resonator is shown in Figure 2.3. This method of coupling was used in samples 1–4, and the physical implementation can be seen in Figure 4.1. The qubit is coupled to the open end of the resonator through coupling capacitors C_c. Since coupling capacitors are used on both ends of the resonator, the total coupling capacitance is $C_c/2$. The resonator is coupled to differential 50 Ω ports in the external measurement setup through coupling capacitances C_e.

The transmission line resonator will be modeled as a single mode resonator. In this model, the resonator can be replaced with an effective LC oscillator with angular

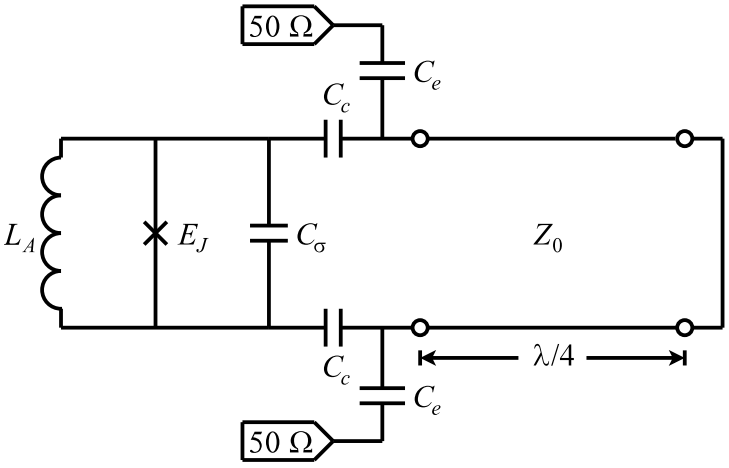

Figure 2.1: Fluxonium capacitively coupled to a quarter wavelength transmission line resonator.

resonant frequency ω_R. The bare fluxonium Hamiltonian (Equation (1.7)) picks up two additional terms with the addition of the readout resonator, the energy due to photons in the resonator,

$$\hat{H}_r = \hbar\omega_R \hat{a}^\dagger \hat{a}, \tag{2.18}$$

and the coupling Hamiltonian

$$\hat{H}_c = -g\hat{n}(\hat{a} + \hat{a}^\dagger), \tag{2.19}$$

giving the full Hamiltonian for the fluxonium circuit

$$\hat{H} = 4E_C\hat{n}^2 + \frac{1}{2}E_L\hat{\varphi}^2 - E_J\cos\left(\hat{\varphi} - 2\pi\frac{\Phi_{\text{ext}}}{\Phi_0}\right) + \hbar\omega_R\hat{a}^\dagger\hat{a} - g\hat{n}(\hat{a} + \hat{a}^\dagger). \tag{2.20}$$

For a qubit coupled to a resonator through a coupling capacitance $C_c/2$ (two capacitors of value C_c in series, to match Figure 2.3), the coupling Hamiltonian may we written as

$$-g\hat{n}(\hat{a} + \hat{a}^\dagger) = -2e\hat{n}\frac{C_c}{2C_\Sigma}V_0(\hat{a} + \hat{a}^\dagger), \tag{2.21}$$

where $-2e\hat{n}$ is the operator for charge across the qubit, and $V_0(\hat{a}+\hat{a}^\dagger)$ is the voltage across the resonator at the location where the qubit is being coupled (the voltage anti-node). The $\frac{C_c}{2C_\Sigma}$ term can be thought of as either a voltage divider for V_0, giving the potential which is applied to the charge across the qubit, or as the fraction of charge provided by the qubit which ends up on the coupling capacitors and sees the full resonator potential. C_Σ is the total shunt capacitance across the qubit, which includes contributions from the small junction capacitance, coupling capacitors, junction and stray capacitance in the array, as well as stray capacitance of the leads in the qubit, and is most easily obtained from the charging energy, $C_\Sigma = e^2/(2E_C)$. The shunting capacitance C_σ shown in Figure 2.3 is the total shunt capacitance excluding that which is due to the coupling capacitors ($C_\sigma = C_\Sigma - C_c/2$). V_0 is the RMS voltage across the resonator due to vacuum fluctuations. It is given by the half-photon vacuum energy, which is shared between the inductive and capacitive parts of the resonator ($\frac{1}{2}C_R V_0^2 = \frac{1}{4}\hbar\omega_R$):

$$V_0 = \sqrt{\hbar\omega_R}2C_R = \omega_R\sqrt{\frac{\hbar}{2}Z_R}. \tag{2.22}$$

The coupling constant can be written as

$$g = \hbar\omega_R\frac{C_c}{2C_\Sigma}\sqrt{\frac{1}{2}\frac{Z_R}{R_Q}}. \tag{2.23}$$

In the case of a quarter wavelength transmission line resonator where the transmission line has characteristic impedance Z_0, the equivalent LC oscillator with matching resonant frequency and voltage at single photon excitation has an impedance $Z_R =$

$\frac{4}{\pi}Z_0$ (see Appendix A.1, Equation (A.25)). Applying this, the coupling constant is

$$g = \hbar\omega_R \frac{C_c}{2C_\Sigma}\sqrt{\frac{2}{\pi}\frac{Z_0}{R_Q}}. \tag{2.24}$$

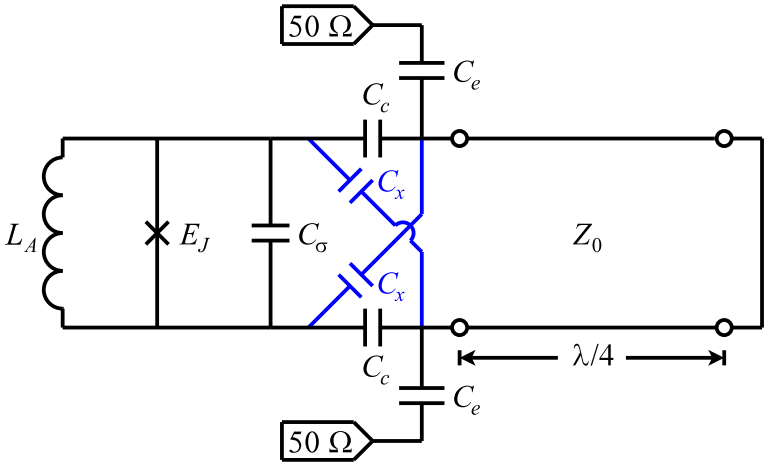

Figure 2.2: Fluxonium capacitively coupled to a quarter wavelength transmission line resonator, showing the addition of cross coupling capacitances C_x in blue.

Depending on the geometry of the qubit to readout coupling capacitors used, there may be significant cross coupling capacitances. The addition of cross coupling is shown schematically in Figure 2.2. The cross coupling will reduce the coupling between the qubit and readout. To include the effect of the cross coupling capacitances, the capacitive divider $\frac{C_c}{2C_\Sigma}$ used above must be replaced with $\frac{C_c - C_x}{2C_\sigma + C_c + C_x}$ (this is worked out through standard circuit theory).

2.2.2 Inductive Coupling to a Resonator

In the inductive coupling scheme utilized in sample 5, shown schematically in Figure 2.3, inductances L_C were placed in series with a quarter wavelength balanced transmission line resonator. The physical implementation is shown in Figure 4.2. One of the inductances is shared with the loop of the qubit, coupling the qubit and

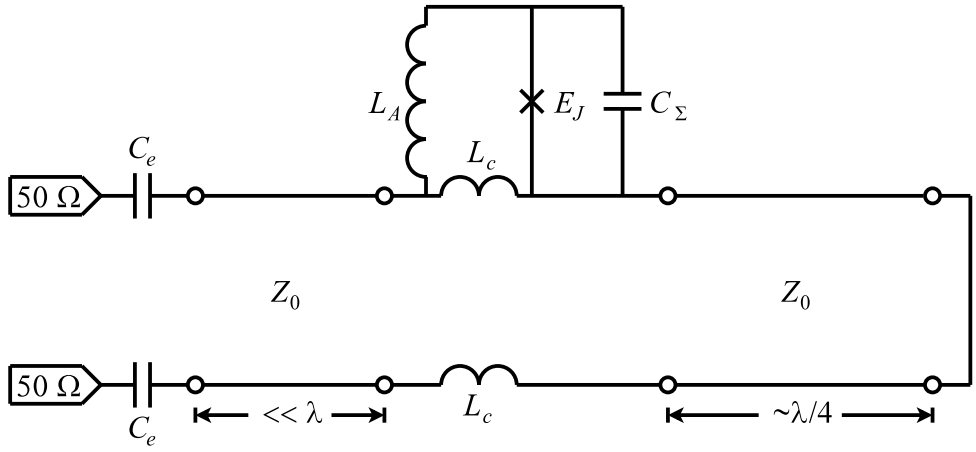

Figure 2.3: Fluxonium inductively coupled to a quarter wavelength transmission line resonator.

resonator. The other inductance is for symmetry to keep the resonator balanced.

Given a quarter wavelength resonator, the closer the coupling inductances are inserted to the short, the stronger the coupling due to the higher currents in the resonator. The mode frequencies of the resonator are also more highly modified by the insertion of the inductance, dropping the readout frequency. In sample 5, the coupling inductance was implemented with the largest sized Josephson junction that could be reliably fabricated using the Dolan bridge technique, while producing all other junctions in the device in a single double-angle evaporation step. In order not to approach the critical current of the junction too closely when the readout is driven, the coupling inductances were placed very near the open end of the resonator. The shorted segment of the resonator consisted of a length of transmission line slightly less than a quarter wavelength, and the open ended segment of the resonator was much shorter than a wavelength. Like the capacitively coupled fluxonium, the readout resonator is driven differentially through external coupling capacitors C_e via 50 Ω microwave ports. Further details on the resonator design discussed in Subsection 2.2.6.

In analogy with Equation (2.21), the coupling term in the Hamiltonian for a qubit coupled to a resonator through a shared inductance L_C is given by

$$\hat{H}_c = -g\hat{\varphi}(\hat{a} + \hat{a}^\dagger) = -\phi_0\hat{\varphi}\frac{L_c}{L_\Sigma}\eta_I I_0(\hat{a}^\dagger - \hat{a}), \tag{2.25}$$

where $-\phi_0\hat{\varphi}\frac{L_c}{L_\Sigma}$ is the operator for flux across the coupling inductance, and $\eta_I I_0(\hat{a}^\dagger - \hat{a})$ is the operator for current through the resonator at the location where the coupling inductance is located. $L_\Sigma = L_A + L_c$ is the total shunt inductance across the small junction. The term $\frac{L_c}{L_\Sigma}$ can be thought of as a current divider for $\eta_I I_0$, giving the current which is driven through the qubit. Alternatively, it can be thought of as the fraction of flux provided by the qubit which is seen across L_c. η_I is the ratio of the current at the coupling inductance location to the anti-node current. I_0 is the RMS current through the resonator at the current anti-node due to vacuum fluctuations of a half-photon of energy shared between the inductive and capacitive parts of the resonator ($\frac{1}{2}L_R I_0^2 = \frac{1}{4}\hbar\omega_R$), and is given by

$$I_0 = \sqrt{\hbar\omega_R}2L_R = \omega_R\sqrt{\frac{\hbar}{2Z_R}}. \tag{2.26}$$

The coupling constant can be written as

$$g = \hbar\omega_R\frac{L_c}{L_\Sigma}\eta_I\sqrt{\frac{1}{2}\frac{R_Q}{Z_R}}. \tag{2.27}$$

Approximating the resonator as a single-mode LC oscillator (see Appendix A.1) the resonator impedance is given by $Z_R = \frac{\pi}{4}Z_0$ (Equation (A.20)). Applying this, the coupling constant is

$$g = \hbar\omega_R\frac{L_c}{L_\Sigma}\eta_I\sqrt{\frac{1}{2}\frac{4R_Q}{\pi Z_0}}. \tag{2.28}$$

2.2.3 Dispersive Shift (Capacitive Coupling)

With the qubit in state α and resonator in state l, the presence of coupling between the qubit and resonator will modify the total system energy. When the qubit and resonator are detuned from one another, this modification can be found with second order perturbation theory. Let the unperturbed (uncoupled) eigenstates be represented by $\mid \alpha, l\rangle$, and unperturbed eigenenergy be represented by $E^0_{\alpha,l} = E_\alpha + l\hbar\omega_R$, where E_α is the qubit eigenenergy and ω_R is the resonator angular frequency ($\omega_R = 2\pi\nu_R$, where ν_R is frequency). The coupled eigenstates are given by $E_{\alpha,l} = E^0_{\alpha,l} + \delta E_{\alpha,l}$, where the change in energy due to the coupling Hamiltonian (Equation (2.19)) is

$$\begin{aligned}\delta E_{\alpha,l} &= \sum_{\substack{\beta\neq\alpha \\ m\neq l}} \frac{\left|\langle\beta, m \mid g\hat{n}(\hat{a}+\hat{a}^\dagger) \mid \alpha, l\rangle\right|^2}{E^0_{\alpha,l} - E^0_{\beta,m}} \\ &= \sum_{\beta\neq\alpha} g^2|n_{\alpha\beta}|^2 \frac{2lE_{\alpha\beta} + E_{\alpha\beta} + \hbar\omega_R}{E^2_{\alpha\beta} - (\hbar\omega_R)^2},\end{aligned} \tag{2.29}$$

where $E_{\alpha\beta} = E_\alpha - E_\beta$ is the transition energy to go from qubit state α to β. The modification in resonator transition energy due to the state of the qubit α is given by $(E_{\alpha,l+1} - E_{\alpha,l}) - \hbar\omega_R$. In other words, there is a shift in resonant frequency of the resonator due to coupling with the qubit, and this state-dependent frequency shift is given by

$$\begin{aligned}\chi_\alpha &= \frac{1}{h}(E_{\alpha,l+1} - E_{\alpha,l}) - \nu_R \\ &= \frac{1}{h} g^2 \sum_\beta |n_{\alpha\beta}|^2 \frac{2E_{\alpha\beta}}{E^2_{\alpha\beta} - (\hbar\omega_R)^2}.\end{aligned} \tag{2.30}$$

The experimentally observed shift in resonator frequency is due to transitions in qubit states

$$\chi_{\alpha\beta} = \chi_\alpha - \chi_\beta. \tag{2.31}$$

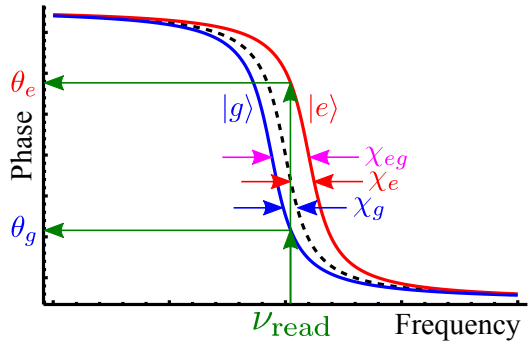

Figure 2.4: Illustration of the dispersive readout scheme. The bare resonator response is shown in dashed black, and the resonator coupled to a qubit in states g and e are shown in blue and black, respectively. ν_{read} is the readout tone frequency that is sent in (green), and the reflected tone picks up a phase θ_g or θ_e, depending on whether the qubit is in the g or e state.

The readout scheme is illustrated in Figure 2.4. When measuring the resonator shift during an experiment, a single microwave probe frequency appropriately chosen around the resonator frequency is pulsed in, and the reflected signal is observed. The shift in resonator frequency is not directly observed, rather a shift in phase is observed (in a lossless resonator, no amplitude response would be measured in a reflection measurement; however, transmission resonators may make use of amplitude response with appropriate bias of the probe frequency). This phase shift comes from the response of the resonator. A higher Q resonator will have a steeper phase response to shifts in the resonant frequency than a lower Q resonator. In general, the resonator Q should be chosen such that changes of the qubit state result in roughly a linewidth shift of the resonator. Shifts of several linewidths provide no benefit to the readability of the qubit, as maximum distinguishability occurs for phase shifts of 180°, and excessive resonator coupling to the qubit will unnecessarily couple it to the external environment more strongly.

Fluxonium is generally read out in the strongly projective regime, where each measurement consists of sampling many readout photons (typically several tens). In

this regime, a measurement will force the qubit into a single state, destroying any superposition the qubit may have been in. More details on the readout are explained in Subsection 5.1.6 and Section 5.3.

2.2.4 Dispersive Shift (Inductive Coupling)

Following the details of Subsection 2.2.3, the change in system energy due to the coupling Hamiltonian in Equation (2.25) is given by

$$\begin{aligned}\delta E_{\alpha,l} &= \sum_{\substack{\beta\neq\alpha \\ m\neq l}} \frac{\left|\langle \beta, m \mid g\hat{\varphi}(\hat{a}^\dagger - \hat{a}) \mid \alpha, l\rangle\right|^2}{E^0_{\alpha,l} - E^0_{\beta,m}} \\ &= \sum_{\beta\neq\alpha} g^2 |\varphi_{\alpha\beta}|^2 \frac{2l\hbar\omega_R + E_{\alpha\beta} + \hbar\omega_R}{E^2_{\alpha\beta} - (\hbar\omega_R)^2}.\end{aligned} \tag{2.32}$$

The dispersive shift by the qubit state α is

$$\begin{aligned}\chi_\alpha &= \frac{1}{h}(E_{\alpha,l+1} - E_{\alpha,l}) - \nu_R \\ &= \frac{1}{h} g^2 \sum_{\beta\neq\alpha} |\varphi_{\alpha\beta}|^2 \frac{2\hbar\omega_R}{E^2_{\alpha\beta} - (\hbar\omega_R)^2}.\end{aligned} \tag{2.33}$$

Using these equations in place of Equation (2.29) and Equation (2.30), the discussion of Subsection 2.2.3 otherwise holds true for inductive coupling.

2.2.5 Qubit and Readout Resonant Splittings

In typical fluxonium samples which have been measured to date, there are usually two observable resonant splittings between the resonator and qubit (the exception is sample 5, which had a readout frequency that was always between the g–e and g–f transitions). The first splitting is between the qubit in the first excited state and resonator in the ground state ($\mid e, 0\rangle$) with the qubit in the ground state and

resonator with one photon ($\mid g,1\rangle$). This is referred to as the vacuum Rabi splitting. From degenerate perturbation theory, the width of this splitting (in frequency) is

$$\begin{aligned} \nu_{\mathrm{VR}} &= 2\frac{g}{h}|n_{eg}| \quad \text{(capacitive coupling)} \\ \nu_{\mathrm{VR}} &= 2\frac{g}{h}|\varphi_{eg}| \quad \text{(inductive coupling)}, \end{aligned} \tag{2.34}$$

where n_{eg} is taken at the flux bias where the modes are degenerate.

The second splitting which is experimentally observed is between the qubit in the second excited state and resonator in the ground state ($\mid f,0\rangle$) with the qubit in the first excited state and resonator with one photon ($\mid e,1\rangle$). The transition from the ground state $\mid g,0\rangle$ to the state $\mid e,1\rangle$ is known as the blue sideband, and is a copy of the ground to first excited state with no readout photons, shifted up in frequency by the readout resonator frequency. The splitting between the second excited state and blue sideband is given by

$$\begin{aligned} \nu_{f,0|e,1} &= 2\frac{g}{h}|n_{fe}| \quad \text{(capacitive coupling)} \\ \nu_{f,0|e,1} &= 2\frac{g}{h}|\varphi_{fe}| \quad \text{(inductive coupling)}, \end{aligned} \tag{2.35}$$

at the flux bias where these modes are degenerate.

Using these experimentally observed splittings, it is possible to extract a value for the coupling constant, and from the coupling constant (in conjunction with the spectroscopically determined values for the qubit parameters E_L, E_J, E_C), experimentally extract the value of the qubit coupling capacitance/inductance.

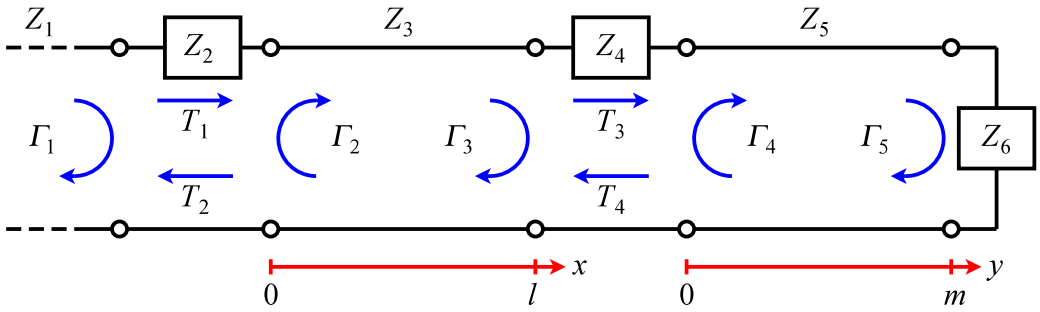

Figure 2.5: Two transmission line resonator segments, coupled through generic impedances

2.2.6 Microwave Analysis of Resonator for Inductively Coupled Fluxonium

In analyzing the resonant mode structure of the resonator used in the inductively coupled fluxonium, we will start with a general circuit detailed schematically in Figure 2.5. In the inductively coupled sample, $Z_1 = 50\ \Omega$ is the external measurement lines, $Z_2 = 1/(j\omega C_e)$ is the coupling capacitor to the resonator, $Z_3 = Z_5$ are the coupled microstrip resonator segments terminated by a short ($Z_6 = 0$), and $Z_4 = j\omega L_c$ is the coupling inductance shared with the qubit loop.

Note that our model here is unbalanced, while our actual implementation is balanced. Our unbalanced model simply divides the balanced device along the ground plane; the other half responds in an identical and opposite way. As a result, the impedance of the resonator transmission lines we use in our model are halved, as well as the energy a photon induces in the resonator.

In the following discussion, voltages and currents represent the amplitude (peak value) of harmonic signals. V_1^+ and V_1^- are the forward and backward propagating voltages in Z_1 at the interface of Z_1 and Z_2. $V_3^+(x)$ and $V_3^-(x)$ are the forward and backward propagating voltages along Z_3, where $x = 0$ is at the interface of Z_2 and

Z_3. $V_5^+(y)$ and $V_5^-(y)$ are the forward and backward propagating voltages along Z_5, where $y = 0$ is at the interface of Z_4 and Z_5. Currents are similarly defined, where $I_n^+(z) = V_n^+(z)/Z_n$ and $I_n^-(z) = -V_n^-(z)/Z_n$. Total voltages and currents do not include a superscript "+" or "−", and are given by $V_n(z) = V_n^+(z) + V_n^-(z)$ and $I_n(z) = I_n^+(z) + I_n^-(z)$.

The reflection coefficients at the interfaces of Figure 2.5 are given by

$$\Gamma_1 = \frac{(Z_2 + Z_3) - Z_1}{(Z_2 + Z_3) + Z_1}, \tag{2.36}$$

$$\Gamma_2 = \frac{(Z_1 + Z_2) - Z_3}{(Z_1 + Z_2) + Z_3}, \tag{2.37}$$

$$\Gamma_3 = \frac{(Z_4 + Z_5) - Z_3}{(Z_4 + Z_5) + Z_3}, \tag{2.38}$$

$$\Gamma_4 = \frac{(Z_3 + Z_4) - Z_5}{(Z_3 + Z_4) + Z_5}, \tag{2.39}$$

$$\Gamma_5 = \frac{Z_6 - Z_5}{Z_6 + Z_5}. \tag{2.40}$$

The transmission coefficients may be found by looking at the voltage division between the coupling impedance and impedance of the transmission line being coupled to. For example, T_1 may be found by

$$\begin{aligned} V_3^+(0) &= T_1 V_1^+, \\ V_3^+(0) &= \frac{Z_3}{Z_2 + Z_3}(V_1^+ + V_1^-) = \frac{Z_3}{Z_2 + Z_3} V_1^+(1 + \Gamma_1), \end{aligned} \tag{2.41}$$

where $\frac{Z_3}{Z_2+Z_3}$ is a voltage divider, and $V_1^+ + V_1^-$ is the input voltage. This gives us

$$T_1 = \frac{Z_3}{Z_2 + Z_3}(1 + \Gamma_1), \tag{2.42}$$

and similarly we may find the other transmission coefficients

$$T_2 = \frac{Z_1}{Z_1 + Z_2}(1 + \Gamma_2), \tag{2.43}$$

$$T_3 = \frac{Z_5}{Z_4 + Z_5}(1 + \Gamma_3), \tag{2.44}$$

$$T_4 = \frac{Z_3}{Z_3 + Z_4}(1 + \Gamma_4). \tag{2.45}$$

Voltage Along Z_3

The voltage along Z_3, with a total length l, is given by

$$V_3(x) = V_3^+(x) + V_3^-(x), \tag{2.46}$$

where $V_3^+(x)$ and $V_3^-(x)$ each come from incoming signals V_1^+ and $V_5^-(0)$. The voltage due to V_1^+ is

$$V_3^{\mathrm{I}}(x) = V_3^{\mathrm{I},+}(x) + V_3^{\mathrm{I},-}(x), \tag{2.47}$$

and similarly the voltage due to $V_5^-(0)$ is

$$V_3^{\mathrm{V}}(x) = V_3^{\mathrm{V},+}(x) + V_3^{\mathrm{V},-}(x), \tag{2.48}$$

which sum to give the total voltage

$$V_3(x) = V_3^{\mathrm{I}}(x) + V_3^{\mathrm{V}}(x). \tag{2.49}$$

The forward and backward propagating voltages along Z_3 due to V_1^+ are given by summing all reflections, with $\beta_3 = \omega/v_{p3}$, where v_{p3} is the phase velocity on Z_3

$$\begin{aligned} V_3^{\mathrm{I},+}(x) &= V_1^+[T_1 \mathrm{e}^{-j\beta_3 x} + T_1\Gamma_3\Gamma_2 \mathrm{e}^{-2j\beta_3 l}\mathrm{e}^{-j\beta_3 x} + T_1\Gamma_3\Gamma_2\Gamma_3\Gamma_2 \mathrm{e}^{-4j\beta_3 l}\mathrm{e}^{-j\beta_3 x} + \ldots] \\ &= V_1^+ T_1 \mathrm{e}^{-j\beta_3 x}\sum_{n=0}^{\infty}(\Gamma_2\Gamma_3\mathrm{e}^{-2j\beta_3 l})^n \\ &= V_1^+ T_1 \frac{\mathrm{e}^{-j\beta_3 x}}{1-\Gamma_2\Gamma_3\mathrm{e}^{-2j\beta_3 l}}, \end{aligned} \tag{2.50}$$

and

$$\begin{aligned} V_3^{\mathrm{I},-}(x) &= V_1^+[T_1\Gamma_3\mathrm{e}^{-j\beta_3 l}\mathrm{e}^{-j\beta_3(l-x)} + T_1\Gamma_3\Gamma_2\Gamma_3\mathrm{e}^{-3j\beta_3 l}\mathrm{e}^{-j\beta_3(l-x)} \\ &\quad + T_1\Gamma_3\Gamma_2\Gamma_3\Gamma_2\Gamma_3\mathrm{e}^{-5j\beta_3 l}\mathrm{e}^{-j\beta_3(l-x)} + \ldots] \\ &= V_1^+ T_1\Gamma_3\mathrm{e}^{-j\beta_3(2l-x)}\sum_{n=0}^{\infty}(\Gamma_2\Gamma_3\mathrm{e}^{-2j\beta_3 l})^n \\ &= V_1^+ T_1 \frac{\Gamma_3\mathrm{e}^{-j\beta_3(2l-x)}}{1-\Gamma_2\Gamma_3\mathrm{e}^{-2j\beta_3 l}}. \end{aligned} \tag{2.51}$$

Using similar methods for $V_5^-(0)$ incoming signals, we obtain

$$V_3^{\mathrm{V},+}(x) = V_5^-(0)T_4\frac{\Gamma_2\mathrm{e}^{-j\beta_3(l+x)}}{1-\Gamma_2\Gamma_3\mathrm{e}^{-2j\beta_3 l}}, \tag{2.52}$$

and

$$V_3^{\mathrm{V},-}(x) = V_5^-(0)T_4\frac{\mathrm{e}^{-j\beta_3(l-x)}}{1-\Gamma_2\Gamma_3\mathrm{e}^{-2j\beta_3 l}}. \tag{2.53}$$

Voltage Along Z_5

Since Z_6 is a termination (in our case a short) rather than a transmission line, the voltage along Z_5 is only due to incoming waves from the left of Figure 2.5, originating from V_1^+. The incoming waves from Z_1 travel through Z_2, Z_3 and Z_4, before reaching

Z_5. The total transmission coefficient from Z_1 to Z_5 is given by

$$\begin{aligned} T_{1T} &= T_1 T_3 \mathrm{e}^{-j\beta_3 l} + T_1\Gamma_3\Gamma_2 T_3 \mathrm{e}^{-3j\beta_3 l} + T_1\Gamma_3\Gamma_2\Gamma_3\Gamma_2 T_3 \mathrm{e}^{-5j\beta_3 l} + \dots \\ &= T_1 T_3 \mathrm{e}^{-j\beta_3 l} \sum_{n=0}^{\infty} (\Gamma_2\Gamma_3 \mathrm{e}^{-2j\beta_3 l})^n \\ &= \frac{T_1 T_3 \mathrm{e}^{-j\beta_3 l}}{1 - \Gamma_2\Gamma_3 \mathrm{e}^{-2j\beta_3 l}}. \end{aligned} \tag{2.54}$$

The total reflection coefficient off Z_4 from Z_5 is

$$\begin{aligned} \Gamma_{4T} &= \Gamma_4 + T_4\Gamma_2 T_3 \mathrm{e}^{-2j\beta_3 l} + T_4\Gamma_2\Gamma_3\Gamma_2 T_3 \mathrm{e}^{-2j\beta_3 l} + \dots \\ &= \Gamma_4 + T_3 T_4 \Gamma_2 \mathrm{e}^{-2j\beta_3 l} \sum_{n=0}^{\infty} (\Gamma_2\Gamma_3 \mathrm{e}^{-2j\beta_3 l})^n \\ &= \Gamma_4 + \frac{T_3 T_4 \Gamma_2 \mathrm{e}^{-2j\beta_3 l}}{1 - \Gamma_2\Gamma_3 \mathrm{e}^{-2j\beta_3 l}}. \end{aligned} \tag{2.55}$$

We may now calculate the forward and backward propagating waves along Z_5 (with length m) as

$$\begin{aligned} V_5^+(y) &= V_1^+ T_{1T} \mathrm{e}^{-j\beta_5 y}[1 + \Gamma_5\Gamma_{4T}\mathrm{e}^{-2j\beta_5 m} + \dots] \\ &= V_1^+ T_{1T} \mathrm{e}^{-j\beta_5 y} \sum_{n=0}^{\infty} (\Gamma_{4T}\Gamma_5 \mathrm{e}^{-2j\beta_5 m})^n \\ &= V_1^+ T_{1T} \frac{\mathrm{e}^{-j\beta_5 y}}{1 - \Gamma_{4T}\Gamma_5 \mathrm{e}^{-2j\beta_5 m}}, \end{aligned} \tag{2.56}$$

and

$$\begin{aligned} V_5^-(y) &= V_1^+ T_{1T} \Gamma_5 \mathrm{e}^{-j\beta_5 (2m-y)}[1 + \Gamma_{4T}\Gamma_5\mathrm{e}^{-2j\beta_5 m} + \dots] \\ &= V_1^+ T_{1T} \Gamma_5 \mathrm{e}^{-j\beta_5 (2m-y)} \sum_{n=0}^{\infty} (\Gamma_{4T}\Gamma_5 \mathrm{e}^{-2j\beta_5 m})^n \\ &= V_1^+ T_{1T} \frac{\Gamma_5 \mathrm{e}^{-j\beta_5 (2m-y)}}{1 - \Gamma_{4T}\Gamma_5 \mathrm{e}^{-2j\beta_5 m}}, \end{aligned} \tag{2.57}$$

where $\beta_5 = \omega/v_{p5}$, where v_{p5} is the phase velocity on Z_5.

Total Reflection Coefficient

When measuring the resonator, the total reflection coefficient of the device, Γ_T, is what is observed. When the device is on resonance, it appears as a short, so $\Gamma_T = -1$. By finding this condition with respect to varying ω, the resonances of the device may be found. The total reflection coefficient is given by

$$\Gamma_T = \frac{Z_{2L} - Z_1}{Z_{2L} + Z_1}, \tag{2.58}$$

where

$$Z_{2L} = Z_2 + Z_3 \frac{Z_{4L} + jZ_3 \tan(\beta_3 l)}{Z_3 + jZ_{4L} \tan(\beta_3 l)}, \tag{2.59}$$

and

$$Z_{4L} = Z_4 + Z_5 \frac{Z_6 + jZ_5 \tan(\beta_5 m)}{Z_5 + jZ_6 \tan(\beta_5 m)}. \tag{2.60}$$

Quality Factor

The external quality factor of the resonator may be determined by comparing the energy stored in the resonator, versus the power lost

$$Q_{\text{ext}} = \omega_0 \frac{E_L + E_C}{P_{\text{loss}}}, \tag{2.61}$$

where ω_0 is the resonant frequency, E_L and E_C are the inductive and capacitive energy stored in the resonator ($E_L = E_C$ on resonance), and P_{loss} is the power lost by the resonator when it has total energy $E_L + E_C$.

The inductive energy is given by summing the inductive contributions of transmission lines Z_3 and Z_5, and qubit coupling inductor L_c (in Z_4)

$$E_L = \frac{1}{4} \int_0^l \frac{Z_3}{v_{p3}} |I_3(x)|^2 \, \mathrm{d}x + \frac{1}{4} L_c |I_3(l)|^2 + \frac{1}{4} \int_0^m \frac{Z_5}{v_{p5}} |I_5(y)|^2 \, \mathrm{d}y. \tag{2.62}$$

The capacitive energy is given by summing the capacitive contributions of transmission lines Z_3 and Z_5, and resonator coupling capacitor C_e (in Z_2)

$$E_C = \frac{1}{4}C_e|V_3(0) - \cancelto{0}{V_1^+(1+\Gamma_T)}|^2 + \frac{1}{4}\int_0^l \frac{1}{Z_3 v_{p3}}|V_3(x)|^2\,\mathrm{d}x + \frac{1}{4}\int_0^m \frac{1}{Z_5 v_{p5}}|V_5(y)|^2\,\mathrm{d}y, \tag{2.63}$$

where $\Gamma_T = -1$ on resonance. The power leaking from the resonator is given by

$$P_{\text{loss}} = \frac{|V_3^-(0)T_2|^2/2}{Z_1}. \tag{2.64}$$

Resonator Design

The resonator of the inductively coupled fluxonium sample was designed to have a similar external quality factor and resonant frequency to the capacitively coupled samples. The dimensions of the transmission lines match that of the capacitively coupled samples (14 μm wide with 4 μm separation). Given the impedance of the transmission lines (100 Ω differential), and the maximum size coupling junction which could be fabricated using the Dolan bridge technique [44], the coupling junction had to be inserted close to the open end of the resonator such that when the resonator is excited with a photon for readout, the current through the coupling junction does not approach the critical current too closely. However, the qubit must be coupled strongly enough that sufficient dispersive shift is achieved. The chosen design was a 51 μm long transmission line on the open end (Z_3), and 3.48 mm long transmission line on the shorted end (Z_5). By using a bridge-free technique [45, 46], larger area junctions may be fabricated, allowing the qubit to be located anywhere along the resonator. Alternatively, the kinetic inductance of a nanowire may be used in place of a junction.

The parameters of sample 5 result in the resonant mode structure displayed in

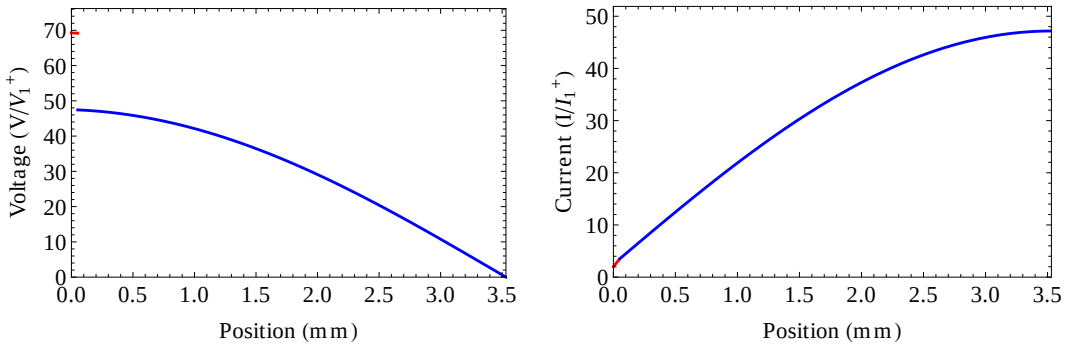

(a) (b)

Figure 2.6: (a) Voltage and (b) current resonant mode structure along the transmission lines of the inductively coupled fluxonium (sample 5), normalized to the incoming voltage V_1^+ and current I_1^+. Red represents Z_3, a 51 μm long transmission line segment, and blue represents Z_5, a 3.48 mm long transmission line shorted at the end.

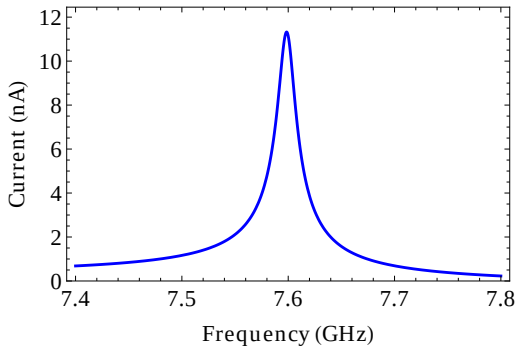

Figure 2.7: Current through the coupling junction when the resonator is probed with a power such that on resonance one photon occupies the resonator.

Figure 2.6 for the fundamental resonance at $\nu_R = 7.589$ GHz. The voltage profile is similar to that of a quarter wavelength resonator, with the exception of a sharp voltage drop across the coupling junction inductance $L_c = 6.5$ nH. The corresponding current profile has a cusp at the coupling junction. The ratio between the anti-node current and coupling junction current is $\eta_I = 0.074$. When the resonator is excited for readout, with a readout power such that one photon populates the resonator on resonance, as shown in Figure 2.7 about 11 nA flow through the coupling junction

which has a critical current of 51 nA.

2.2.7 Magnetic Coupling

The possibility of coupling magnetically between the fluxonium qubit and readout resonator is attractive, as it eliminates lossy coupling capacitors and galvanically isolates the qubit from the readout. Galvanic isolation would prevent the migration of quasiparticles that may be generated in the resonator from entering the qubit. This method was explored, however, as will be shown here, it is difficult to obtain strong coupling to the qubit.

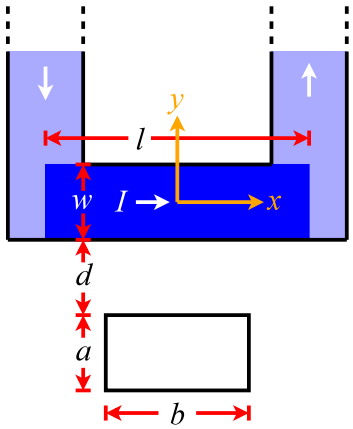

Figure 2.8: Illustration of magnetic coupling between a current carrying sheet representing the short in a quarter wavelength transmission line resonator (shown in blue, with width w and length l, with uniformly distributed current I) and rectangular loop representing a qubit ($a \times b$ in size) a distance d away. The leads of the resonator, represented here as the light blue shaded areas, may be ignored due to symmetry (assuming the qubit loop is centered with respect to the resonator short), as the magnetic fields of the left and right leads cancel.

Consider a current carrying sheet located near a loop representing the qubit, as shown in Figure 2.8. The current carrying segment may be the shorted end of a quarter wavelength transmission line resonator, with a total current I passing through (for simplicity, we will assume it is uniformly distributed across the width

w). The magnetic field generated on the x–y plane by the current carrying segment is given by the Biot-Savart law

$$B(x,y) = \frac{\mu_0}{4\pi}\frac{I}{w}\hat{z}\int_{-\frac{l}{2}}^{\frac{l}{2}}\int_{-\frac{w}{2}}^{\frac{w}{2}}\frac{y-y'}{[(x-x')^2+(y-y')^2]^{3/2}}\,\mathrm{d}y'\mathrm{d}x'$$
$$= \frac{\mu_0}{4\pi}\frac{I}{w}\hat{z}\ln\left|\frac{\left(\sqrt{\left(x-\frac{l}{2}\right)^2+\left(y+\frac{w}{2}\right)^2}+x-\frac{l}{2}\right)\left(\sqrt{\left(x+\frac{l}{2}\right)^2+\left(y-\frac{w}{2}\right)^2}+x+\frac{l}{2}\right)}{\left(\sqrt{\left(x-\frac{l}{2}\right)^2+\left(y-\frac{w}{2}\right)^2}+x-\frac{l}{2}\right)\left(\sqrt{\left(x+\frac{l}{2}\right)^2+\left(y+\frac{w}{2}\right)^2}+x+\frac{l}{2}\right)}\right|. \tag{2.65}$$

The mutual inductance between the resonator segment and qubit loop is given by the total flux in the qubit loop generated by the current in the resonator segment

$$M = \frac{\Phi_{\mathrm{loop}}}{I} = \frac{1}{I}\int_{-\frac{b}{2}}^{\frac{b}{2}}\int_{\frac{w}{2}+d}^{\frac{w}{2}+d+a}B(x,y)\,\mathrm{d}y\mathrm{d}x. \tag{2.66}$$

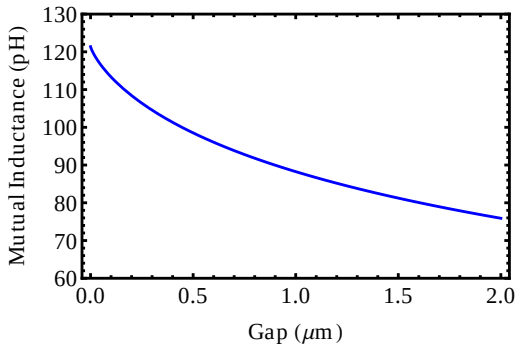

Figure 2.9: Mutual inductance versus gap between a 120 μm square loop and 122 μm long 1 μm wide current carrying segment.

The qubit loop in samples 1–5 was 2 μm × 18 μm in size. Let us consider a qubit loop much larger in area, 120 μm × 120 μm. If we place the qubit loop near a current carrying segment of conductor that is $w = 1$ μm wide, and $l = 122$ μm long, the mutual inductance obtained from Equation (2.66) versus gap d is shown in Figure 2.9. If the qubit loop is made of 500 nm wide lines (so that the outer

dimensions of the loop is a 121 μm square), and we surround the qubit loop with four of the current carrying segments to form a coupling loop such that there is a 500 nm gap between the qubit and coupling loops, the mutual inductance is 350 pH. The self inductance of the coupling loop is 490 pH, and the self inductance of the qubit loop is 550 pH.

Let's assume the coupling loop is part of an LC oscillator, with an impedance $Z_R = \sqrt{L/C} = 50\ \Omega$ and resonant frequency of 8 GHz. From Equation (2.27) we obtain a coupling constant of $g/h = 31$ MHz, where $\eta_I = 1$, $L_c = 350$ pH and $L_\Sigma = L_A + 550$ pH, where we take the array inductance to be $L_A = 290$ nH to match sample 5 (the inductively coupled sample). In comparison, sample 5 had a coupling constant of $g/h = 45$ MHz. Since the disperisve shift goes as g^2, if the magnetically coupled sample had a qubit with parameters identical to sample 5, this would result in a device with half the dispersive shift, which is still strong enough to measure.

However, the qubit loop area is 400 times larger, making it much more susceptible to picking up flux noise. Additionally, to maximize the mutual inductance we are assuming the qubit loop is only 500 nm away from the resonator coupling loop, which may pose fabrication problems. Spiral inductors will only have moderate increases in mutual inductance, but not enough to reduce the loop size to the usual area, and they would also complicate fabrication. Three-dimensional readout cavity architecture are in an even worse situation, as the resonator current is spread along the perimeter of the cavity, rather than localized to a wire as on planar resonators. Given these issues, it does not seem likely that magnetic coupling is a practical option unless some clever solution to significantly increase the mutual inductance is devised.

2.3 Relaxation Mechanisms

Energy relaxation in fluxonium may be modeled as the phase across the small junction coupling to a source of dissipation. The coupling Hamiltonian between the qubit and some lossy environment is given by

$$H_{\text{env}} = -\hat{\Phi}\hat{I}_{\text{env}} = -\phi_0\hat{\varphi}\hat{I}_{\text{env}}. \tag{2.67}$$

From Fermi's golden rule, the transition rate from state e to g is

$$\begin{aligned}\Gamma^{\text{env}}_{e\to g} &= \frac{1}{\hbar^2}|\langle e \mid \hat{\Phi} \mid g\rangle|^2 S^{\text{env}}_{II}(\omega_{eg}) \\ &= \frac{1}{(2e)^2}|\langle e \mid \hat{\varphi} \mid g\rangle|^2 S^{\text{env}}_{II}(\omega_{eg}),\end{aligned} \tag{2.68}$$

where the quantum current noise spectral density is [69]

$$S^{\text{env}}_{II}(\omega_{eg}) = \hbar\omega_{eg}\text{Re}[Y_{\text{env}}(\omega_{eg})]\left(\coth\left(\frac{\hbar\omega_{eg}}{2k_BT}\right)+1\right), \tag{2.69}$$

and $\text{Re}[Y_{\text{env}}(\omega_{eg})]$ is the real part of the admittance of the lossy element connected to the qubit. Various sources of dissipation that may couple to the fluxonium qubit are outlined below. The transition rate of a particular loss source is calculated by inserting its admittance into the quantum current noise spectral density (with the exception of quasiparticle loss, which has a different coupling to the qubit).

2.3.1 Purcell Effect

The Purcell effect is the filtering of the external world through a resonator [70]. In the fluxonium circuit shown in Figure 2.3, the readout resonator is capacitively coupled to a differential pair of 50 Ω transmission lines (the external world), and

the qubit is capacitively coupled to the readout. To calculate relaxation due to the Purcell effect, we must find the admittance of the outside world as seen by the qubit. This is given by

$$Y_{\text{Purcell}}(\omega) = \left[\frac{2}{j\omega C_c} + \left(2Z_{\text{ext}} + \frac{2}{j\omega C_e}\right) \middle|\middle| Z_{\text{res}}(\omega)\right]^{-1}, \tag{2.70}$$

where C_c is the size of the coupling capacitors between the qubit and resonator, C_e is the size of the coupling capacitor between the resonator and external transmission lines of impedance $Z_{\text{ext}} = 50\ \Omega$, and Z_{res} is the resonator impedance at the location of the qubit coupling capacitors. For a lossless quarter wavelength resonator, the impedance is

$$Z_{\text{res}}(\omega) = jZ_0 \tan\left(\frac{\pi}{2}\frac{\omega}{\omega_0}\right), \tag{2.71}$$

where Z_0 is the characteristic impedance of the transmission lines making up the resonator, and ω_0 is the unloaded resonant frequency of the bare resonator.

In the following, the results of Appendix A are used extensively to obtain C_e and ω_0 from the measured resonant frequency ω_R and total quality factor Q_{tot}. We assume we are well into the overcoupled regime, where the total Q is approximately equal to the external Q, so resistance internal to the resonator is neglected. The size of the external coupling capacitors may be found using Equation (A.28) and Equation (A.32) by approximating the transmission line resonator as an LC oscillator

$$2Z_{\text{ext}} + \frac{1}{2Z_{\text{ext}}\left(\omega_R \frac{C_e^2}{2}\right)^2} = Q_{\text{tot}}\sqrt{\frac{L}{C + C_e'(\omega_R)}} \simeq Q_{\text{tot}} Z_R, \tag{2.72}$$

where Z_R is the equivalent LC oscillator impedance, and $C_e'(\omega)$ (neglected above, but used later below) is the effective shunt capacitance from C_e and Z_{ext}, given by

Equation (A.33)

$$C'_e(\omega) = \frac{C_e/2}{1 + \left(2Z_{\text{ext}}\omega\frac{C_e}{2}\right)^2}. \tag{2.73}$$

Applying Equation (A.25) ($Z_R = \frac{4}{\pi}Z_0$) and solving for C_e, we have

$$C_e = \frac{1}{\omega_R\sqrt{\frac{2}{\pi}Z_{\text{ext}}Z_0Q_{\text{tot}} - Z_{\text{ext}}^2}}. \tag{2.74}$$

Now that we have C_e, the remaining unknown quantity is the bare resonant frequency ω_0. The LC oscillator equivalent to the transmission line resonator consists of a capacitance C_R and inductance L_R. With the coupling of the resonator to the external world, there is additional shunt capacitance $C'_e(\omega)$ from the coupling capacitor loading. There is also resistive loading, but for $Q_{\text{tot}} \gg 1$ the effect on the resonant frequency is small. The loaded frequency is

$$\omega_R = \frac{1}{\sqrt{L_R(C_R + C'_e(\omega_R))}} = \frac{1}{\sqrt{\frac{1}{\omega_0^2} + L_RC'_e(\omega_R)}}. \tag{2.75}$$

Inserting Equation (A.24) ($L_R = \frac{4Z_0}{\pi\omega_0}$) and solving for ω_0, we have

$$\omega_0 = \omega_R^2\frac{2Z_0}{\pi}C'_e(\omega_R) + \sqrt{\left(\omega_R^2\frac{2Z_0}{\pi}C'_e(\omega_R)\right)^2 + \omega_R^2}. \tag{2.76}$$

2.3.2 Capacitive Loss

We can model the shunt capacitance in the qubit as having an effective dielectric with real and imaginary parts, $\epsilon(\omega) = \epsilon'(\omega) - j\epsilon''(\omega)$ (note that this is the "engineer's" dielectric constant, where the imaginary part has a minus sign, and $j = -i$), the imaginary part resulting in a source of dissipation due to dipole relaxation of bound charge in the dielectric [71]. In the frequency range of interest ($\sim$ 1–10 GHz) we will

assume $\epsilon(\omega)$ remains constant, which will result in a shunt conductance which varies linearly with frequency, as we will see below. If we think of a plate capacitor of area A and plate separation d, the admittance is given by

$$\begin{aligned} Y_{\text{cap}}(\omega) &= j\omega\epsilon\frac{A}{d} \\ &= j\omega\epsilon'\frac{A}{d} + \omega\epsilon''\frac{A}{d} \\ &= j\omega C + G(\omega). \end{aligned} \tag{2.77}$$

The lossy dielectric results in a shunt conductance which scales linearly with frequency. The quality factor (or inverse loss tangent) for the dielectric is given by the ratio of the imaginary and real parts of the admittance

$$Q_{\text{cap}} = \frac{\text{Im}[Y_{\text{cap}}(\omega)]}{\text{Re}[Y_{\text{cap}}(\omega)]} = \frac{1}{\tan\delta}. \tag{2.78}$$

Using the quality factor defined above, we may write the real part of the admittance as

$$\text{Re}[Y_{\text{cap}}(\omega)] = \frac{\omega C}{Q_{\text{cap}}}. \tag{2.79}$$

In analyzing dielectric loss in fluxonium, we characterize the total shunt capacitance across the qubit $C_\Sigma = e^2/(2E_C)$. It is not possible to break down and independently analyze the individual capacitances in a single qubit, so the best we can do is lump all losses into a single effective dielectric, and compare the overall dielectric quality between samples. If modifying one particular capacitor is found to have a consistent effect on the overall capacitive quality factor, then we may gain insight on that capacitor's contribution.

2.3.3 Inductive Loss

In analogy with the capacitive loss, we may model the shunt inductance in the qubit (in fluxonium, the shunt inductance is given by $L_\Sigma = \varphi_0^2/E_L$) as having a lossy permeability $\mu(\omega) = \mu'(\omega) - j\mu''(\omega)$ which we will take as constant for the frequency range of interest. This model results in an inductor with a frequency dependent series resistance. The impedance of the inductor is

$$\begin{aligned} Z_{\text{ind}}(\omega) &\propto j\omega\mu' + \omega\mu'' \\ Z_{\text{ind}}(\omega) &= j\omega L + R(\omega). \end{aligned} \tag{2.80}$$

The quality factor for the inductance is the ratio of the real and imaginary parts of the impedance

$$Q_{\text{ind}} = \frac{\text{Im}[Z_{\text{ind}}(\omega)]}{\text{Re}[Z_{\text{ind}}(\omega)]}. \tag{2.81}$$

Using the quality factor, the real part of the impedance is

$$\text{Re}[Z_{\text{ind}}(\omega)] = \frac{\omega L}{Q_{\text{ind}}}. \tag{2.82}$$

In order to determine the current noise spectral density, we require the real part of the admittance:

$$\begin{aligned} \text{Re}[Y_{\text{ind}}(\omega)] &= \text{Re}\left[\frac{1}{j\omega L + \text{Re}[Z_{\text{ind}}(\omega)]}\right] \\ &= \frac{1}{\omega L}\frac{1}{Q_{\text{ind}} + 1/Q_{\text{ind}}} \\ &\simeq \frac{1}{\omega L}\frac{1}{Q_{\text{ind}}}. \end{aligned} \tag{2.83}$$

The functional difference between inductive and capacitive loss is a factor of ω^2 between $\text{Re}[Y_{\text{cap}}(\omega)]$ and $\text{Re}[Y_{\text{ind}}(\omega)]$.

2.3.4 Quasiparticle Loss

The tunneling of quasiparticles across the small Josephson junction may be a source of dissipation if nonequilibrium quasiparticles are present. In thermal equilibrium the density of quasiparticles normalized to the density of Cooper-pairs, given by $x_{\rm qp}^{\rm eq} = \sqrt{2\pi k_B T/\Delta}\mathrm{e}^{-\Delta/k_B T}$, is exponentially depleted at the low temperatures used in experiments ($\Delta/k_B = 2.1$ K for aluminum, where Δ is the superconducting gap). However, nonequilibrium quasiparticles may be produced from radioactive decay of materials within the cryostat, cosmic rays, or inadequate filtering and shielding of samples from infrared or optical photons (the most likely source in present experiments). A summary of the main results from reference [72] which are useful for quantifying bounds on qusiparticle densities in this thesis work are presented in the equations below. We assume the junction has equal superconducting gaps on both sides, and $\delta E \ll \hbar\omega \ll 2\Delta$, where δE is the characteristic energy of the quasiparticles.

The transition rate due to the presence of quasiparticles is given by

$$\Gamma_{e\to g}^{\rm qp} = \left|\left\langle e\left|\sin\frac{\hat{\varphi}}{2}\right|g\right\rangle\right|^2 S_{\rm qp}(\omega_{eg}), \tag{2.84}$$

where the quasiparticle noise spectral density is

$$S_{\rm qp}(\omega) = \frac{2\hbar\omega}{e^2}\mathrm{Re}[Y_{\rm qp}(\omega)]. \tag{2.85}$$

The real part of the junction admittance due to quasiparticles is

$$\mathrm{Re}[Y_{\rm qp}(\omega)] = \frac{1}{2}x_{\rm qp}G_t\left(\frac{2\Delta}{\hbar\omega}\right)^{3/2}, \tag{2.86}$$

where the junction conductance is given by the Ambegaokar-Baratoff relation

$$G_t = \frac{8E_J}{\Delta R_K}. \tag{2.87}$$

For aluminum junctions $\Delta = 180$ μeV (note that Δ should be expressed in the same units as E_J in the above equation). We can define a frequency-dependent quality factor for the junction as

$$Q_J(\omega_{eg}) = \frac{\omega_{eg}}{\Gamma^{\rm qp}_{e\to g}}, \tag{2.88}$$

but it is simpler to quantify quasiparticle loss through the frequency-independent normalized quasiparticle density $x_{\rm qp}$.

2.3.5 Transition Efficiencies

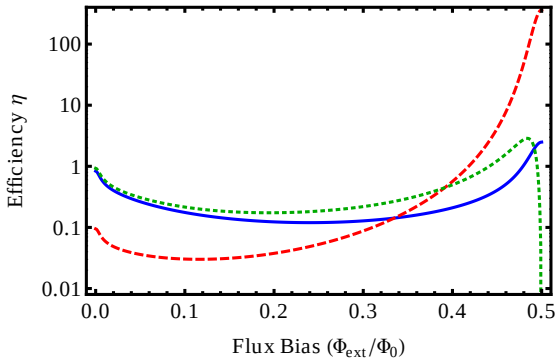

Figure 2.10: Transition efficiencies of sample 2 to capacitive loss (solid blue), inductive loss (dashed red) and quasiparticle loss (dotted green).

A convenient method of comparing the coupling strength of different qubits to various loss mechanisms is through transition efficiencies. The transition efficiency, η, is defined such that an LC oscillator has unity efficiency for capacitive and inductive loss. Given the transition efficiency and quality factor for a loss mechanism and the

g–e transition frequency, the transition rate is

$$\Gamma_{e\to g} = \frac{\omega_{eg}\eta}{Q}. \tag{2.89}$$

The transition efficiencies for sample 2 are shown in Figure 2.10.

2.4 Effect of Phase Slips in Array

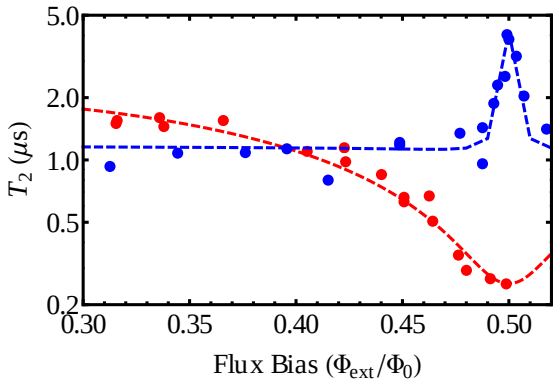

Figure 2.11: T_2 times for sample 1 (red) and sample 3 (blue) biased around $\Phi_{\text{ext}} = \Phi_0/2$. Sample 1 has the lowest T_2 times at the flux sweet spot, indicating dephasing due to phase slips in the array. Sample 1 had an array junction phase slip amplitude $E_{SA}/h = 140$ kHz, and flux noise of 0.7 $\mu\Phi_0/\sqrt{\text{Hz}}$ @ 1 Hz. Sample 3 had an array junction phase slip amplitude $E_{SA}/h = 8.8$ kHz, and flux noise of 2.5 $\mu\Phi_0/\sqrt{\text{Hz}}$ @ 1 Hz. The reason for additional flux noise in sample 3 is not clear, as the loop areas are identical, and the same magnetic shielding was used.

When the coherence times of sample 1 were measured near $\Phi_{\text{ext}} = \Phi_0/2$, it was found that T_2 times were the worst at the flux sweet spot (see Figure 2.11). The explanation for this counterintuitive result is the presence of coherent quantum phase slips (CQPS) by flux tunneling through array junctions in addition to the "weak" small junction. The total phase slip energy for the loop consists of the superposition of tunneling amplitudes for all junctions, of which the individual amplitudes have a phase that depends on the charge of the enclosed islands (islands here are the pieces

of metal between junctions). When charge on the islands between array junctions fluctuate, the result is an inhomogeneous broadening between states [33, 34] through the Aharonov-Casher effect [73]. The linewidth between the states α and β due to phase slips in the array is given by

$$\delta\nu_{\alpha\beta} = \frac{\sqrt{N}E_{SA}}{h}\left|\int_{-\infty}^{+\infty}\Psi_\alpha(\varphi)\Psi_\alpha(\varphi-2\pi)d\varphi - \int_{-\infty}^{+\infty}\Psi_\beta(\varphi)\Psi_\beta(\varphi-2\pi)d\varphi\right|, \quad (2.90)$$

where N is the number of junctions in the array, and E_{SA} is the phase slip energy of array junctions. When biased at $\Phi_{\text{ext}} = \Phi_0/2$, for states g and e the absolute value term reduces to 1, giving the linewidth of the g–e transition as $\sqrt{N}E_{SA}/h$. Moving away from $\Phi_{\text{ext}} = \Phi_0/2$, the absolute value term reduces. The linewidth translates into a dephasing rate by

$$\Gamma_{\text{CQPS}} = \sqrt{2}\pi\delta\nu_{\alpha\beta}. \quad (2.91)$$

The phase slip amplitudes of the array junctions depend exponentially on the ratio of the Josephson energy, E_{JA}, to charging energy, E_{CA} [74]

$$E_{SA} = 4\sqrt{\frac{2}{\pi}}\left(\frac{8E_{JA}}{E_{CA}}\right)^{1/4}\sqrt{8E_{JA}E_{CA}}\,\mathrm{e}^{-\sqrt{\frac{8E_{JA}}{E_{CA}}}}. \quad (2.92)$$

By increasing the E_{JA}/E_{CA} ratio a factor of 1.7 in sample 3, the T_2 times improved a factor of 16 at $\Phi_{\text{ext}} = \Phi_0/2$, as shown in Figure 2.11. This result demonstrates the importance of reducing phase slips in the array.

Away from $\Phi_{\text{ext}} = \Phi_0/2$ the response in coherence times versus flux bias is relatively flat in sample 3, indicating flux noise as the dominant source of dephasing, as the g–e transition frequency varies linearly with flux bias. The dephasing rate for

flux noise of amplitude A is given by

$$\Gamma_{\text{flux}} = 2\pi\sqrt{3}A\left|\frac{\partial\nu_{\alpha\beta}}{\partial\Phi}\right| \tag{2.93}$$

Flux noise for all samples was of the order 1 $\mu\Phi_0/\sqrt{\text{Hz}}$ @ 1 Hz, typical for superconducting devices [75].

Chapter 3

Josephson Junction Array Superinductances

3.1 Array Plasma Modes

To calculate the resonant modes of the Figure 1.37, we model the array as a transmission line with capacitive loads. The unloaded resonant frequencies of the array are given by [76]

$$\omega_k^0 = \omega_p \sqrt{\frac{1-\cos\frac{\pi k}{N}}{(1-\cos\frac{\pi k}{N})+\frac{C_0}{2C_J}}}, \tag{3.1}$$

where k is the mode number, $\omega_p = 1/\sqrt{L_J C_J}$ and N is the number of junctions in the array. The impedance of the "transmission line" is given by

$$Z_k = \frac{1}{2}\sqrt{\frac{L_J/(1-\cos\frac{\pi k}{N})}{(1-\cos\frac{\pi k}{N})+\frac{C_0}{2C_J}}}, \tag{3.2}$$

and the phase velocity is

$$v_k^0 = \frac{N\omega_k^0}{k\pi}. \tag{3.3}$$

If the transmission line is cut in half, and the impedance looking into the left and right halves is compared, the situation $\mathrm{Im}[Z_{\mathrm{left}}] = \mathrm{Im}[Z^*_{\mathrm{right}}]$ corresponds to an odd k mode resonance. Additionally, from symmetry we have $Z_{\mathrm{left}} = Z_{\mathrm{right}}$ (always true). Because the impedances are strictly imaginary, the impedance looking into the resonator section must be zero on odd k resonances. So, we have

$$Z_{\mathrm{in}} = Z_k \frac{(j\omega_k C_S)^{-1} + jZ_k \tan(\beta_k N/2)}{Z_k + j(j\omega_k C_S)^{-1} \tan(\beta_k N/2)} = 0, \tag{3.4}$$

where the propagation constant is approximated by $\beta_k = \omega_k / v_k^0$. This yields a transcendental equation which may be solved numerically to find ω_k for odd k

$$\frac{1}{\omega_k C_S Z_k} = \tan\left(\frac{\omega_k N}{2v_k^0}\right). \tag{3.5}$$

To acquire the even k resonances, the same analysis is performed for admittances

$$-\omega_k C_S Z_k = \tan\left(\frac{\omega_k N}{2v_k^0}\right). \tag{3.6}$$

3.2 Frequency Dependence on Flux of Loop Device

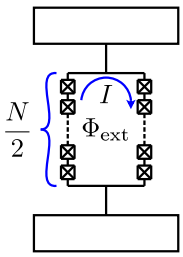

Figure 3.1: Resonator with two parallel arrays of $N/2$ junctions. An externally applied flux Φ_{ext} induces a persistent direct current I in the loop.

Here we present a quasi-classical model that predicts, to lowest order in junction nonlinearity, the frequency dependence on flux bias of the resonator which contains two parallel arrays, diagrammed in Figure 3.1. We consider the case of two identical arrays, each containing $N/2$ Josephson junctions. When an external flux bias Φ_{ext} is applied, a current I is induced in the loop. Due to the nonlinearity of the junctions, the inductance of the arrays increases, and as a result the resonant frequency of the device drops.

The direct current I flowing through the loop when an external flux bias Φ_{ext} is applied is

$$I(\Phi_{\text{ext}}) = I_c \sin\left(\frac{2\pi}{N}\frac{\Phi_{\text{ext}}}{\Phi_0}\right), \tag{3.7}$$

where I_c is the critical current of the junctions. The flux dependent inductance of each junction is

$$L_J(\Phi_{\text{ext}}) = \frac{1}{N}\left(\frac{dI}{d\Phi_{\text{ext}}}\right)^{-1} = \frac{L_{J0}}{\cos\left(\frac{2\pi}{N}\frac{\Phi_{\text{ext}}}{\Phi_0}\right)}, \tag{3.8}$$

where $L_{J0} = \phi_0/I_c$ is the Josephson inductance. We now obtain the resonant frequency of the LC oscillator formed by inductance $NL_J(\Phi_{\text{ext}})/4$ and capacitance C

$$\nu(\Phi_{\text{ext}}) = \frac{1}{2\pi\sqrt{\frac{N}{4}L_J(\Phi_{\text{ext}})C}}. \tag{3.9}$$

We may rewrite this in terms of the maximum frequency ν_R, expand the cosine for $\Phi_{\text{ext}} \ll N\Phi_0$, and add in the effect of flux quanta in the loop by replacing $\frac{\Phi_{\text{ext}}}{\Phi_0}$ with $(\frac{\Phi_{\text{ext}}}{\Phi_0} - m)$, where m the integer number of flux quanta in the loop

$$\nu(\Phi_{\text{ext}}) = \frac{\nu_R}{\sqrt{1 + \frac{1}{2}(\frac{2\pi}{N}(\frac{\Phi_{\text{ext}}}{\Phi_0} - m))^2}}. \tag{3.10}$$

3.3 Microwave Excitation and Demolition of Persistent Direct Currents

When searching for plasma modes of the array loop device, shown in Figure 1.35, it was found that when the loop was flux biased and certain probe frequencies were sent, phase slips would be induced, causing the device to settle to a lower fluxon (magnetic) state. It was found that phase slips were most reliably induced when a microwave tone was pulsed near the $k = 6$ plasma mode at 17.0 GHz. Whether the $k = 6$ mode has some special property, or that particular frequency simply happens to be better coupled to that sample is not clear. Phase slips could also be induced which cause the system to relax to the lowest fluxon state by sweeping across the fundamental resonance at very high powers with the network analyzer, however this method was not as reliable at settling into the lowest fluxon state.

But even stranger, it was discovered that sending pulses at the $k = 3$ and $k = 4$ modes (12.8 and 15.4 GHz, respectively) would excite the device from the fluxon ground state into higher fluxon states, and being very selective to which state they excite to at certain pulse power and time combinations. Several other plasma modes were explored, but only the $k = 3$ and $k = 4$ modes were found to give any response. In this unexpected effect, microwave pulses are able to both induce and remove direct currents in the array loop.

To test the power and time dependence of the microwave pulses on which states are induced, as well as the dependence on external flux bias, several trials were repeated for different parameters of the system. All experimental trials started with a reset to the lowest flux state by applying a 3 second long pulse near the $k = 6$ mode. Although the reset occasionally results in the fluxon mode $m = \pm 1$ rather than $m = 0$, no correlation was seen between the resultant state and starting in

$m = 0$ versus $m = \pm 1$ in any of the data. In the same way the data of Figure 1.39 was taken, the location of the fundamental mode frequency is determined through a network analyzer measurement. The fluxon state m may be determined by observing the resultant fundamental mode frequency through Equation 3.10.

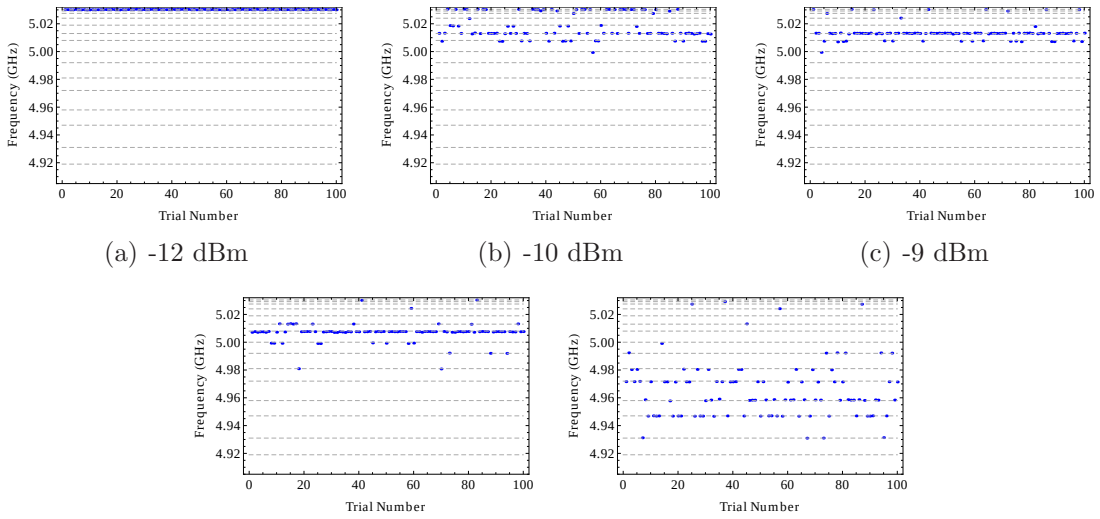

(a) -12 dBm (b) -10 dBm (c) -9 dBm

(d) -2 dBm (e) 12 dBm

Figure 3.2: Fundamental mode frequency after application of microwave a 3 second pulse at the $k = 3$ mode frequency, with $\Phi_{\text{ext}}/\Phi_0 = 0.214$. The experiment is repeated 100 times for different pulse powers, with reset to the lowest fluxon state between trials. Dashed gray lines are the locations of fundamental mode frequencies dependent on the fluxon state the loop is in.

Shown in Figure 3.2 and Figure 3.3 are repeated trials for different pulse powers sent at the $k = 3$ and $k = 4$ mode frequencies. At low powers, the pulses have little to no effect. Increasing the power results in higher and higher fluxon states being induced into the loop. At particular powers, such as shown in Figure 3.2(c) and Figure 3.2(d) for $k = 3$, and Figure 3.3(c) and Figure 3.3(d) for $k = 4$, certain fluxon states are selectively induced. The $k = 4$ plasma mode tends to have the ability to be a bit more selective than the $k = 3$ plasma mode.

The probability of each plasma mode inducing a particular fluxon state versus

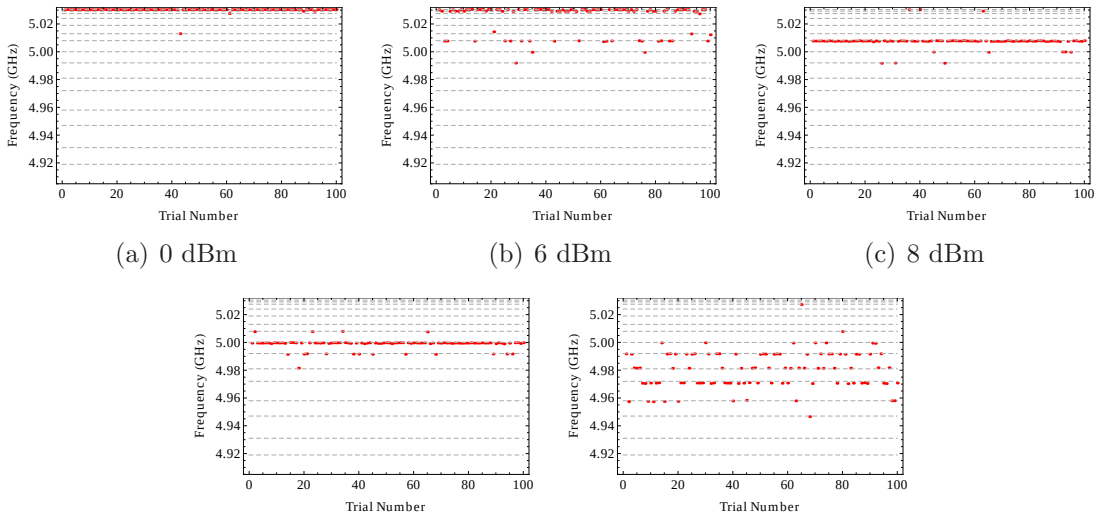

(a) 0 dBm (b) 6 dBm (c) 8 dBm

(d) 15 dBm (e) 22 dBm

Figure 3.3: Fundamental mode frequency after application of microwave a 3 second pulse at the $k = 4$ mode frequency, with $\Phi_{\text{ext}}/\Phi_0 = 0.214$. The experiment is repeated 100 times for different pulse powers, with reset to the lowest fluxon state between trials. Dashed gray lines are the locations of fundamental mode frequencies dependent on the fluxon state the loop is in.

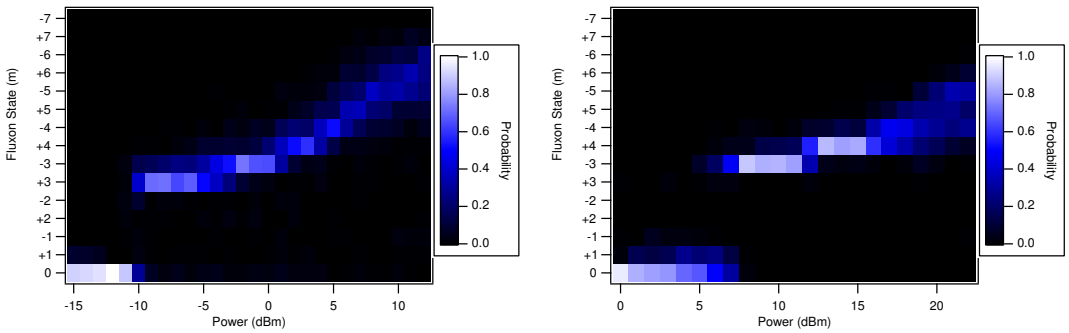

(a) $k = 3$ (b) $k = 4$

Figure 3.4: Probability of inducing m flux quanta versus power of 3 second pulses applied at the (a) $k = 3$ and (b) $k = 4$ array plasma modes, flux biased at $\Phi_{\text{ext}}/\Phi_0 = 0.214$. Each column corresponds to 100 trials at the given pulse power (values in each column sum to a probability of 1).

power of the plasma mode pulse is shown in Figure 3.4. It can be seen that pulses at the $k = 3$ mode have reasonable selectivity for the $m = \pm 3$ states, while pulses at the $k = 4$ mode can have selectivity for the $m = -3$ or $m = +4$ states. At high powers,

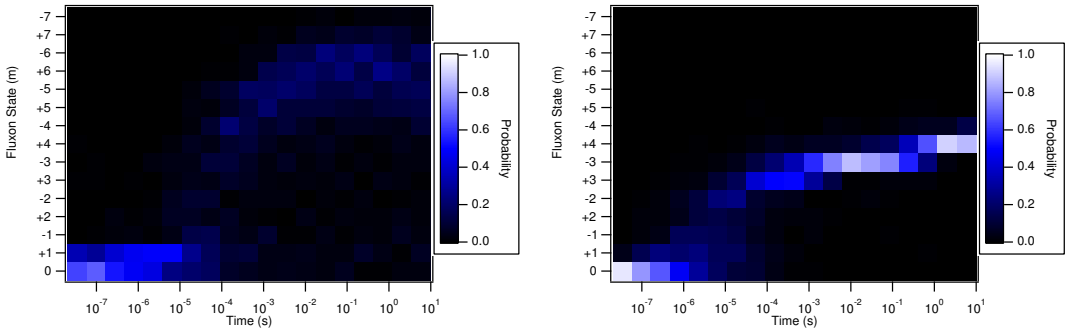

(a) $k = 3$ (b) $k = 4$

Figure 3.5: Probability of inducing m flux quanta versus time duration of 16 dBm pulses applied at the (a) $k = 3$ and (b) $k = 4$ array plasma modes, flux biased at $\Phi_{\text{ext}}/\Phi_0 = 0.214$. Each column corresponds to 100 trials at the given pulse time (values in each column sum to a probability of 1).

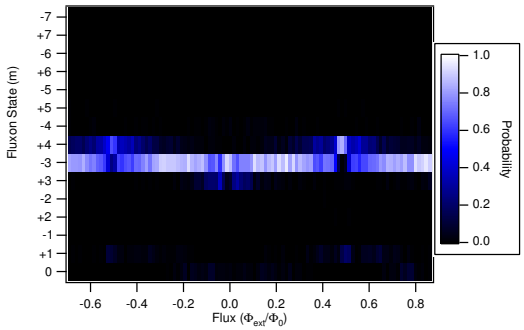

Figure 3.6: Probability of inducing m flux quanta versus flux bias after 3 second 8 dBm pulses applied at the $k = 4$ array plasma mode. Each column corresponds to 100 trials at the given flux bias (values in each column sum to a probability of 1). Note that between integer and half integer values of flux, $m = 0$ is always normalized to refer to the total number of flux quanta in the loop which minimizes the inductive energy. At integer values of flux bias, $+m$ is degenerate with $-m$, while at half integer values of flux $-m$ is degenerate with $+(m + 1)$. Due to errors in setting the exact threshold locations and noise in the data exceeding the level separations, it is not possible to distinguish between nearly degenerate m values.

pulses at both modes tend to scatter around higher fluxon states without much selectivity. Similar experiments were performed varying pulse times and external flux bias, shown in Figure 3.5 and Figure 3.6

Strangely, pulses at the $k = 4$ plasma mode were able to selectively induce the

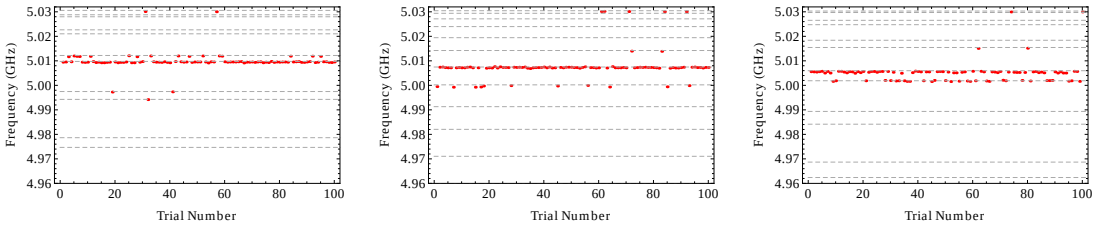

(a) $\Phi_{\text{ext}}/\Phi_0 = 0.093$ (b) $\Phi_{\text{ext}}/\Phi_0 = 0.259$ (c) $\Phi_{\text{ext}}/\Phi_0 = 0.364$

Figure 3.7: Fundamental mode frequency after application of microwave a pulse at the $k = 4$ mode frequency. The experiment is repeated 100 times for different external flux biases, with reset to the lowest fluxon state between trials. Dashed gray lines are the locations of fundamental mode frequencies dependent on the fluxon state the loop is in.

$m = -3$ fluxon state, but it is very unlikely to induce the opposite $m = +3$ state even when flux biased such that they are nearly degenerate, such as in Figure 3.7(a). At intermediate flux bias, shown in Figure 3.7(b), the $m = -3$ fluxon state may be selectively induced, but when biased near half integer flux the $m = +4$ state has a reasonable probability of being excited, as shown in Figure 3.7(c). Note that the $m = +4$ state in Figure 3.7(c) is not nearly as degenerate with $m = -3$ as the $m = +3$ state is in Figure 3.7(a).

Chapter 4

Experimental Methods

4.1 Fluxonium Sample Fabrication

The fluxonium samples measured in this thesis work were fabricated on silicon substrates. The silicon wafer was spun with dual layers of electron beam (e-beam) resist, then the wafer was cleaved before writing in an FEI Type 6634/17 30 kV SEM which was converted to allow e-beam writing using NPGS software. After writing, the sample is developed, and aluminum is deposited using double angle evaporation, with an oxidation step between evaporations. The resist is stripped away in acetone, lifting off the unwanted aluminum, and after rinsing in methanol the sample is mounted and wirebonded. The device fabrication recipes are detailed in Section B.1.

Optical images of capacitively coupled samples are shown in Figure 4.1. The qubit is coupled capacitively to the readout resonator through finger coupling capacitors (Figure 4.1(a), samples 1–3), or wider spaced capacitor pads (Figure 4.1(b), sample 4). The readout resonator is made up of a 3.5 mm long CPW transmission line (each line is 14 μm wide, with 4 μm spacing between the lines), shorted on one end to form a quarter wavelength resonator. The open end is coupled to the qubit, as

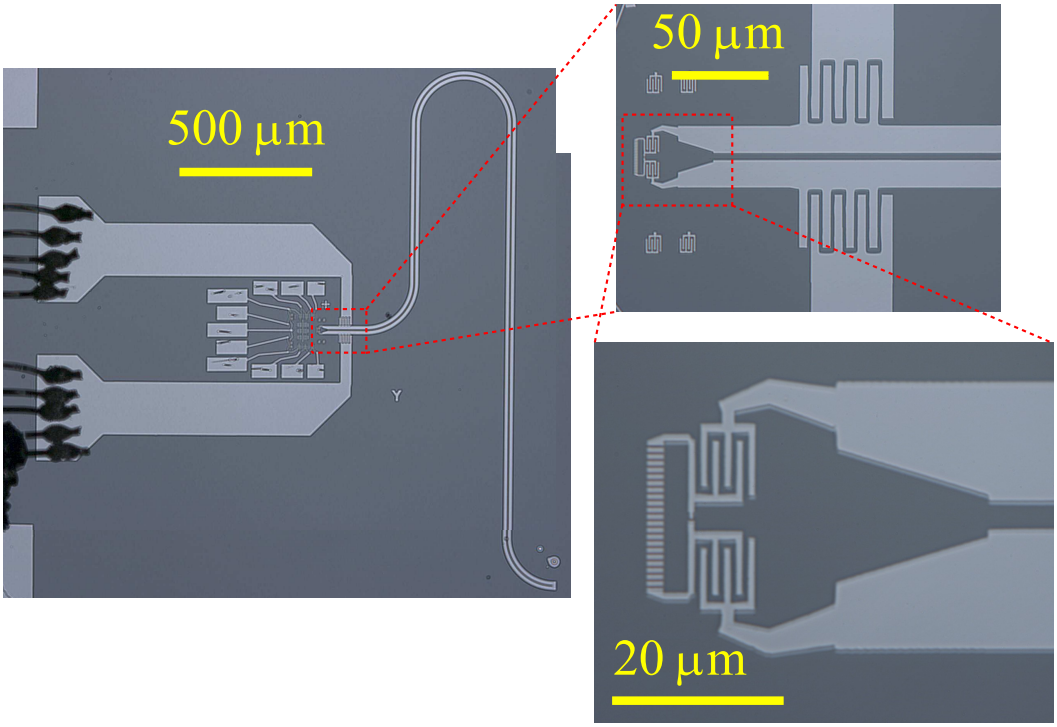

(a)

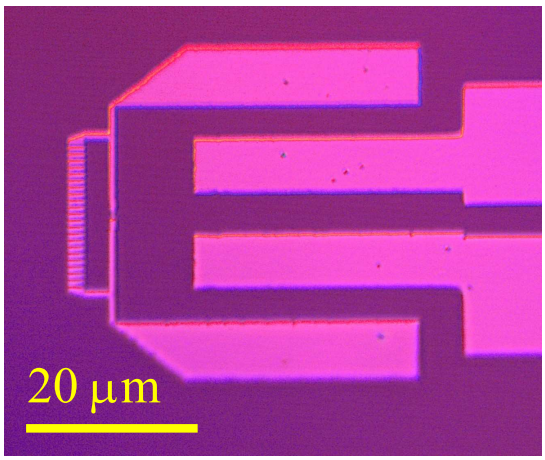

(b)

Figure 4.1: (a) Optical images of capacitively coupled sample (samples 1–4). (b) Optical image of sample 4, which used 4 μm spaced coupling capacitor pads in place of the 720 nm gap finger coupling capacitors.

well as coupled to wirebonding pads via finger coupling capacitors. The pads are wirebonded to differentially driven microstrip lines in the sample holder, which is

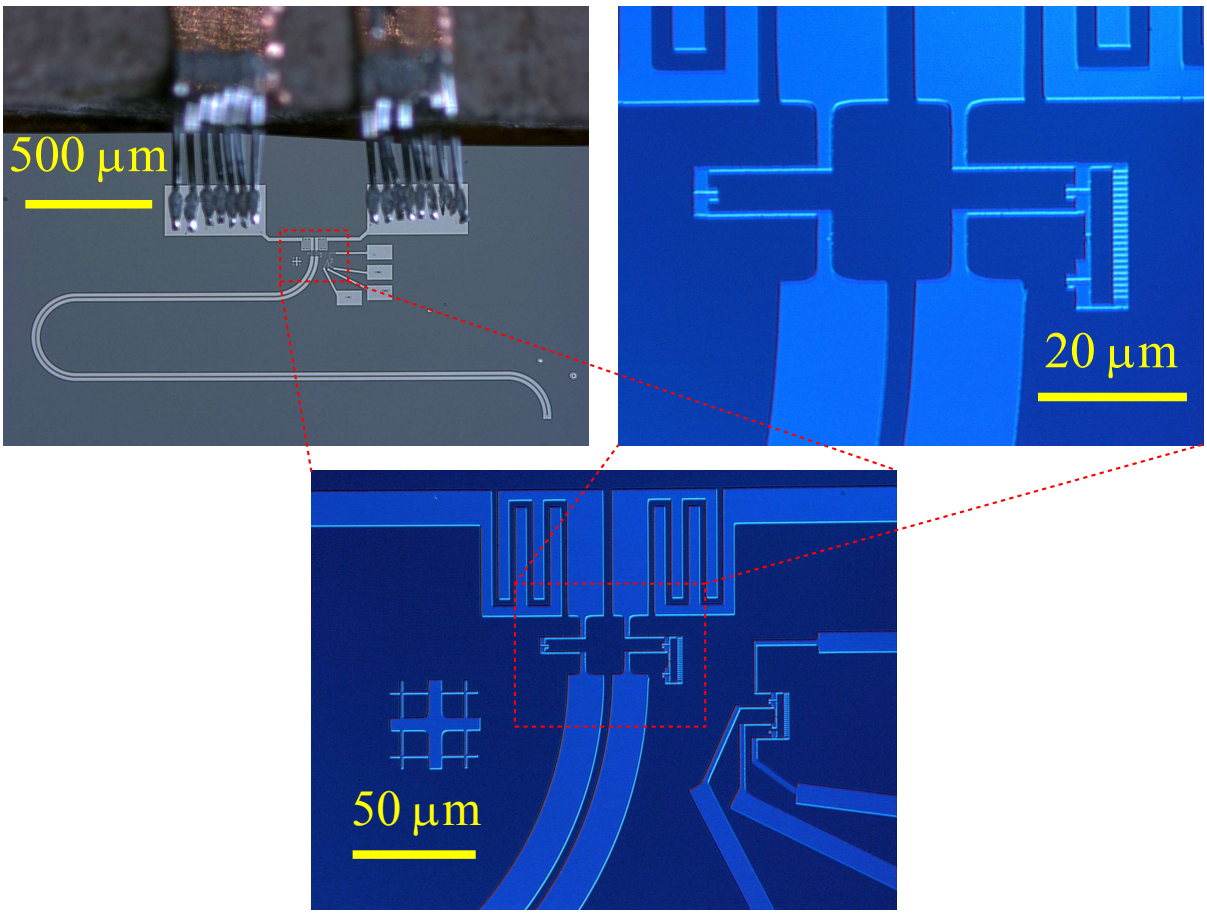

Figure 4.2: Optical images of inductively coupled sample (sample 5).

explained in Section 4.3.

Optical images of the inductively coupled sample are shown in Figure 4.2. Like the capacitively coupled samples, the readout resonator consists of a 3.5 mm long CPW quarter wavelength resonator. The CPW conductors have the same dimensions, however the substrate is 250 μm thick silicon, versus 300 μm (sample 1) or 500 μm (samples 2–4). The open end of the resonator is again coupled capacitively to the wirebonding pads. Near the open end of the resonator, the transmission line is interrupted with a coupling junction on each conductor. On one conductor, the coupling junction is shared with the qubit loop, while the opposite conductor has a bare junction to keep the transmission line symmetric. The qubit loop has a second

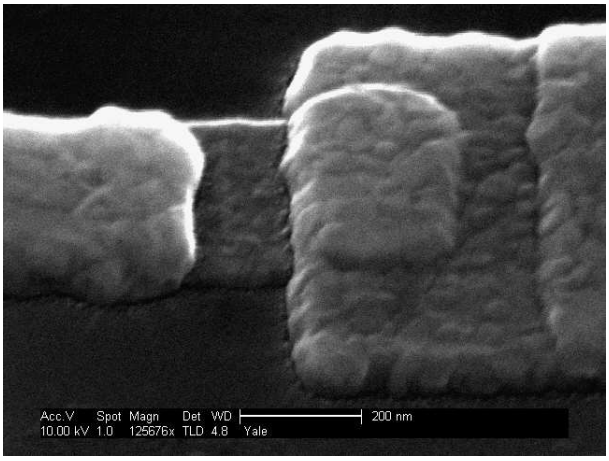

(a) "Weak" junction

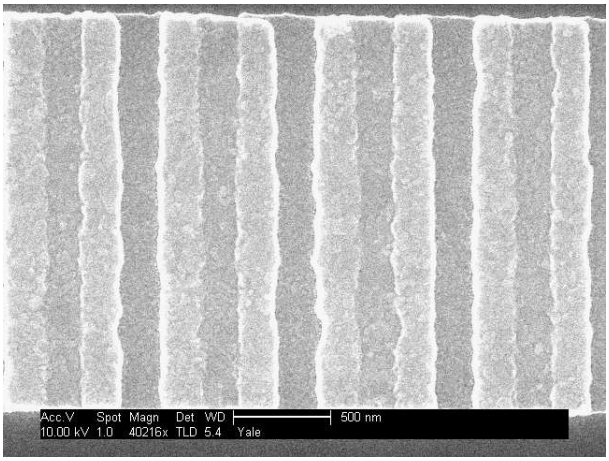

(b) Array

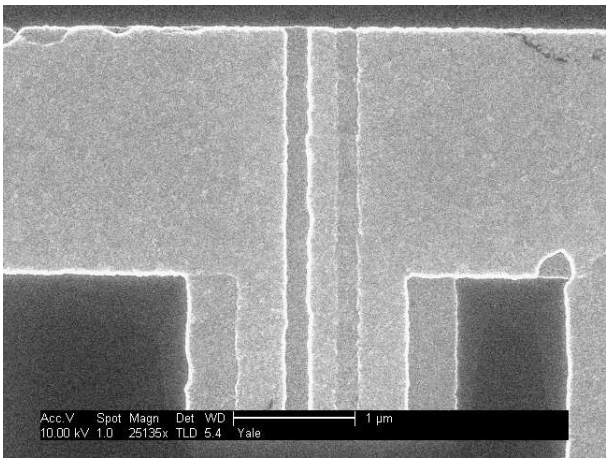

(c) Coupling junction (for inductively coupled sample)

Figure 4.3: SEM images of typical junctions.

large junction (same size as the coupling junction), which serves no specific purpose other than to keep the qubit loop symmetric.

All samples have test junctions near the qubit, which connect to pads for probe station measurements of their resistance. These test junctions are nominally identical to those in the qubit, and serve as a test for correct oxidation parameters and to monitor aging. SEM images of a typical junctions used in the fluxonium samples are displayed in Figure 4.3. Nominal dimensions for the small junctions are 300 nm $\times$ 200 nm, for the array junctions are 2 μm $\times$ 200 nm, and for the coupling junctions are 3.3 μm $\times$ 200 nm.

4.1.1 Dolan Bridge Arrays

Josephson junction arrays may be fabricated with the Dolan bridge technique [44], using a series of bridges. For an array with N bridges, $2N-1$ junctions will be formed. Junctions will occur underneath the bridges, as well as in-between bridges. It is advantageous for the evaporation angles and evaporation thicknesses to be chosen correctly such that the size of the "underneath" and "in-between" junctions match; mismatched sizes will mean the small junctions limit the critical current and phase-slip rate, while the large junctions do not contribute to the total inductance as much as the smaller junctions.

The junctions should be fabricated as close to one another as possible, to maximize the inductance per unit length, and minimize parasitic capacitance to ground. Junction spacing is limited by how narrow in width and thin in thickness the bridges can be fabricated without collapsing.

The evaporation process is diagrammed in Figure 4.4. The first evaporation is at angle θ_1, with an evaporated thickness of t_1 (this is the thickness of the film that would be deposited on a surface perpendicular to the beam). Similarly, the

second evaporation is at an angle θ_2 (measured in the opposite direction from θ_1) with an evaporated thickness t_2. Given the bridge dimensions and evaporation angles and thicknesses, the junction dimensions may be determined trigonometrically. By including corrections from accumulation of aluminum on the top and side of the bridges from the first evaporation, junction dimensions may be accurately determined (to within 5%).

Prior to deposition of aluminum on the first sample of a wafer, the thickness of the develop resist should be measured in the profilometer. At this point the total thickness of the resist is accurately known ($d + b$), and an educated guess may be made on the remaining bridge dimensions. Evaporation angles and thicknesses should be chosen such that the "underneath" and "in-between" junctions match using the estimated bridge values. The resultant array dimensions may then be measured under an SEM to more accurately determine the bridge dimensions. A single iteration of evaporation tests is generally all it takes to determine the parameters for an array with equal sized junctions using this method. For the devices fabricated in this thesis work, symmetric evaporation angles were used between 16° and 17.5°. Evaporation thicknesses of $t_1' = 20$ nm and $t_2' = 50$ nm were deposited on the substrate. An SEM image of a typical array fabricated with the Dolan bridge technique is shown in Figure 4.3(b). The nominal dimensions of the junctions are 2 μm × 200 nm, with connecting wires of the same size.

The following trigonometric expressions detail the array dimensions shown in Figure 4.4, given the first and second evaporation angles and thicknesses ($\theta_1,\ \theta_2,\ t_1,\ t_2$), and bridge dimensions ($w,\ h,\ b,\ d$).

Layer 1 thickness:

$$t_1' = t_1 \cos\theta_1 = t_1 \frac{s_1}{l_1} \tag{4.1}$$

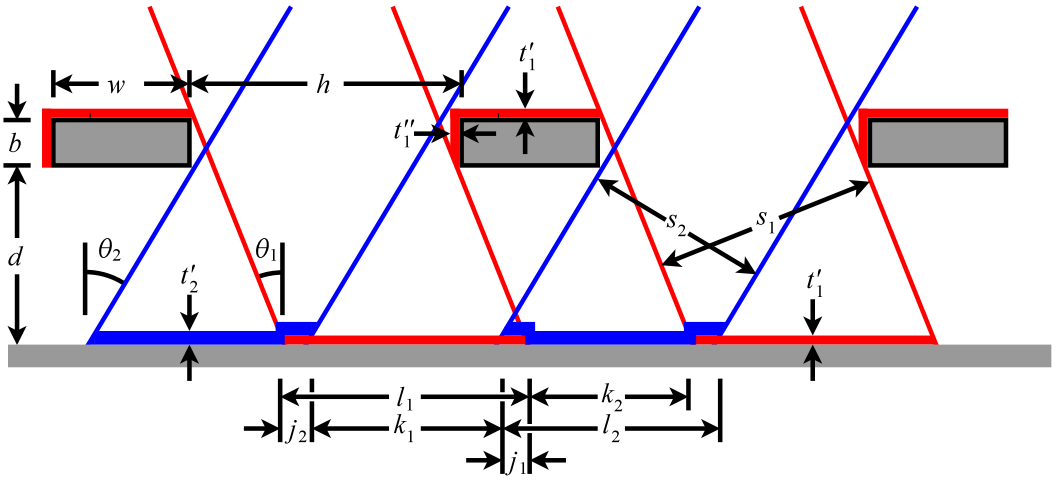

Figure 4.4: Dimensions of a double angle evaporation process of a Dolan bridge array. Red represents the first evaporation layer, including accumulation of metal on the top and sides of the bridges, while blue represents the second layer.

Thickness of bridge side accumulation due to evaporation of layer 1:

$$t_1'' = t_1 \sin\theta_1 \tag{4.2}$$

Layer 2 thickness:

$$t_2' = t_2 \cos\theta_2 = t_2 \frac{s_2}{l_2} \tag{4.3}$$

Width of layer 1 deposits:

$$l_1 = h - b\tan\theta_1 \tag{4.4}$$

Layer 1 beam width:

$$s_1 = l_1 \cos\theta_1 = h\cos\theta_1 - b\sin\theta_1 \tag{4.5}$$

Width of layer 2 deposits:

$$l_2 = h - t_1'' - (b + t_1')\tan\theta_2 \tag{4.6}$$

Layer 2 beam width:

$$s_2 = l_2 \cos\theta_2 = (h - t_1'') \cos\theta_2 - (b + t_1') \sin\theta_2 \tag{4.7}$$

Width of junctions under bridges:

$$j_1 = d \tan\theta_1 + (d - t_1') \tan\theta_2 - w \tag{4.8}$$

Width of junctions in-between bridges:

$$j_2 = h - t_1'' - (d + b)(\tan\theta_1 - \tan\theta_2) \tag{4.9}$$

Width of single layer between junctions, layer 1:

$$k_1 = l_1 - j_1 - j_2 = w + t_1'' + (b + t_1') \tan\theta_2 \tag{4.10}$$

Width of single layer between junctions, layer 2:

$$k_2 = l_2 - j_1 - j_2 = w + b \tan\theta_1 \tag{4.11}$$

4.2 Array Resonator Fabrication

The array resonators used to test the superinductance arrays were fabricated on a sapphire substrate with a silver backing. It was decided to switch to sapphire over silicon due to its lower loss tangent [77]. Additionally, the sapphire substrate allowed for more rigorous cleaning with the addition of oxygen plasma cleaning before spinning resist, after development, and before aluminum deposition within the evaporator. The wafer was spun with dual layers of e-beam resist, and written in a 100 kV

Vistec 5000+ electron beam pattern generator. The wafer was developed, aluminum was deposited using double angle evaporation, and after resist lift-off the wafer was diced. The device fabrication recipes are detailed in Section B.2. Device images are shown in Figure 1.33 and Figure 1.35.

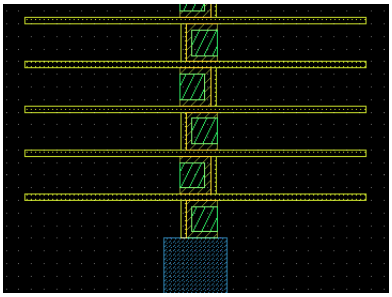

Figure 4.5: CAD image of an array using the bridge-free technique. The main dose is shown in yellow (and blue, for the large wire connecting to one end of the array), with the wire undercuts shown in green. Aluminum is deposited at angles from the left and right of the image. When the undercut box is to the right, the right angled deposition will stick to the substrate, while the left angled deposition will stick to the wall of the resist and subsequently be removed during lift-off. By alternating the undercut boxes to the left and right between junctions, the top and bottom layers are alternately connected between junctions, forming a series array.

The junctions were fabricated using a bridge-free technique which utilizes a selective undercut and double angle evaporation to cut a single layer of the wires that connect the junctions [45, 46]. This method allows for arbitrary shape junctions, and additionally benefits from the thin connecting wires connecting junctions when an array is formed, reducing the parasitic capacitance to ground. Along with the thin connecting wires, by changing the aspect ratio of the junctions to longer and skinnier junctions (near 1:30 aspect ratios), the parasitic capacitance of the arrays may be reduced by 60% using the bridge-free technique according to simulations. An image of the CAD for an array is shown in Figure 4.5. The array junctions are 5 μm $\times$ 140 nm with 500 nm $\times$ 100 nm connecting wires.

4.3 Sample Holder

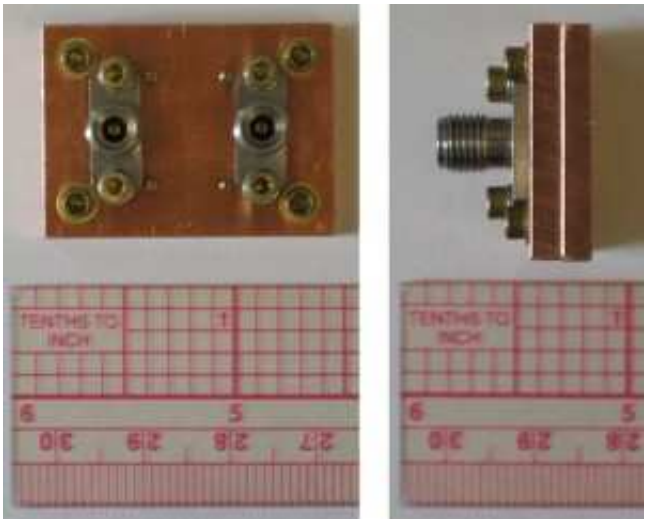

Figure 4.6: Overall view of a 2-port sample holder.

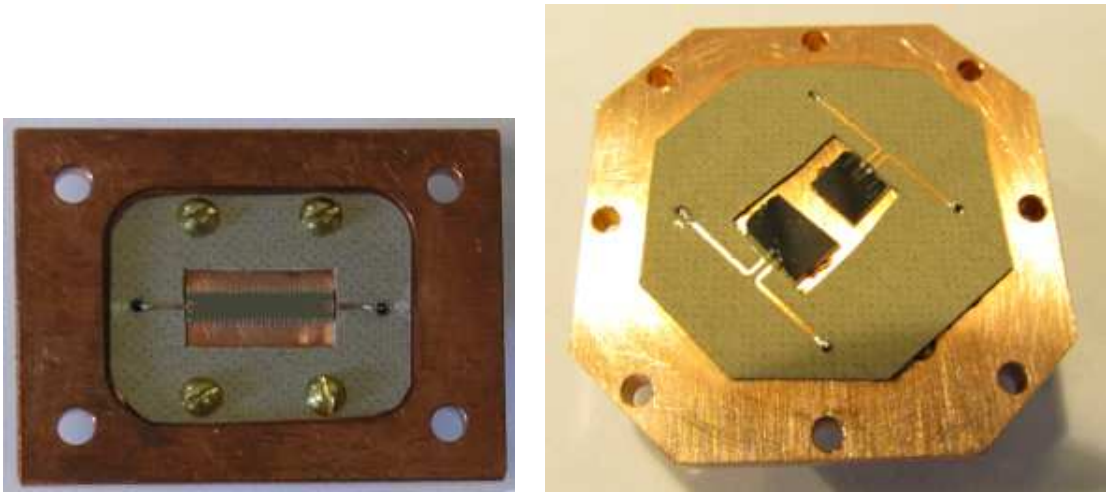

Figure 4.7: Chips mounted in 2 and 4-port versions of the sample holder. The chip in the 2-port holder has a CPW geometry, and the ground of the chip is directly wirebonded to the base of the sample holder. The 4-port holder is shown with two samples that are each differentially driven with two ports.

An important element in any mesoscopic electronics experiment is the sample holder, which provides protective housing (both physical and electromagnetic), ther-

malization and electrical connection to the sample. The sample holder used for fluxonium experiments utilized a perpendicular transition between the coaxial connector outside the box and microstrip line which is wirebonded to the sample. While other perpendicular coaxial to microstrip transitions exist [78, 79, 80], this sample holder has a simpler construction. The holder is straightforward to machine, and only requires single-sided PCB's for the microstrip traces that may be fabricated in-house (the base of the sample holder acts as the ground plane for the microstrip). An image of a 2-port version of the sample holder is shown in Figure 4.6, and samples mounted in 2 and 4-port versions are shown in Figure 4.7.

4.3.1 Coaxial to Microstrip Transition

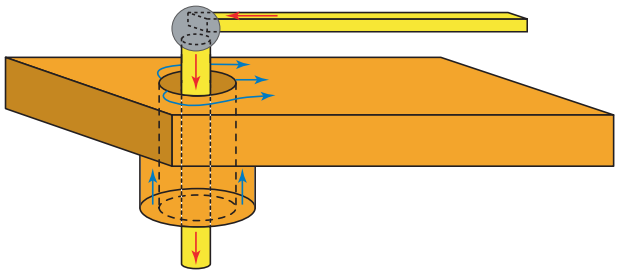

Figure 4.8: An illustration of the coaxial to microstrip transition. Blue arrows show how the currents in the grounding conductor are routed from the coaxial shell to the ground plane of the microstrip, while red arrows show the current in the center conductor and microstrip.

One of the main advantages of the sample holder's design is its perpendicular transition between coaxial and microstrip geometries, which allows for compact yet convenient configuration of the coaxial connections. An edge-launch geometry becomes cumbersome to install in a measurement setup as the number of connectors increases. In order to achieve high frequency performance of the transition, the coaxial cable is shrunk down before the transition. This reduction in size minimizes the

path length differences in the grounding shell as it transitions into a plane, as illustrated in Figure 4.8. The extra length the signal must travel during the transition versus the ground path results in a parasitic inductance which will ultimately limit the high frequency performance and produce a low-pass behavior.

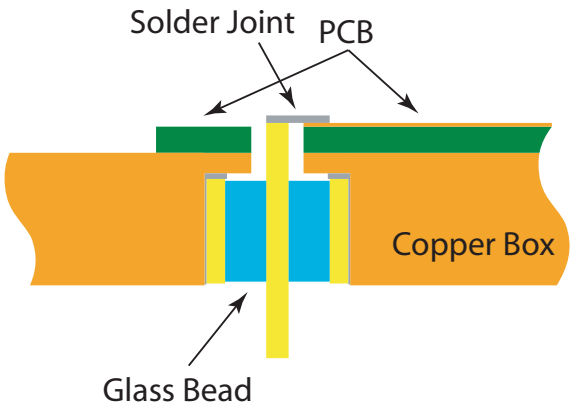

Figure 4.9: A cross section of the physical implementation of the coaxial to microstrip transition. An Anritsu K connector flange launcher (not shown) sits on the bottom of the coaxial bead.

The transition is implemented using a coaxial glass bead (Anritsu K100B) which is soldered in a pocket milled into the OFHC copper sample holder, with a small hole allowing the pin to pass through to the opposite side where the PCB sits (illustrated in Figure 4.9). Anritsu produces a step drill (Anritsu 01-104) that allows the pocket and holes for the bead to be drilled after a pilot hole is drilled, but at the cost of convenience cheaper conventional machine tools may be used to produce the same results. The required dimensions for the bead pocket and holes are detailed in the datasheet for the Anritsu 01-104 step drill. Anritsu K flange launch connectors sit on top of the bead (K103F for female, K103M for male), which are SMA compatible. The male and female connectors are conveniently interchangeable, even after the sample holder is closed and has a sample mounted.

The PCB used for microstrip traces is Arlon AR1000L01555, a 15 mil thick

glass and PTFE laminate with a relative dielectric constant of 9.6, requiring 14 mil microstrip trace widths for 50 Ω. Similar materials may be used, adjusting the microstrip trace width as necessary to compensate for changes in dielectric constant. The PCB is glued down to the sample holder base with Lake Shore VGE-7031 varnish. Because the base of the sample holder acts as the microstrip ground, it is critical that the PCB lie flat. The sample holder base must be free from burrs from machining, and the PCB should be pressed firmly and evenly against the holder while the varnish cures.

The joints between center pins of the coaxial beads and microstrip traces is made with a low melting point (158 °F) alloy known as Wood's metal, consisting of bismuth, lead, tin and cadmium. The reason for using this alloy over conventional tin/lead solder is the low surface tension of Wood's metal, allowing it to bridge the gap between the bead pin and microstrip trace in a thin layer. Tin/lead solder will tend to ball up on the bead pin and microstrip trace, making it difficult to solder the two parts together. However, it does help to pre-tin with tin/lead solder before using Wood's metal.

Samples are mounted to the holder by either gluing down with Lake Shore VGE-7031 varnish, or silver paste for silver backed samples. The sample may then be wirebonded to microstrip traces, or to the base of the sample holder for grounding. Samples may be carefully removed to allow reuse of the holder without requiring replacement of the PCB.

4.3.2 Microwave Characterization

The performance of the microwave transitions is tested by measuring the S parameters for a through connection, as shown in Figure 4.10. The S parameters are shown in Figure 4.11 for three different trials, where between trials the solder joint between

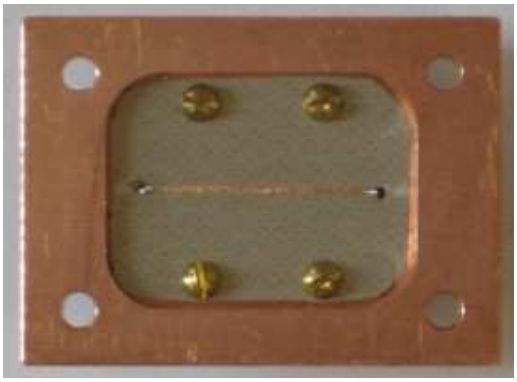

Figure 4.10: Sample holder with a through microstrip for characterization of return losses.

the bead pin and microstrip trace was redone. The general low-pass trend is unmodified by variations in the solder joints, however an excessive amount of solder in the joint will significantly degrade performance. Therefore it is important to use as little solder as possible, while still making a mechanically secure joint (the sample holder may be tapped on a table several times and its continuity tested to verify mechanical strength of the bond).

When a cap is applied to the 2-port sample holder, resonances of the cavity formed will result, as shown in Figure 4.12. To eliminate these resonances a small amount of Eccosorb® may be inserted in the box, such as shown in Figure 4.13. Eccosorb® GDS SS-6M was used for the tests shown here. Alternatively, the dimensions of the box may be adjusted such that any resonances are pushed away from frequencies that would be problematic. The cavity modes were not apparent in any experiments using this type of sample holder during this thesis work (Eccosorb® was not used in any experiments).

Isolation between the ports in the 2-port sample holder was tested by putting a 10 mm break in the through line shown in Figure 4.10, with results shown in Figure 4.14. The ports are isolated by better than 60 dB up to 8 GHz, and better

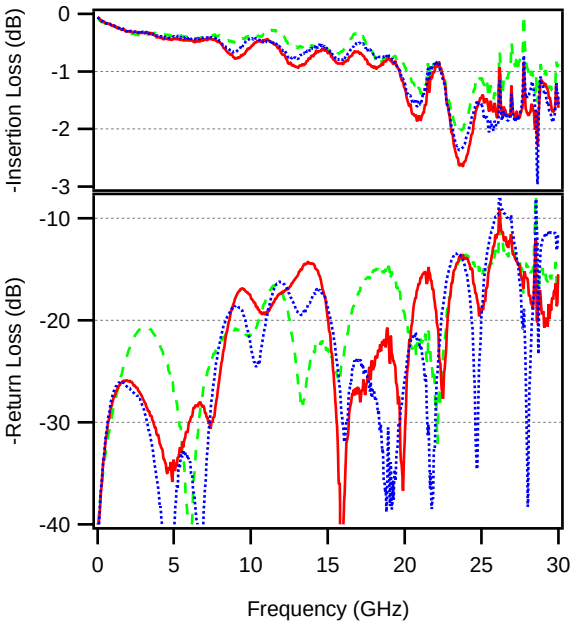

Figure 4.11: Insertion and return loss for a microstrip through between ports for three different trials, each trial corresponding to redoing solder joints to the microstrip. The top plot is insertion loss, while the lower is return loss. Similar line styles in the two plots correspond to the same trial.

than 40 dB up to 10 GHz, and the addition of Eccosorb® to the cavity improves isolation near cavity modes. Reducing the size of the cavity to push the modes up in frequency would improve isolation without the need for Eccosorb®.

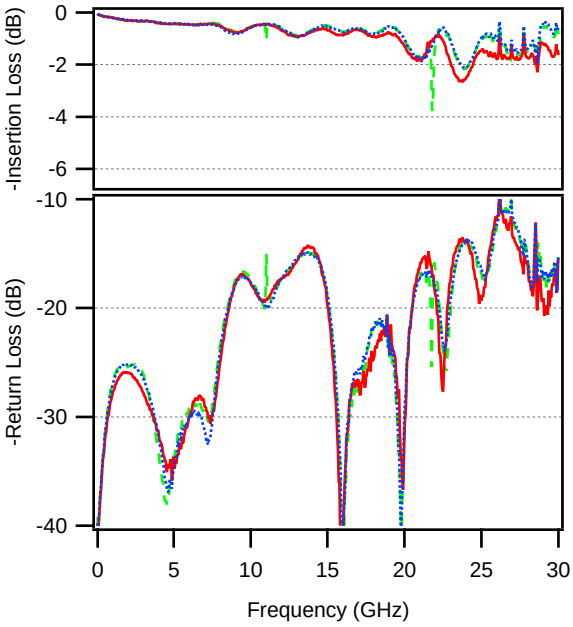

Figure 4.12: Insertion and return losses with no cap (red solid, same as solid data in Figure 4.11), with a cap (green dashed, cavity resonances can be seen), and with cap and Eccosorb® (blue dotted, cavity resonances are reduced).

Figure 4.13: Sample holder cap with Eccosorb® GDS SS-6M.

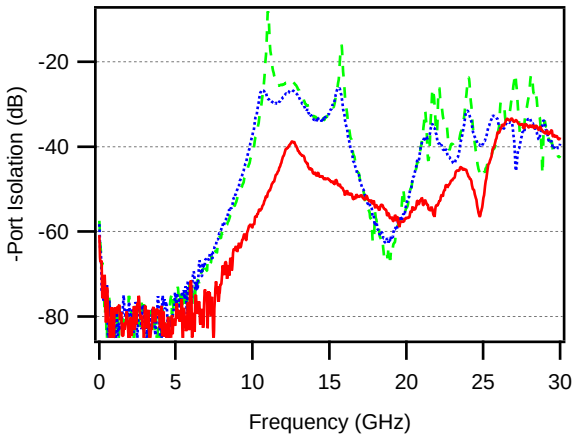

Figure 4.14: Port isolation with no cap (red solid), capped (green dashed), and capped with Eccosorb® (blue dotted). The cap provides a cavity for microwaves to propagate, but Eccosorb® reduces the transmission.

4.4 Dilution Refrigerator Setup

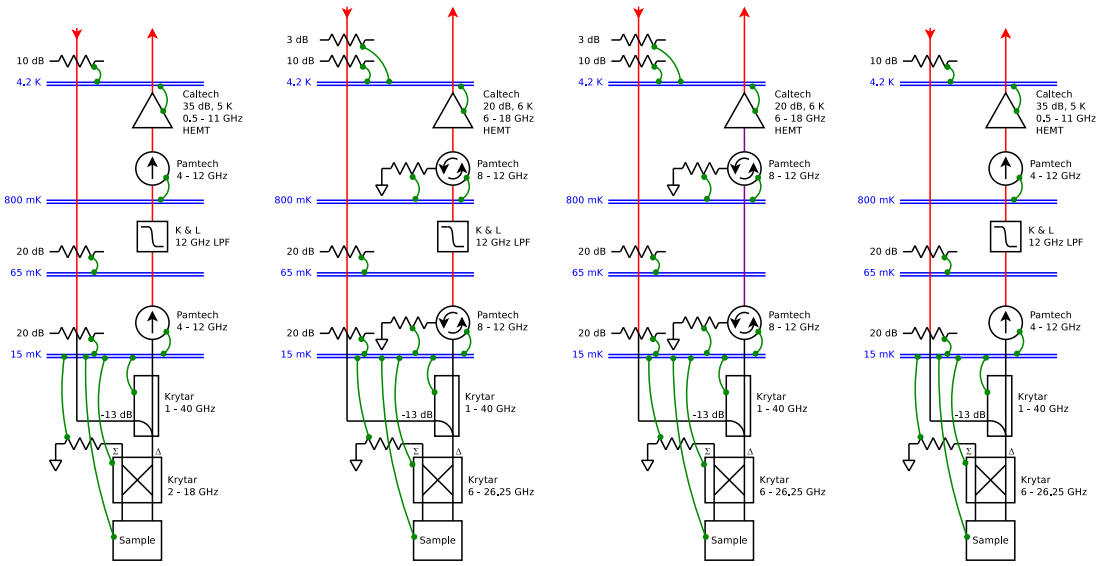

(a) Samples 1 and 2 (b) Sample 3 (c) Sample 4 (d) Sample 5

Figure 4.15: Fridge wiring diagrams for the fluxonium samples measured. Red lines are stainless steel semi-rigid cables (inner and outer conductors), purple are superconducting niobium titanium, and black are copper. Green lines terminated with dots represent thermalization anchors between components and refrigerator stages. The thermal anchor for attenuators drawn above the 4.2 K stage lines is provided by their immersion in the liquid helium bath.

Wiring diagrams for the measurement setup of the five fluxonium samples is shown in Figure 4.15. The refrigerator was equipped with two sets of measurement lines, which may undertake slight modifications between runs. Samples 1, 2 and 5 used one set of lines, while samples 3 and 4 used the other set of lines.

The sample holder was mounted at the mixing chamber stage of a Cryoconcept dilution refrigerator, rated at 200 μW @ 100 mK. The base temperature was 15 ± 1 mK. The sample holder was thermalized to the base stage with strips of OFHC copper, except for sample 1, which was thermalized with copper braid. The microwave lines between stages were 85 mil semi-rigid cable with stainless steel inner and outer conductors, with the exception of sample 4 which used superconducting

niobium titanium semi-rigid cables between the directional coupler and HEMT amplifier. The superconducting cable was later replaced with stainless steel, as the crimp SMA connectors used on the superconducting cables were suspected of having poor connection at low temperatures. In addition, the setup for sample 4 did not include the 12 GHz low pass filter between circulators on the output line in order to minimize losses between the qubit and HEMT amplifier. Microwave interconnects at the mixing chamber stage were 85 mil copper semi-rigid cable.

The directional couplers, isolators, circulators and HEMT amplifiers were thermalized by mounting to OFHC plates. Attenuators and terminators were thermalized by wrapping with copper braid which was then clamped on with a bracket.

After all components are mounted in the refrigerator, gaps and holes in the stage plates are covered with copper tape to reduce radiation traveling down to the samples. Aside from the IVC can which is immersed in liquid helium, the only stage with a shield was the mixing chamber stage. For magnetic shielding the samples were placed inside a Cryoperm can.

The refrigerator wiring for the experiments on array resonators are diagrammed in Figure 4.16. The input and output lines had the addition of copper powder filters, described in Subsection 4.6.2. The magnetic shields were also improved, and consist of aluminum-Cryoperm-aluminum cans with Cryoperm caps.

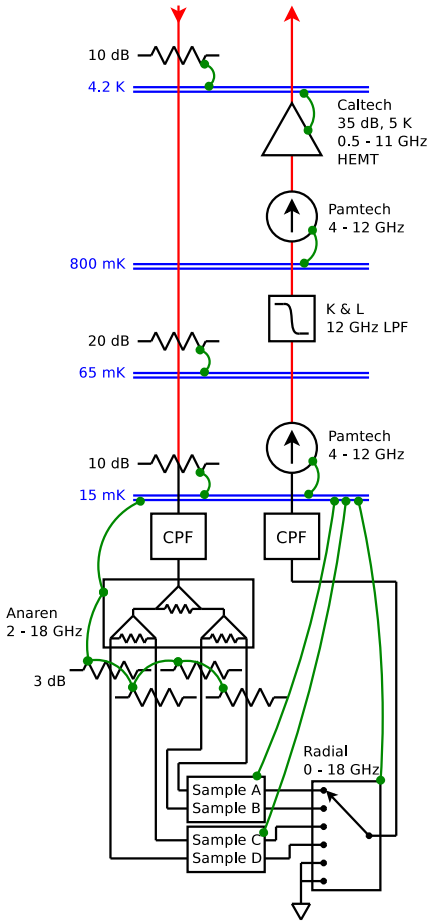

Figure 4.16: Fridge wiring diagrams for experiments on arrays.

4.5 Room Temperature Electronics

The wiring diagram for the room temperature electronics is shown in Figure 4.17. The timing of all pulses as well as data acquisition are controlled by a single AWG. Several microwave generators for qubit manipulation and readout are combined with a Wilkinson hybrid, then sent into the refrigerator setup. Only the readout tone needs to be recovered from the refrigerator. The readout tone which is output from the refrigerator is amplified and heterodyned down to 50 MHz before being sampled by a computer with an Acqiris AP240 data acquisition card. As a phase reference, a duplicate copy of the readout pulse is mixed down to 50 MHz and sampled in a

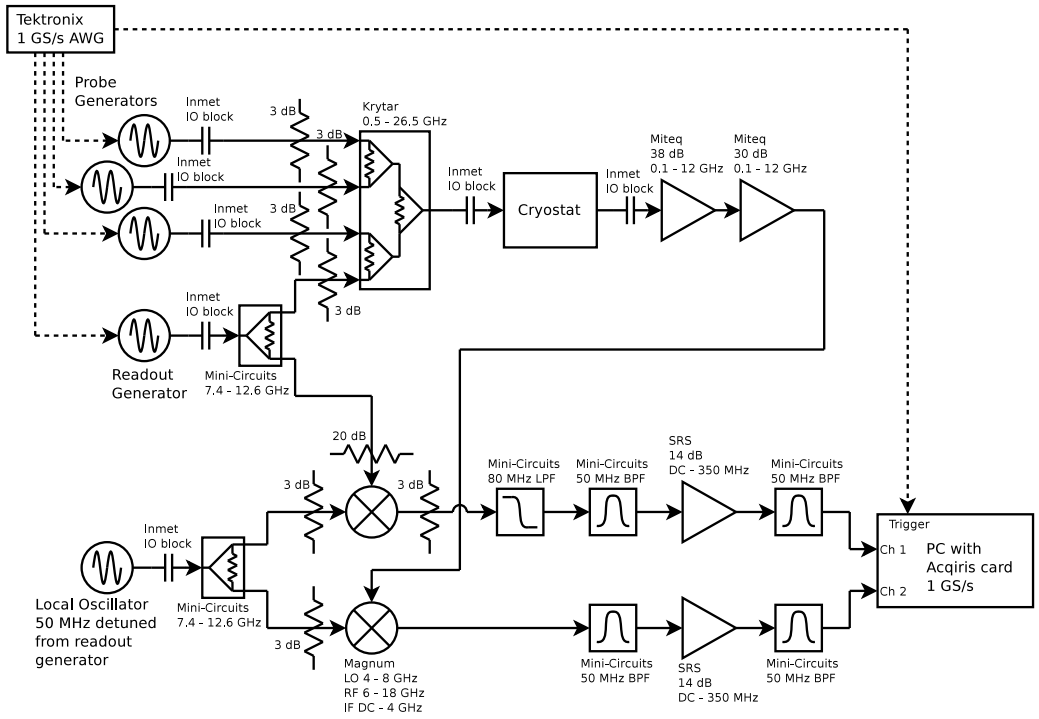

Figure 4.17: Wiring diagram of the room temperature electronics for microwave excitation and readout of fluxonium samples. All active components requiring a time base are synchronized to a 10 MHz rubidium standard. Additionally, the PC can communicate to the microwave generators and AWG through GPIB.

separate channel in the Acqiris card. This measurement setup has the advantage that drifts in the phase of the microwave generators are subtracted out, and do not affect the measurement. However, changes in phase between the two heterodyne paths will not be removed (for example, the boiling off of liquid helium inside the refrigerator may change the path length of the cables).

All experiments are repeated tens of thousands of times to build up a large enough qubit "population", allowing for measurements with a high enough SNR to overcome noise in the experimental setup. As the heterodyned readout and reference signals are acquired by the Acqiris card, the signals from repeated experiments are averaged together (except for single shot experiments). The initial portion of the readout pulse coming from the readout resonator is used to infer the qubit state (typically the first

200 ns). The phase from the averaged readout and reference signal is subtracted to remove phase drifts in the RF generators between experiments. For convenience, phase is generally used to monitor the qubit state. Measuring a quadrature amplitude instead of phase requires rotating the reference axes such that the difference between the signal returned when the qubit is in the ground state versus the excited state lie on one quadrature. When phase is monitored, there is a trivial phase offset which may be ignored, but no need to rotate reference axes. However, for large dispersive shifts the non-linear mapping to phase will distort the apparent response of averaged experiments (for example, a rabi oscillation will look compressed on the ends when observed in phase), so quadrature amplitudes should be used instead.

In some experiments, it is important that different measurements have the same phase reference, or are measured as simultaneously as possible. For example, when measuring T_1 and T_2 times, it is desirable to measure these in as short a time span as possible. If the T_1 and T_2 are measured at separate times, it is possible at certain flux biases in some samples that one could obtain $T_2 > 2T_1$ due to fluctuations in these times. Additionally, one might want to overlay the relaxation and Ramsey curves, and an undesirable phase offset may exist between the two. To resolve these problems, an interlaced pulse sequence may be utilized, where (for example) odd pulse patterns correspond to the relaxation experiment, and even pulse patterns correspond to the Ramsey experiment. In this way, both experiments are effectively performed simultaneously. This method was utilized in acquiring the data presented in Subsection 1.3.1.

4.6 Filters for Microwave Lines

A challenge in quantum electronics experiments is to effectively filter away radiation from room temperature radiation. In addition to thermal shields surrounding the sample, the input and output RF lines must be protected as well. While anchoring attenuators to the various stages in a refrigerator on the input line will reduce Johnson noise upto several tens of GHz, it is not clear they can perform in the hundreds of GHz to THz region (room temperature corresponds to 300 K $\times$ k_B/h = 6 THz). Additionally, noise coming down the output lines may not be blocked by the HEMT amplifier and circulators, and the HEMT itself may be a significant source of noise. To alleviate these concerns, filters that are highly attenuating from the hundreds of GHz to infrared must be installed before the sample on all lines. The filter does not need to have a sharp cutoff above the readout frequency or other frequencies of interest, conventional multi-section microwave filters can perform this role. Rather, these filters should pick up where conventional filters leave off (mulit-section low-pass filters by K & L have a sharp cutoff that extends to 40 GHz, but it is not known what happens beyond).

In the case of qubit experiments, the filter must be well matched at readout frequencies (7 - 9 GHz) to minimize loss of signal coming from the device, and not too highly attenuating at transition frequencies which will be sent to the qubit to ensure the desired qubit operations can be performed without requiring more power than the room temperature electronics can deliver, or excessively heating the refrigerator.

A well-matched filter will minimize the reflection of microwaves coming into the filter; any incoming signal which is not absorbed by the filter should be transmitted through, as reflecting the signal unnecessarily degrades the SNR of the readout. The

voltage reflection coefficient from a load is given by

$$\Gamma = \frac{Z_L - Z_0}{Z_L + Z_0}, \tag{4.12}$$

where Z_0 is the characteristic impedance of the source transmission line, and Z_L is the load impedance, which may be complex. In our case, $Z_0 = 50\ \Omega$, and Z_L represents the impedance of our filter with a 50 Ω termination on the opposite port. The matching of a load is frequently expressed as a return loss, given by

$$\mathrm{RL} = -20 \log |\Gamma| \text{ dB}. \tag{4.13}$$

Note that this is simply the magnitude of the single-port S-parameter expressed in dB, but with a sign difference. A device with a high return loss is well matched to the characteristic impedance of the source, and therefore reflects little of the incoming signal. A 10 dB return loss corresponds to 10% of the incoming signal bouncing back, and a 20 dB return loss corresponds to 1%. The return loss for a 50 Ω source as a function of (real) load impedance is plotted in Figure 4.18.

To meet the requirements of a filter that is both matched at readout frequencies and high loss in the hundreds of GHz to infrared, a copper powder filter was developed while others in the lab simultaneously developed a filter using Eccosorb®. Both filters are discussed below, however both filters still require "before and after" experiments to verify or dismiss their effectiveness (thus far both filters have been implemented in several experiments, but not before first performing the identical experiment without the filters).

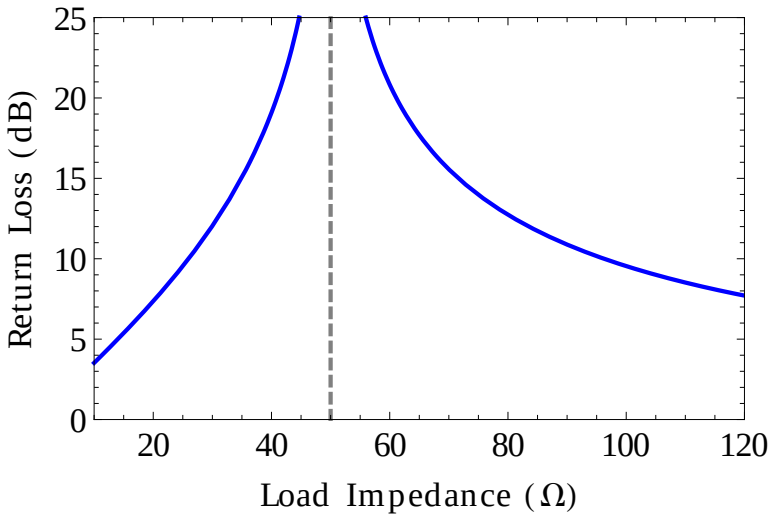

Figure 4.18: Return loss into a real load from a source with a characteristic impedance of 50 Ω. When the load is impedance matched at 50 Ω the return loss becomes infinite.

4.6.1 Eccosorb® Filters for Microwave Lines

Eccosorb® is a magnetically loaded microwave absorbing material manufactured by Emerson & Cuming. It comes in a variety of forms such as silicone sheets, foams, and machinable stock, but of particular interest is the Eccosorb® CR, a two-part epoxy that may fill and seal arbitrary shaped volumes. While Emerson & Cuming only provide absorption data up to a few tens of GHz, they expect its attenuation should extend fully into the optical region. Matched filters using Eccosorb® have been reported [81], and embedding the sample holder containing a capacitively shunted flux qubit in Eccosorb® CR-124 was shown to improve the relaxation time and thermal population of the qubit [82].

The filter described here is similar to those reported in [81], but aims for reduced loss and matching up to 10 GHz, and uses the least absorptive Eccosorb® epoxy, CR-110. The filter consists of an OFHC box with knurled SMA connectors pressed in to opposite sides. In order to hermetically seal the SMA connectors the joint is

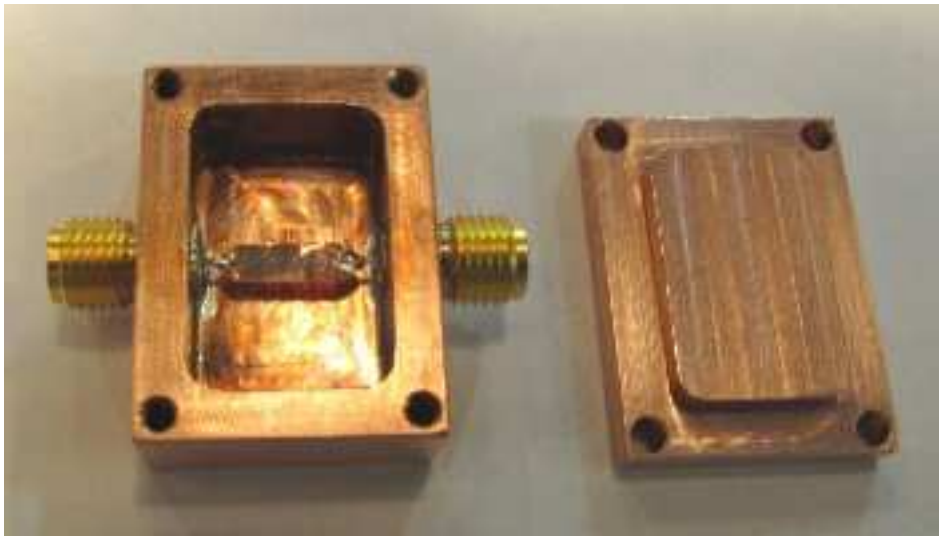

Figure 4.19: Eccosorb® filter before filling the interior cavity with Eccosorb® CR epoxy.

sweated with solder (skipping this step will result in the Eccosorb® epoxy leaking out before it has cured). The center pins from the SMA connectors are soldered to a strip of sheet copper, as shown in Figure 4.19, the dimensions of which are chosen to provide 50 Ω impedance based on RF simulations. The box is filled with Eccosorb® epoxy, and the lid is placed on top before the epoxy cures. This results in a stripline transmission line with a lossy Eccosorb® dielectric.

The filter has a steady roll-off, shown in Figure 4.20. This particular design has a resonance at 4.5 GHz when measured at room temperature, but it becomes less significant when cold. The matching of this design can likely be improved upon. Using a coaxial geometry would simplify construction, and should facilitate in producing a filter with improved matching by optimizing the conductor diameters.

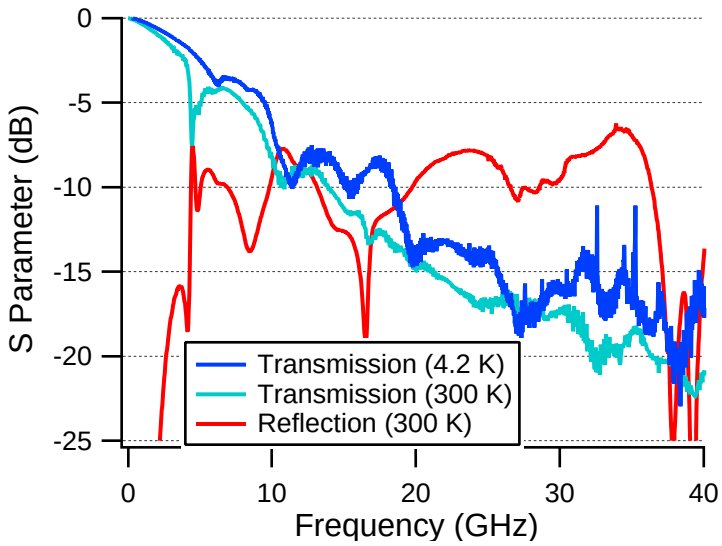

Figure 4.20: Transmission and reflection response for an Eccosorb® filter. Transmission data was taken at room temperature and at 4.2 K dunked in liquid helium. At room temperature the network analyzer used SOLT calibration, and for helium dunk testing a through calibration was made by dunking the cables before inserting the filter. Because the setup could not be SOLT calibrated when cold, reflection data was only done at room temperature. There is a cavity resonance at 4.5 GHz when warm, which can be seen as a dip in transmission and peak in reflection. This resonance moves up to 6.1 GHz when cold, and becomes less pronounced.

4.6.2 Copper Powder Filters for Microwave Lines

The use of metal powders as a highly absorptive material in filters has been well established [83, 84, 85], however at present there are only a few reports of using impedance matched metal powder filters for use at microwave frequencies [86, 87, 88]. The copper powder filter presented here is simpler to construct than that reported in [86] (the materials used are more common, and no machining is required other than drilling), and is better matched than that in [87, 88]. Additionally, the matching is better than the Eccosorb® filter presented in Subsection 4.6.1.

The filter, shown in Figure 4.21, is essentially a segment of lossy coaxial cable. It consists of a 7.9 mm inner diameter copper pipe, acting as the outer conductor, and 0.5 mm copper wire for the center conductor. The wire is covered with two layers

Figure 4.21: Copper powder filter with SMA connections. The center section acts as a lossy coaxial cable.

of polyolefin heat shrink tubing (the thickness of this layer is 0.9 mm, adjusted to impedance match the filter), and the remaining volume is filled with -100 mesh copper powder ($\leq$ 150 μm diameter). The inductance per unit length for a coaxial geometry is given by

$$L_l = \frac{\mu_0}{2\pi} \ln\left(\frac{r_2}{r_1}\right), \tag{4.14}$$

where μ_0 is the permittivity of free space, and r_1 and r_2 are the inner and outer conductor diameters, respectively. The capacitance per unit length is

$$C_l = \frac{2\pi\epsilon}{\ln\left(\frac{r_2}{r_1}\right)}, \tag{4.15}$$

where ϵ is the dielectric constant of the dielectric between the conductors. The characteristic impedance of the coaxial cable is

$$Z_1 = \sqrt{\frac{L_l}{C_l}} = \frac{1}{2\pi} \ln\left(\frac{r_2}{r_1}\right) \sqrt{\frac{\mu_0}{\epsilon}}. \tag{4.16}$$

The characteristic impedance of the filter transmission line will be designated with Z_1, as Z_0 will continue to represent the characteristic impedance of the 50 Ω lines in

the measurement setup. Assuming dielectric losses from the copper powder, modeled as the dielectric having real and imaginary parts $\epsilon = \epsilon' - j\epsilon''$, the attenuation of the filter will increase exponentially with frequency. The complex propagation constant is

$$\gamma = \sqrt{j\omega L_l \times j\omega C_l} = j\omega\sqrt{\mu_0 \epsilon}, \tag{4.17}$$

where the attenuation constant α is given by the real part of the propagation constant. The transmission coefficient through such a filter is given by

$$T = \frac{(1+\Gamma_1)(1-\Gamma_1)\mathrm{e}^{-\gamma l}}{1-\Gamma_1^2 \mathrm{e}^{-2\gamma l}}, \tag{4.18}$$

where $\Gamma_1 = (Z_1 - Z_0)(Z_1 + Z_0)$, and l is the length of the filter.

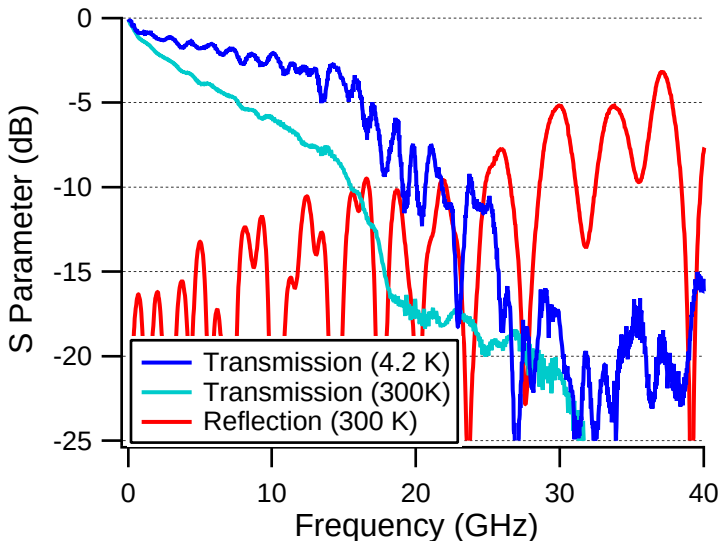

Figure 4.22: Transmission and reflection response for a copper powder filter. Transmission data was taken at room temperature and at 4.2 K dunked in liquid helium. At room temperature the network analyzer used SOLT calibration, and for helium dunk testing a through calibration was made by dunking the cables before inserting the filter. Because the setup could not be SOLT calibrated when cold, reflection data was only done at room temperature. At 4.2 K there is less than 3 dB of insertion loss up to 10 GHz. The return loss is better than 10 dB up to 16 GHz.

S-parameters for a filter with a 60 mm long center conductor are shown in Figure 4.22. The return loss is better than 10 dB up to 16 GHz (at room temperature). When dunked in liquid helium, the insertion loss is below 3 dB up to 10 GHz, meaning more than half the qubit signal will make it through the filter. These results were reproducible for 5 other filters constructed in the same way, and the filters were unaltered after several cooling cycles.

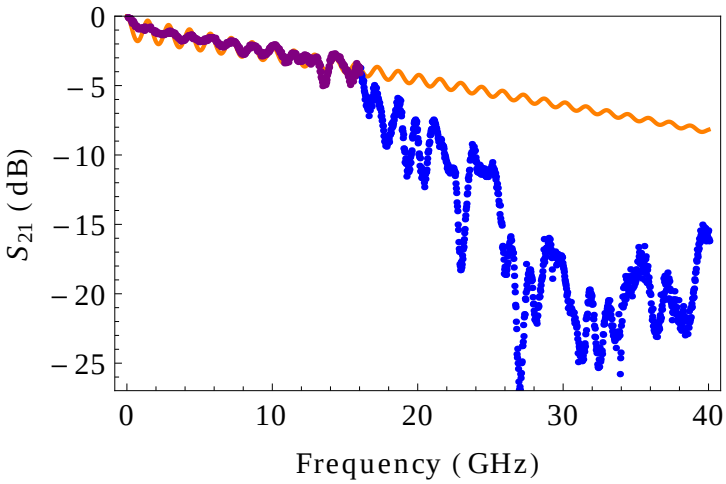

Figure 4.23: Theoretical transmission response (orange) for a 60 mm long filter filled with a dielectric of $\epsilon_r = 3.0 - 0.059j$. Overlaid in blue and purple is transmission data at 4.2 K. The purple section is the first 16 GHz of data to which a fit was applied to extract the real and imaginary parts of ϵ_r.

Up to 16 GHz the filter displays the expected exponential increase in attenuation with frequency. Beyond 16 GHz the insertion loss of the filter increases most likely due to degraded impedance matching, which may be the result of waveguide modes in the pipe. However, impedance matching at these higher frequencies is not important (it is only necessary that the readout frequency be well matched), and we expect the exponential increase in attenuation due to dielectric loss continues. The initial trend in attenuation can be described by the copper powder and polyolefin having an effective relative dielectric constant of $\epsilon_r = 3.0 - 0.059j$. Figure 4.23 displays

the theoretical behavior of a filter with such a dielectric, overlaid with the cold transmission data. This dielectric corresponds to the attenuation constant $\alpha = f \times 0.35$ Np/m/GHz, and for the 60 mm length of the filter results in a loss of 0.18 dB/GHz (the conversion between nepers and decibels is 1 Np = $10\log(e^2)$ dB $\simeq 8.69$ dB), translating to over 180 dB of loss above 1 THz. Filters with a similar frequency roll-off have been designed using bronze and carbon powder with a NbTi center conductor [88].

Construction

A piece of 18 AWG wire (measures 0.5 mm in diameter) used for the center conductor of the filter is cut and filed to length to square the ends. The magnet wire has a thin poly-thermaleze coating which is not required, but useful as a solder mask. ThermoSleeve HST116BK100 1/16" black polyolefin heat shrink tubing is shrunk over the wire, and the ends of the heat shrink tubing are cut flush to the wire. The ends of the wire are tinned, then butt-soldered to the center conductor of 85 mil semi-rigid cable. The center conductor of the cable is cut and filed square to 0.5 mm before soldering. To protect the joint from shorting through the copper powder, it is coated with Lake Shore VGE-7031 varnish before a second layer of heat shrink tubing is applied and trimmed to cover both joints, as shown in Figure 4.24.

A piece of 7.9 mm inner diameter copper pipe is cut 3 mm longer than the central wire, and the inside of the pipe is cleaned. Pieces of sheet copper are cut to disks matching the outer diameter of the pipe, and holes are drilled in the middle to allow the passage of the semi-rigid cable. A disk is soldered to one end of the pipe, and the semi-rigid cable is soldered into the disk such that the wire is centered within the pipe. The resultant solder joint is shown in Figure 4.25. At this point the pipe is filled and compacted with copper powder, as shown in Figure 4.26, and a second

(a) Solder joint covered with Lake Shore VGE-7031 varnish.

(b) Polyolefin heat shrink tubing covering solder joints and the entire length of wire.

Figure 4.24: Connection between the 85 mil semi-rigid cable center conductor and 0.5 mm copper wire. A first layer of polyolefin heat shrink tubing is applied to the 0.5 mm wire before soldering. The solder joint is then sealed with varnish before a second layer of heat shrink tubing covers the 0.5 mm wire and solder joints at both ends.

disk is soldered on to seal the filter. Standard SMA connectors may then be applied to the semi-rigid cable protruding from the filter.

Figure 4.25: Solder joint between the outer conductor of the 85 mil semi-rigid cable and shell of filter. A round piece of copper sheet with a hole drilled in the middle is soldered to the end of the copper pipe, then the coaxial cable is soldered to the copper sheet.

Figure 4.26: The inside of the filter is filled and compacted with copper powder. The outer edge of the copper pipe is pre-tinned to simplify sealing of the filter.

Chapter 5

Experimental Results

This chapter focuses on experiments with the fluxonium artificial atom which were used in the course of this thesis work. The most important experiments which verify proper functionality of the fluxonium sample, and are used to characterize the sample, are detailed in the first section. Other experimental techniques which have been performed and may be useful for future experiments are presented in the sections that follow.

5.1 Primary Experiments

5.1.1 Finding the Readout

The very first measurement when a sample is cooled down is to locate the resonant frequency of the readout resonator. Unless there is a severe problem in the measurement setup or sample, the readout resonator should be easy to find and clearly visible. The response near resonance frequency ν_R can be approximated as a single

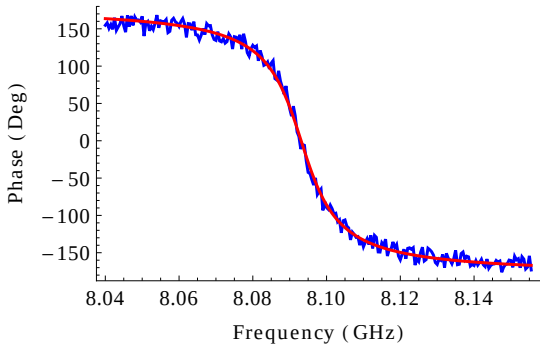

Figure 5.1: Readout resonance response for sample 2 with a least squares fit of Equation (5.2) in red.

mode resonance with the voltage reflection coefficient [89]

$$\Gamma = \frac{2j\left(\frac{\nu-\nu_R}{\nu_R}\right) - \frac{1}{Q_{\text{ext}}} + \frac{1}{Q_{\text{int}}}}{2j\left(\frac{\nu-\nu_R}{\nu_R}\right) + \frac{1}{Q_{\text{ext}}} + \frac{1}{Q_{\text{int}}}}. \tag{5.1}$$

The fluxonium samples have been designed to be strongly overcoupled ($Q_{\text{ext}} \ll Q_{\text{int}}$), and are measured in a reflection measurement. This allows for simplification of Equation (5.1) by dropping Q_{int} terms, and puts the resonator response entirely in the phase of the reflected signal:

$$\theta = \text{Arg}[\Gamma] = 2\arctan\left(-2Q_{\text{ext}}\frac{\nu-\nu_R}{\nu_R}\right). \tag{5.2}$$

The actual response from the measurement setup will have some arbitrary phase offset and electrical delay which will need to be subtracted out. A representative readout response is plotted in Figure 5.1.

5.1.2 Flux Modulation of Readout Resonator

While applying a CW readout tone at the readout frequency and monitoring the reflected phase, the presence of the qubit can be determined by sweeping flux applied

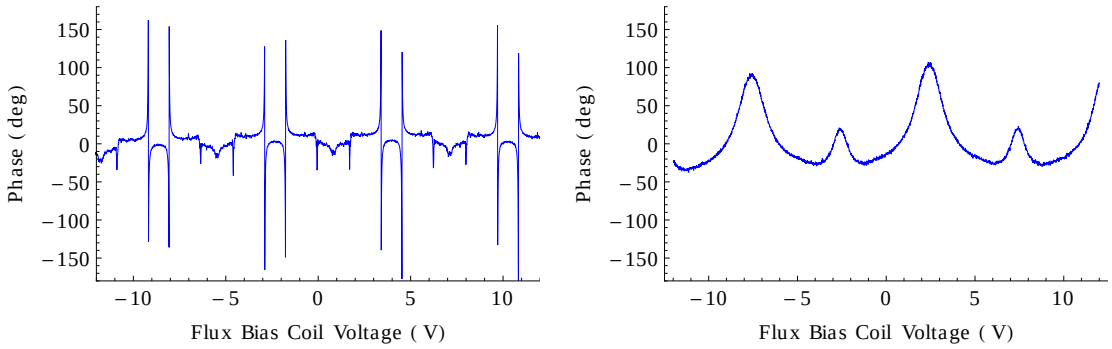

Figure 5.2: Modulation of the readout resonator in sample 2 (left) and sample 5 (right) versus applied flux to the qubit over several flux quanta. Sample 2 is capacitively coupled, and the qubit crosses the readout (8.093 GHz), which can be seen as the sharp changes in phase. Sample 5 is inductively coupled, and the qubit does not cross the readout (7.589 GHz). The difference in periodicity between the two samples is due to changes in proximity to the flux bias coil.

to the qubit, without any need to excite the qubit out of the ground state. The mere presence of the qubit coupled to the resonator will push or pull the resonator from its bare resonant frequency, as described by Equation (2.30) for capacitive coupling and Equation (2.33) for inductive coupling. The shift in readout frequency is flux dependent, as the n and φ matrix elements and transition energies are flux dependent. The result is a periodic shift in resonator response as flux is swept, with large shifts in phase if the qubit comes into resonance with the readout resonator. The shifts in resonator frequency are observed as changes in reflected phase (or amplitude for less overcoupled resonators), examples of which are shown in Figure 5.2. The response function Equation (5.1) describes how frequency shifts translate into phase and amplitude response.

5.1.3 Two-Tone Spectroscopy

In order to determine the transition energies of the qubit, a two-tone measurement is utilized. The first tone is a probe, stepped in frequency across some qubit transition.

At each frequency step of the probe tone, a second fixed-frequency readout tone is sent to the readout resonator, and the reflected readout tone is measured to determine the qubit state. When the probe tone excites a transition, the readout resonator will shift in resonant frequency, resulting in a change in phase of the reflected readout tone. At each probe tone frequency, the measurement is repeated tens of thousands of times.

Two-tone spectroscopy may be done in a pulsed or continuous manner. In pulsed spectroscopy, the probe tone is first applied for some period of time, then the readout tone is applied to record the qubit state. The probe tone is pulsed for a time of order T_1, the energy relaxation time of the qubit. This allows the average qubit population to saturated to 50% excitation. If a shorter duration pulse were applied, the qubit may not be tracked as reliably, as there may be unfortunate coincidence where the length of the probe tone would coincide closely with an $2N\pi$-pulse, where N is an integer. This coincidence would result in the qubit flipping between an excited state and ground N times before leaving the qubit near the ground state.

The advantage of pulsed spectroscopy is that there is no risk in stark shifting the qubit with the readout tone. When the qubit is probed, only a single tone is applied, then the qubit is read out immediately afterwards.

When the dispersive shift is very weak, a continuous measurement may be utilized, where both the probe and readout tones are continuously applied. This method has the advantage that the readout tone may be averaged for arbitrarily long periods of time.

5.1.4 Time Domain Measurements

In this section, typical time domain measurements will be briefly explained. These are standard qubit experiments, with their origins lying in NMR. Characteristic times are

carried over from NMR, where T_1 represents the energy relaxation time (longitudinal decay, known as spin-lattice relaxation time in NMR), and T_2 represents decoherence of the population (transverse decay, known as spin-spin relaxation in NMR) [90, 91]. When the decoherence in NMR is caused by an inhomogeneous magnetic field applied to the sample, the precessional rate of the spins will differ, resulting in a transverse decay which is shorter than that due to just random fluctuations in the field between spins. The decay time due to a fixed field inhomogeneity is referred to as T_2^*. Since only a single qubit is measured, in order to build up a "population" the experimental pulse sequences are repeated tens of thousands of times, and the qubit response is averaged within an Acqiris data acquisition card (see Section 4.5). The averaged data is then analyzed as an effective qubit population.

Rabi Oscillations

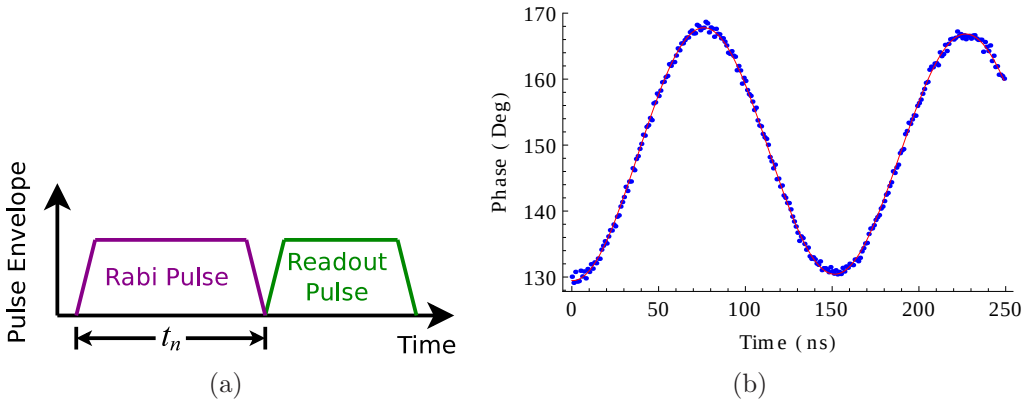

Figure 5.3: (a) Pulse sequence used to generate Rabi oscillations. The drive on the qubit is applied for variable time t_n. (b) Example of a Rabi oscillation experiment in sample 2, biased at $\Phi_{\text{ext}} = 0.195\Phi_0$. A fit of a sinusoid with an exponential decay is shown in red.

In a Rabi experiment, a drive is applied to the qubit a variable length of time before reading out the state of the qubit. The drive rotates the qubit about an axis

perpendicular to the poles of the Bloch sphere, resulting in a sinusoidal oscillation of the qubit population. The oscillation frequency is proportional to the drive amplitude [92]. The pulse sequence and an example Rabi oscillation are shown in Figure 5.3. By performing this experiment, a $\pi/2$-pulse and π-pulse may be calibrated for use in other experiments (such as measuring the energy relaxation time, explained below).

Energy Relaxation Time (T_1)

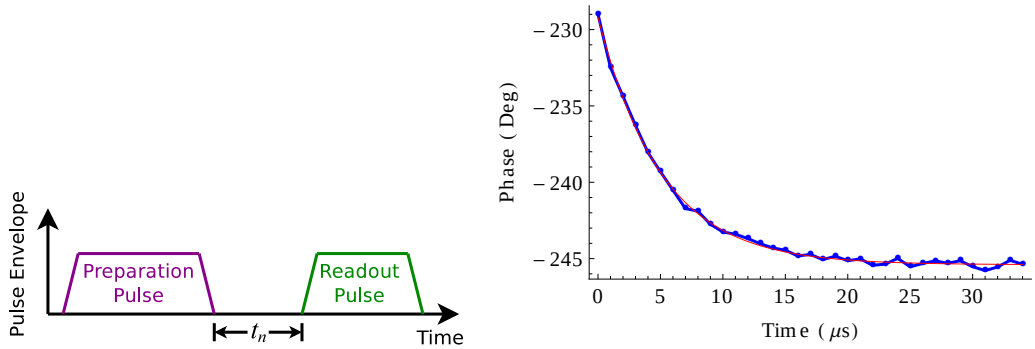

Figure 5.4: (a) Pulse sequence used to measure the energy relaxation time. After a preparation pulse excites the qubit, a variable delay of length t_n is applied before reading the qubit state. (b) Example of an energy relaxation experiment in sample 2, biased at $\Phi_{\text{ext}} = 0.195\Phi_0$. An exponential decay fit is shown in red.

To measure the energy relaxation time T_1 of the qubit, a preparation pulse is first applied to the qubit to populate the excited state. The preparation pulse is typically a π-pulse, which may be determined through Rabi oscillations, or alternatively a sideband pulse may be used (see Section 5.2). A long saturation pulse may be applied without the need to perform a Rabi experiment, but at the cost of a $\sim$50% reduction in signal (since half the saturated population will already be in the ground state). The saturation method is useful when T_1 times are low enough that Rabi flops are not possible, or for automated experiments where automatically determining a π pulse is difficult. After the preparation pulse, the state of the qubit is read-out after

a variable delay. The result is an exponential decay in the qubit population versus wait time, as shown in an example experiment in Figure 5.4. The decay constant gives the T_1 time, the qubit's energy relaxation time.

Ramsey Oscillations (T_2^*)

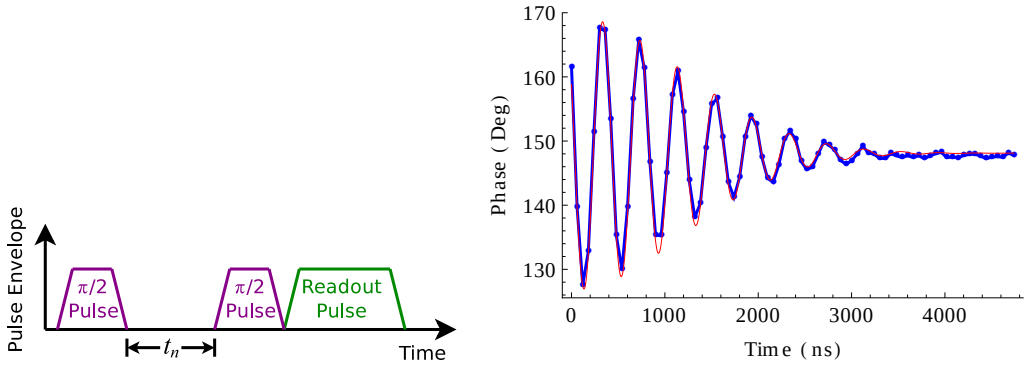

Figure 5.5: (a) Pulse sequence used to generate Ramsey oscillations. A variable delay of length t_n is placed between two $\pi/2$-pulses. The qubit state is read out immediately after the last $\pi/2$-pulse. (b) Example of a Ramsey oscillation in sample 2, biased at $\Phi_{\text{ext}} = 0.195\Phi_0$. A fit of a sinusoid a Gaussian envelope is shown in red.

In a Ramsey experiment, a $\pi/2$-pulse places the qubit in the x-y plane of the Bloch sphere. The qubit is allowed to precess for a variable amount of time before a second $\pi/2$-pulse is applied before projecting the qubit on the z-axis [93]. When the $\pi/2$-pulses are on resonance with the qubit, the resultant data from the experiment is a decay envelope which is either Gaussian (if the coherence time is dephasing limited with $1/f$ noise) or exponential (if the coherence time is T_1 limited, or dephasing limited with white noise) [94, 95]. Any detuning in the $\pi/2$-pulses will result in oscillations equal in frequency to the detuning. Small detunings are inevitable, and difficult to deconvolve from the decay envelope. Therefore, the $\pi/2$-pulses are deliberately detuned from the qubit, such that the oscillations and decay envelope can be

reliably fit simultaneously. An example Ramsey oscillation is shown in Figure 5.5. The decay constant of the Ramsey oscillation give the T_2^* time for the qubit.

Spin Echo (T_2^{echo})

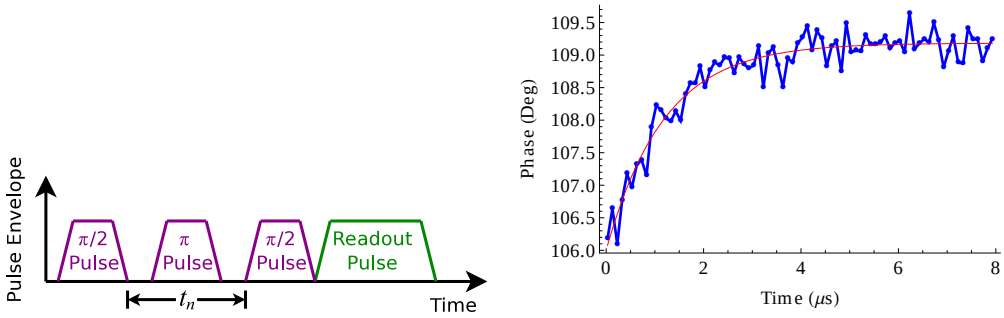

(a) (b)

Figure 5.6: (a) Pulse sequence used for spin echo. A variable delay of length t_n is placed between two $\pi/2$-pulses, with a refocusing π-pulse centered between the two $\pi/2$-pulses. The qubit state is read out immediately after the last $\pi/2$-pulse. (b) Example of spin echo in sample 2, biased at $\Phi_{\text{ext}} = 0.079\Phi_0$. An exponential fit is shown in red.

A spin echo experiment utilizes a refocusing pulse to cancel variations in the precessional rate along the equatorial plane between measurements in the qubit ensemble. In NMR, spin echo is used to correct for field inhomogeneity across spins [96]. In our case, echo can correct for noise sources which affect the precessional rate slowly with respect to the time it takes to perform a single qubit measurement. The pulse sequence, shown in Figure 5.6, is the same as that of a Ramsey experiment with a π-pulse added between the $\pi/2$-pulses. Visualizing the qubit ensemble, the first $\pi/2$-pulse rotates the qubit population into the equatorial plane. The ensemble will start to precess, with some variation in the precessional rate between qubits. Qubits with faster precessional rates will move ahead those with slower precessional rates, causing the distribution to spread along the equatorial plane. The π-pulse then flips the ensemble around 180° (around the same axis as the $\pi/2$-pulse), reversing the

order of each qubit on the equatorial plane; now the fastest qubits are the furthest behind. By the time the next $\pi/2$-pulse arrives, the fastest precessing qubits have now caught up with the slowest precessing qubits, and the ensemble has "refocused" before being projected back on the z-axis by the final $\pi/2$-pulse. The time constant of the resultant decay as the $\pi/2$-pulses are separated in time is T_2^{echo}.

By using multiple refocusing pulses within a given time interval, faster sources of noise may be echoed away. Using such multi-pulse sequences, detailed characterization of the noise present in a qubit may be performed, as was done for a flux qubit in reference [2].

5.1.5 Resonator Photon Number Calibration from AC Stark Shift

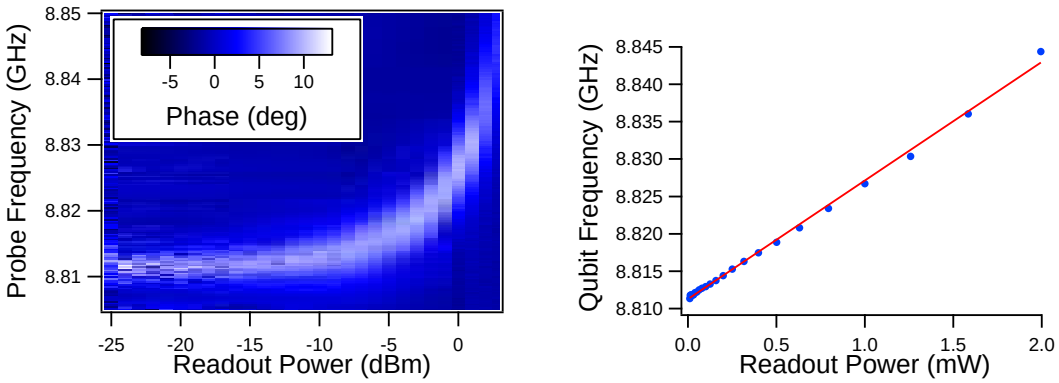

(a) (b)

Figure 5.7: (a) An example of the AC Stark shift on sample 2, biased at $\Phi_{\text{ext}} = 0.052\Phi_0$. (b) The shift in qubit transition frequency has a linear dependence on readout power, the slope of which may be used in conjunction with a measurement of χ_{eg} to convert readout power to average number of photons in the readout resonator.

The AC Stark shift of the qubit transition from g to e with n photons in the

resonator is given by

$$\begin{aligned}\delta\nu_{eg}(n) &= \frac{1}{h}(E_{e,n} - E_{g,n}) - \frac{1}{h}(E_{e,0} - E_{g,0}) \\ &= \frac{1}{h}(\delta E_{e,n} - \delta E_{g,n}) - \frac{1}{h}(\delta E_{e,0} - \delta E_{g,0}) \\ &= \frac{1}{h}(\delta E_{e,n} - \delta E_{e,0}) - \frac{1}{h}(\delta E_{g,n} - \delta E_{g,0}) \\ &= n\chi_e - n\chi_g = n\chi_{eg}.\end{aligned} \tag{5.3}$$

This derivation is correct for both capacitive and inductive coupling, however $\delta E_{\alpha,l}$ and χ_α are given by different expressions (Equations (2.29) and 2.30 for capacitive coupling, and Equations (2.32) and 2.33 for inductive coupling). We see that the shift in qubit frequency has a linear dependence on the number of photons in the readout resonator, and therefore on readout power, as demonstrated by data in Figure 5.7 [97]. Dividing both sides of the expression by the readout power P' sent into the refrigerator from room temperature microwave source, and rearranging terms, we have

$$\frac{\bar{n}}{P'} = \frac{\Delta\nu_{eg}}{P'}\frac{1}{\chi_{eg}}, \tag{5.4}$$

where $\frac{\Delta\nu_{eg}}{P'}$ is our experimentally measured slope of qubit frequency versus readout power, and χ_{eg} can be measured in other experiments described in Subsection 5.1.6. Our desired calibration of average readout photon number in terms of microwave generator power $\frac{\bar{n}}{P'}$ is now given in terms of measurable quantities.

5.1.6 Measuring Dispersive Shift

In order to directly observe the dispersive shift the qubit exerts on the readout resonator, the readout response may be measured directly after a preparation pulse (pulse sequence illustrated in Figure 5.8(a)). In order to measure the readout res-

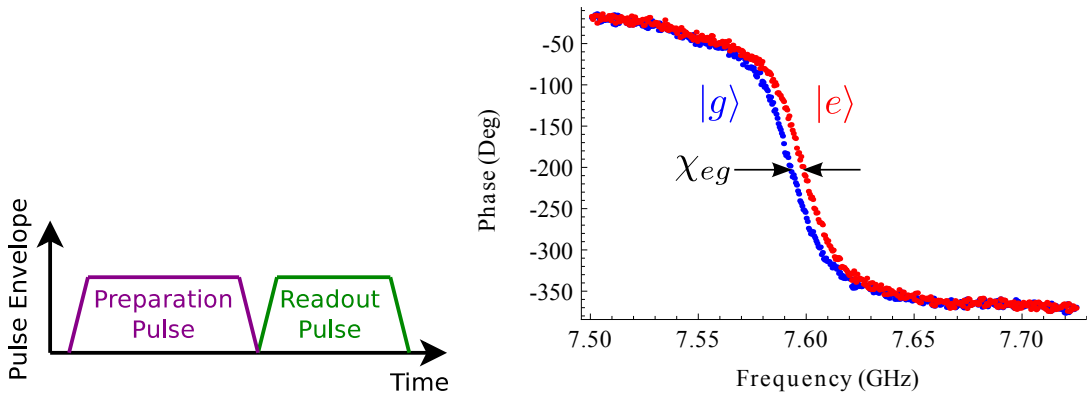

Figure 5.8: (a) Pulse sequence used to acquire readout resonator response. The preparation pulse may be a π-pulse or blue sideband pulse to prepare the e state of the qubit, and a blank pulse or red sideband pulse to prepare the g state. After the preparation pulse, the readout pulse at a particular frequency is applied to measure the response of the resonator. At each readout frequency, the experiment is repeated tens of thousands of times and averaged. The readout frequency is then stepped, and the experiment repeated with the new readout frequency to build up the response profile of the resonator. (b) Dispersive shift of readout resonator in sample 5 biased at $\Phi_{\text{ext}} = 0.5\Phi_0$. The blue points are data for the readout response when the qubit is in the ground state (no preparation pulse), while the red points are the readout response data taken after a π-pulse excites the qubit into the first excited state.

onator response while the qubit is in the ground state, the preparation pulse is left blank when the g–e transition energy is large compared to thermal fluctuations ($h\nu_{eg} \gg k_B T$). If the g–e transition frequency is comparable to thermal fluctuations, the qubit may be prepared in the ground state by applying a pulse at the red sideband transition between the qubit and readout resonator (see Section 5.2). The first excited state may be prepared by applying a π-pulse ($h\nu_{eg} \gg k_B T$) or blue sideband pulse ($h\nu_{eg} \gtrsim k_B T$).

When the dispersive shift is small, or the qubit cannot be reliably prepared, the dispersive shift may be determined through a spectroscopic measurement. With a weak continuous readout tone (weak enough that the qubit is minimally perturbed through the AC Stark shift), a second continuous tone sweeps across the qubit. As

the qubit tone increases in power, the phase response of the spectroscopic peak will increase until the average qubit population is saturated at 50%. The full phase response is twice the saturation value. The dispersive shift may then be found through the slope of the readout resonator response, $\chi_{eg} = 2\Delta\theta/\text{slope}$, where $\Delta\theta$ is the saturated phase response of the spectroscopic peak.

5.2 State Preparation with Readout Resonator Sidebands

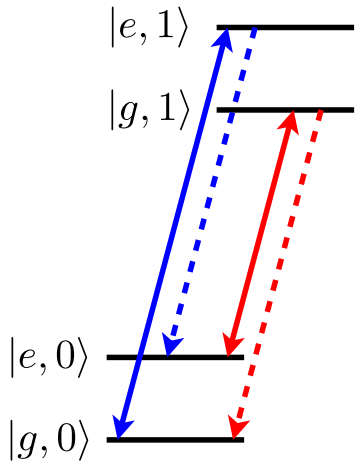

Figure 5.9: Level structure of the qubit and readout resonator with sideband transitions. The red and blue sidebands are shown as solid red and blue lines, respectively. The dashed red and blue lines show the decay channels into the final prepared state when the red and blue sidebands are applied.

When fluxonium is biased near a half flux quantum, the g–e transition is at it's minimal value, and results in a significant thermal population of the e state. The use of sideband cooling for cooling the motional state of strongly trapped atoms has been well established [98, 99, 100], and the technique can be readily applied to preparing the state of fluxonium. Similar techniques have been employed in flux qubits, using

the lossy second excited state of the qubit to quickly empty the thermally populated first excited state to ground [101].

The lowest levels of the fluxonium qubit and readout resonator are illustrated in Figure 5.9 with the sideband transitions shown as solid lines with arrows. The readout resonator is strongly coupled to the microwave environment, resulting in a lifetime which is significantly shorter than the qubit ($Q_{\text{ext}}/f_R \ll T_1$). In order to prepare the qubit in the ground state, a microwave tone at the red sideband is applied, which couples $|e,0\rangle$ to $|g,1\rangle$. If the qubit is in the e state, the red sideband will populate $|g,1\rangle$, which will quickly decay into $|g,0\rangle$ when the readout resonator loses a photon to the external environment (represented as the dashed red line in Figure 5.9). When the system is in $|g,0\rangle$ the red sideband tone has no effect. Similarly, applying a microwave tone at the blue sideband transition couples the states $|g,0\rangle$ and $|e,1\rangle$. If the qubit is in g, the blue sideband will populate $|e,1\rangle$ which quickly decays to $|e,0\rangle$. Once in $|e,0\rangle$ the blue sideband tone does not have any effect.

To demonstrate the effect of sideband preparation, a Rabi oscillation experiment may be performed after application of a sideband pulse. Figure 5.10 shows the pulse sequence used and result of such an experiment. Application of the red sideband prepares the ground state, producing Rabi oscillation with enhanced response relative to that which is obtained without preparation when a significant portion of the qubit population is thermally excited. After application of the blue sideband, the Rabi oscillations are inverted.

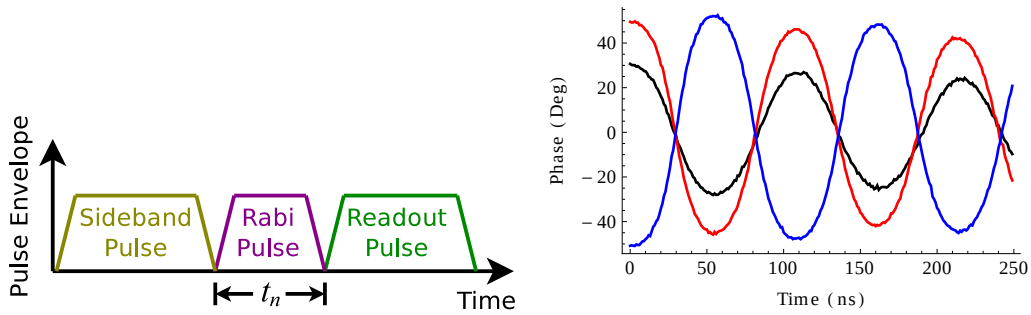

Figure 5.10: (a) Pulse sequence used to prepare the qubit state and produce Rabi oscillations. The pulse sequence is identical to that of a typical Rabi experiment explained in Subsection 5.1.4, but immediately before the Rabi drive, the sideband preparation is applied. (b) Rabi oscillations without state preparation (black), and after red and blue sideband preparation (red and blue traces, respectively) of sample 4 biased at $\Phi_{\text{ext}} = 0.477\Phi_0$.

5.3 Single Shot Measurement

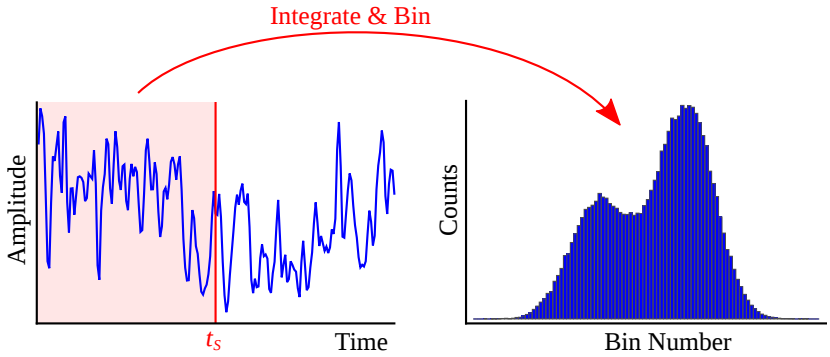

Figure 5.11: Illustration of a single shot measurement.

In a single shot measurement, rather than repeating an experiment many times and averaging together the responses to get the expectation value for an ensemble of qubits, each measurement is analyzed individually. From an individual measurement, the projected state of the qubit may be estimated. To perform a single shot measurement, a microwave pulse at the readout frequency is sent to the sample, and the reflected pulse is mixed down and sent to the data acquisition card as usual. The

acquired pulse is demodulated digitally into I and Q quadrature amplitudes versus time (the phase of a reference signal is subtracted as explained in Section 4.5). The time dependent I and Q signals are then integrated over a sampling time t_S, yielding an I and Q amplitude for the measurement. After this process has been repeated many times, the collection of I and Q amplitudes may be histogrammed to show the distribution of results, as illustrated for a single quadrature in Figure 5.11.

In the data presented in this section, integration of single shot data over the sampling time is equally weighted (the rectangular or "boxcar" window). The sampling time was adjusted to achieve the highest fidelity. In order to place more weight on initial data which is less likely to have transited states, as well as reduce the significance of the sampling time length, an exponential weight function with decay time of order T_1 may be used. Using an exponential weight function did not have a noticeable impact on the fidelity of current single shot measurements of fluxonium. Non-linear functions which modify the weight placed on later data based on the result of earlier data within a trace also exist, but only have a significant impact when fidelities are already very high [102].

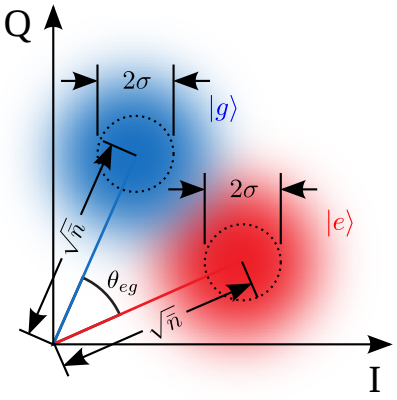

Figure 5.12: Illustration of the single shot distribution for the g and e states in the I-Q plane.

When the readout resonator is driven for readout, a coherent state $|\alpha\rangle$ is pro-

duced in the resonator. Depending on the state of the qubit, the shift in resonator frequency will result in a phase shift of the coherent state which is read out. The distribution of measurement outcomes in the I-Q plane may be visualized as illustrated in Figure 5.12, where the g and e states are witnessed through a bimodal distribution. I and Q are the real and imaginary parts of α, defined as

$$\hat{I} = \frac{\hat{a} + \hat{a}^\dagger}{2}, \tag{5.5}$$

$$\hat{Q} = \frac{\hat{a} - \hat{a}^\dagger}{2i}, \tag{5.6}$$

where a and $a^\dagger$ are the photon annihilation and creation operators, following the commutation relation $[\hat{a}, \hat{a}^\dagger] = 1$. Assuming no losses in the sample, any readout photons sent in will be reflected back out. Therefore, regardless of the state of the qubit, the distance between the center of both the g and e distributions and the origin of the I-Q plane will be $\sqrt{\bar{n}}$, where $\bar{n}$ is the average number of photons populating the readout resonator during readout [103]:

$$\langle\alpha|\hat{I}|\alpha\rangle^2 + \langle\alpha|\hat{Q}|\alpha\rangle^2 = \langle\alpha|\hat{a}^\dagger\hat{a}|\alpha\rangle = |\alpha|^2 = \bar{n}. \tag{5.7}$$

The distributions for the g and e states have a Gaussian profile, with a width given by the quantum noise of a half photon in the readout resonator, in addition to the noise of the measurement setup. In a well designed setup, the system noise should be dominated by the first amplifier in the setup (in our case a HEMT amplifier, in other cases a SQUID amplifier [104] or JPC [105]) which is at a lower noise temperature than any of the following amplifiers. When an average readout resonator occupancy of one photon is used to read out (where photons act as elementary samples), the

width due to quantum fluctuations is

$$\sigma_0^2 = \langle\alpha|(\hat{I} - \langle\hat{I}\rangle)^2|\alpha\rangle = \langle\alpha|(\hat{Q} - \langle\hat{Q}\rangle)^2|\alpha\rangle = \frac{1}{4}. \tag{5.8}$$

As the signal proceeds through the measurement setup, it is amplified, and many photons worth of information are typically measured over the sampling time. The amplifiers will add noise photons to the signal, increasing the width of the Gaussian profiles, while measuring many photons will reduce the width as $1/\sqrt{\bar{n}_S}$, where $\bar{n}_S$ is the average number of photons sampled. The number of noise photons injected by the amplifiers at noise temperature T_N is given by $k_B T_N/(h\nu_R)$. The resultant width of the measured g and e distributions is

$$\sigma_S = \frac{1}{\sqrt{\bar{n}_S}}\sqrt{\sigma_0^2 + \frac{k_B T_N}{2h\nu_R}}. \tag{5.9}$$

The average number of photons sampled is given by

$$\bar{n}_S = \frac{P t_S}{h\nu_R}, \tag{5.10}$$

where P is the readout tone power sent to the sample. The readout power sent to the sample is not known directly, as the attenuation of the cryogenic setup is not precisely known when cold. Rather, given a power at room temperature sent down the refrigerator, the average number of photons populating the resonator is known through an AC Stark shift experiment (see Subsection 5.1.5). With the average number of photons populating the readout resonator, $\bar{n}$, the readout power is

$$P = \bar{n} h\nu_R \kappa, \tag{5.11}$$

where $\kappa = 2\pi\nu_R/Q_{\text{ext}}$ is the rate at which energy leaks out of the readout resonator, and ν_R is the readout resonator frequency. Combining Equation (5.10) and Equation (5.11), we obtain the more experimentally useful result

$$\bar{n}_S = \bar{n}\kappa t_S. \tag{5.12}$$

Increasing $\bar{n}_S$, either through higher readout power or longer sampling, will narrow the g and e distributions. However, if the sampling time is long compared to T_1, or the rate at which the qubit transitions due to thermal fluctuations, the distributions will tend to spread. Additionally, if the readout power is set too high it may induce transitions in the qubit.

The phase separation between the g and e distributions originates from Equation (5.2) and Equation (2.30) for capacitive coupling or Equation (2.33) for inductive coupling, and is given by

$$\begin{aligned}\theta_{eg} &= 2\arctan\left(-2Q_{\text{ext}}\frac{\nu-\nu_R-\chi_e}{\nu_R+\chi_e}\right) - 2\arctan\left(-2Q_{\text{ext}}\frac{\nu-\nu_R-\chi_g}{\nu_R+\chi_g}\right) \\ &\approx 8\pi\frac{\chi_{eg}}{\kappa} \qquad \text{for } \chi_g, \chi_e < \frac{\kappa}{4\pi},\end{aligned} \tag{5.13}$$

where ν is the readout frequency used and ν_R is the resonant frequency of the unperturbed readout resonator. The phase separation is fixed, regardless of sampling time or readout power. The signal-to-noise ratio (SNR) is given by the separation of the states divided by the distribution widths, in power:

$$\text{SNR} = \frac{2\bar{n}_S(1-\cos\theta_{eg})}{\sigma_S^2}. \tag{5.14}$$

When the location of the of the distributions are known, the quadrature axes may be rotated into a frame where all information about the qubit state is projected

on a single axis. A threshold separating the states along the projection axis may then be set. When a measurement ends up on one side of the threshold, the state may be predicted as being in g, whereas if it is on the opposite side it is predicted as being in e. To quantify our ability to predict the state of the qubit after a single shot measurement, the fidelity is used as a figure of merit. The fidelity is defined as

$$F = 1 - P(e|g) - P(g|e), \tag{5.15}$$

where $P(\alpha|\beta)$ is the probability of predicting the qubit as being in state α when it is in state β. A fidelity of 1 indicates perfect perfect readout with no errors, while a fidelity of 0 means no information is gained in the measurement and predictions are completely random. The fidelity may also be quoted as a percentage.

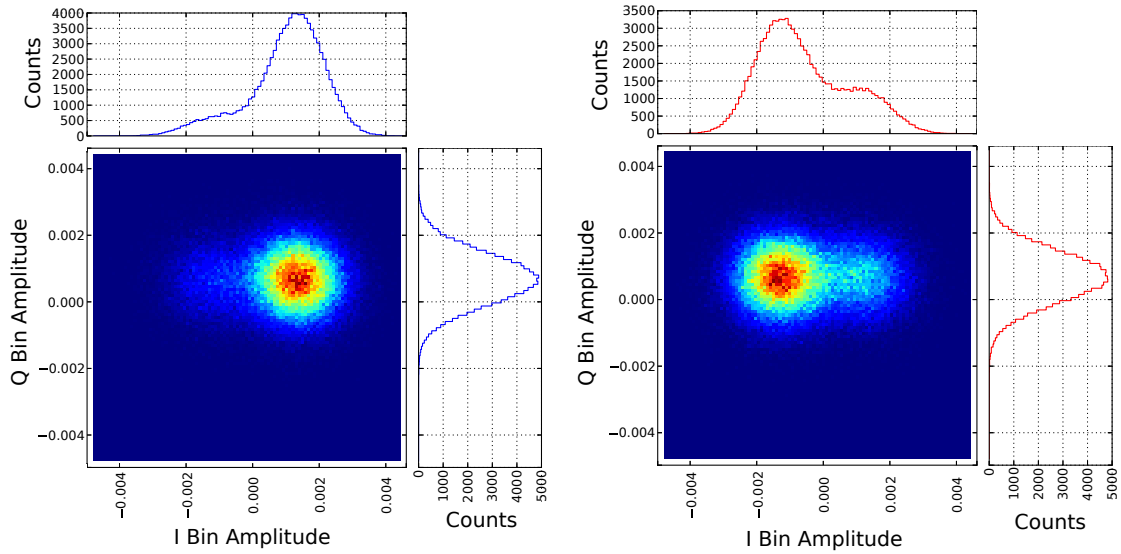

(a) Red sideband prepared $|g\rangle$ (b) Blue sideband prepared $|e\rangle$

Figure 5.13: Single shot distributions for g and e prepared states of sample 1, measured at $\Phi_{\text{ext}} = 0.497\Phi_0$. The readout power was set to $\bar{n}_S = 2.5$ photons, with a sampling time of 1200 ns. 10^5 shots were taken for both the g and e prepared states. Above and to the right of the density plots are projections onto the I and Q axes.

To measure the fidelity, single shot measurements are taken after preparing in

the g and e states. The distributions from the two sets of measurements are used to define the g and e states, and the fidelity is calculated across possible values for the threshold to find the optimal location. Density plots in the I-Q plane, as well as their histogram projections to the I and Q quadratures are shown in Figure 5.13 for single shot data of sample 1 biased at $\Phi_{\text{ext}} = 0.497\Phi_0$. The ground and first excited states are prepared by applying pulses at the red and blue sidebands, respectively. The quadrature axes in Figure 5.13 have already been rotated such that all information about the qubit is projected onto the I quadrature; the Q quadrature provides no insight towards the state of the qubit. From the plots, it is clear there are two preferred locations where the data tends to collect, representing the g and e states of the qubit. Both the g and e prepared states show some residual population in the opposite state, which may be due to the qubit transitioning from thermal fluctuations or T_1 decay within the sampling time, imperfect state preparation, or readout induced transitions in the qubit. It should be stressed here that the readout is strictly linear, and at no time in the measurement or analysis was it assumed that there should be exactly two distinct states. The distributions obtained in Figure 5.13 can be considered proof of the quantum nature of the fluxonium circuit.

The I quadrature distributions for the g and e prepared states of sample 1 are shown in Figure 5.14, along with the corresponding fidelity, varying the threshold location. The threshold with maximum fidelity achieves a fidelity of 53%, which does not make any attempt to correct for errors in preparing the qubit state or relaxation of the qubit; it is an "all inclusive" fidelity, not limited to readout visibility. The fact that the residual distributions are clearly discernible and show appreciable residuals indicates the visibility is significantly better than 53%. Given the centroid locations and widths from fitting the acquired distributions with the sum of two Gaussian envelopes (the free parameters are the centroid location and amplitude of the two

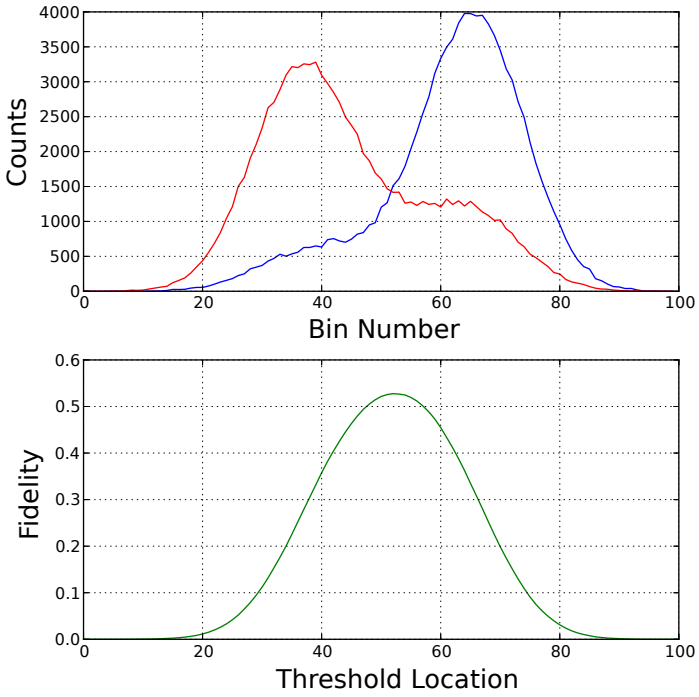

Figure 5.14: Comparison of the g and e prepared state distributions in the I quadrature of the data from Figure 5.13. The fidelity versus threshold location indicates a maximum fidelity of 53%.

Gaussian distributions, and a width which is the same for both Gaussian distributions), the visibility, or fidelity with perfect qubit preparation and no transitions during readout, is 88%, with an SNR of 19.

To test the effect on the qubit of driving the readout resonator, the relaxation time T_1 of the qubit was measured in the presence of readout photons. In a typical relaxation time experiment, as explained in Subsection 5.1.4, after the excited state is prepared a variable delay is placed before reading out the qubit state. This protocol measures the relaxation time with no photons in the readout resonator (other than stray photons which may be present from inadequate shielding or filtering in the setup). In contrast, the relaxation time may be measured continuously, in the presence of readout photons. The qubit is first prepared in the excited state, and immediately following a readout pulse is applied. The reflected readout pulse is

then chopped into segments versus time, with I and Q amplitudes extracted for each segment and averaged over tens of thousands of repeat experiments. The result is an exponential decay in I or Q, representing relaxation in the presence of readout photons.

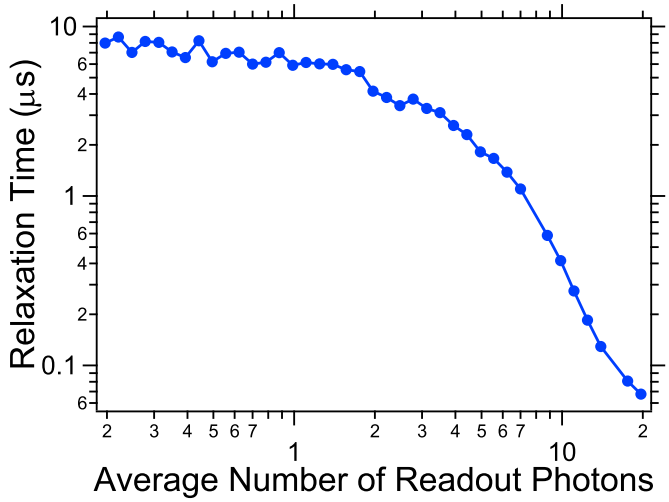

Figure 5.15: Energy relaxation time of sample 1 at $\Phi_{ext} = 0.497\Phi_0$ versus the average number of photons populating the readout resonator. After application of a π-pulse, a readout tone is applied and monitored continuously, and its characteristic decay time extracted. Beyond a few photons in the resonator, there is a clear photon induced reduction in qubit lifetime.

The relaxation time versus the average photon occupation of the readout resonator for sample 1 is plotted in Figure 5.15. Beyond a few photons in the resonator, there is a clear destructive trend in qubit lifetime. This effect is likely due to higher modes of the qubit-readout system coupling, providing additional paths for the qubit to decay. While reading out with higher powers helps to separate the states, it is clear that at higher powers one must compensate for the loss in T_1 by shortening the sampling time, making it non-obvious what readout power results in optimal fidelity.

To find the optimal readout power, single shot measurements were taken with a range of readout powers, and the data sets were analyzed by sweeping integration

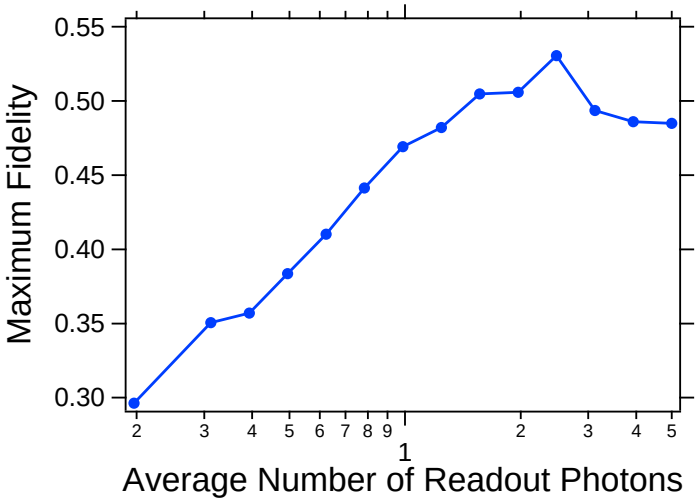

Figure 5.16: Maximum fidelity of sample 1 at $\Phi_{\text{ext}} = 0.497\Phi_0$ versus the average number of photons populated in the readout resonator during readout. At low photon numbers the acquired signal during the qubit lifetime is weak, while at high powers the qubit lifetime is reduced.

times and threshold location to extract the maximum fidelity at each power. The product of this method is Figure 5.16, showing a peak in fidelity around $\bar{n} = 2.5$. The effect of integration time and readout power on the acquired distributions is shown in Figure 5.17 and Figure 5.18, respectively. At higher powers, the qubit lifetime drops faster than the benefits of more readout photons collected per unit time. Below $\bar{n} = 1$ the qubit lifetime does not improve, but the acquired signal is weakened, yielding pronounced losses in fidelity. The empirical result is that only a few photons should be used to read out the state of the qubit, and this regime may be identified quickly by making note at which point the T_1 begins to drop. Further theoretical work is needed to identify which transitions are responsible for the photon induced relaxation, and to determine if the fluxonium parameters may be adjusted to avoid this constraint in the readout.

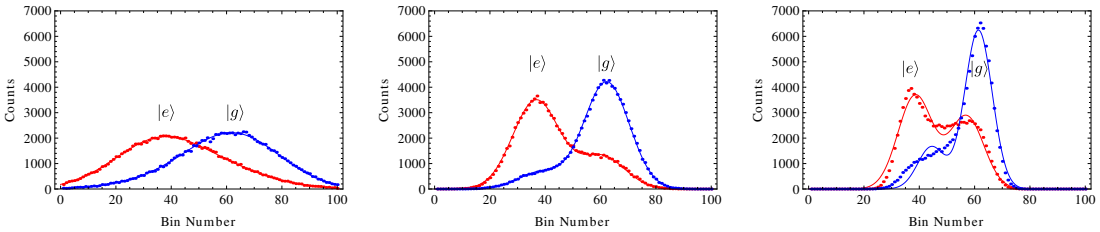

(a) 250 ns (b) 1200 ns (c) 5000 ns

Figure 5.17: Dependence of integration time on the single shot distributions of the g (blue) and e (red) prepared states of sample 1 measured with $\bar{n} = 2.5$ at $\Phi_{\text{ext}} = 0.497\Phi_0$. Solid lines are fits to the data, of two Gaussian distributions. Because the readout power is constant, the peaks of the distributions remain fixed, but as integration time increases the distribution widths narrow as random noise from the amplifiers is averaged away. At long integration times, the effects of T_1 and thermally induced transitions become apparent as displayed in (c), where there is smearing between the two state locations due to transitions occurring within the sampling time. As a result, the fit function does not properly assess the data.

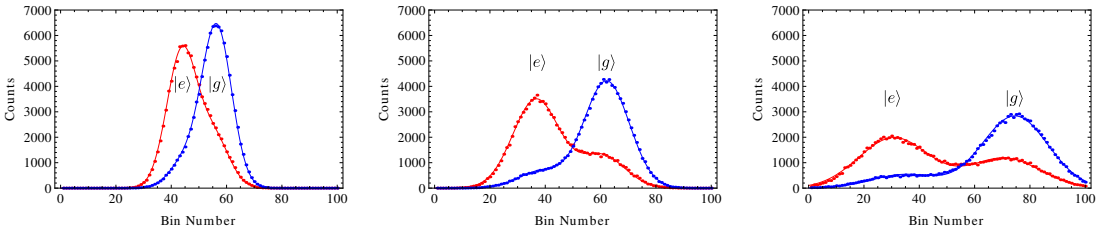

(a) $\bar{n} = 1.2$ photons (b) $\bar{n} = 2.5$ photons (c) $\bar{n} = 5$ photons

Figure 5.18: Dependence of readout power on the single shot distributions of the g (blue) and e (red) prepared states of sample 1 measured at $\Phi_{\text{ext}} = 0.497\Phi_0$, with an integration time of 1200 ns. Solid lines are fits to the data, of two Gaussian distributions. As the photon number increases the distributions spread apart. However, due to non-QND nature of readout photons the distributions also broaden, becoming problematic beyond a readout occupation of a few photons.

5.4 Temperature Measurement

When biased near $\Phi_{\text{ext}} = \frac{1}{2}\Phi_0$, the first excited state of fluxonium is sufficiently low in energy that it may have a significant population due to thermal fluctuations. We can assume the only states with a significant population are g and e, as $h\nu_{eg} \gtrsim k_B T$ and $h\nu_{fe} \gg k_B T$. When the qubit is coupled to a reservoir at temperature T, the ratio of probabilities to be in state e and g is given by

$$\frac{P_e}{P_g} = \mathrm{e}^{-\frac{E_e - E_g}{k_B T}}, \tag{5.16}$$

where P_g and P_e are the ground and first excited state populations, and E_g and E_e are the ground and first excited state energies. Rearranging terms, we see that by measuring the ratio of the g and e state populations, and knowing the g–e transition frequency ν_{eg}, the temperature of the qubit may be inferred by

$$T = \frac{h\nu_{eg}}{k_B \ln\left[\frac{P_g}{P_e}\right]}. \tag{5.17}$$

Because we are only comparing Boltzmann factors (and not concerned with the partition function), this expression is equally valid even when higher states are thermally populated.

In general, measurements of qubit temperature yield numbers higher than that registered on the RuO_2 thermometer on the mixing chamber stage plate. This may be indicative of a strong thermal coupling between the qubit and mixing chamber stage, along with weak couplings to hot reservoirs at liquid helium and room temperatures, and perhaps noise coming from the HEMT amplifiers. Unfortunately, there is not a simple way to determine the coupling strengths and temperatures of any reservoirs which may be coupling to the qubit.

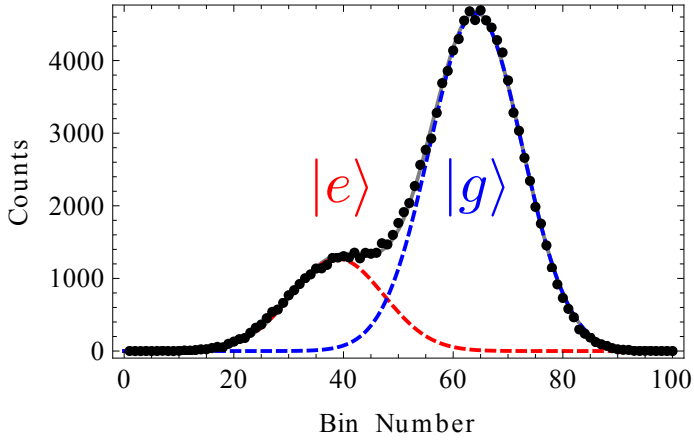

Figure 5.19: Single shot distribution of the steady state of sample 4, biased at $\Phi_{\text{ext}} = 0.477\Phi_0$ ($\nu_{eg} = 1.034$ GHz). 10^5 single shot measurements were taken. Black points indicate the number of counts in each of the 100 data bins. The dashed red and blue curves are fitted Gaussian distributions for the e and g states, respectively, while the solid gray curve is the sum of the distributions. The fit parameters were the Gaussian positions, heights, and width (the same width was used for both states). From the ratio of the area of the distributions, the qubit temperature is extracted as 38.2 ± 0.4 mK, with a ground state population of 78.5%, and excited state population of 21.5%. The uncertainty is the standard error of the Levenberg-Marquardt fitting algorithm. The temperature of the mixing chamber stage of the refrigerator was 13 mK, as measured by a RuO_2 thermometer mounted on the mixing chamber stage plate.

The most direct way to measure the populations is through a single shot experiment on the steady state of the qubit, so long as the g and e states are well resolved. Single shot data of sample 4 is shown in Figure 5.19. The temperature of the mixing chamber stage of the refrigerator was 13 mK. Gaussian distributions for the g and e states are fit to the single shot distribution, and from the ratio of the areas of the two Gaussian distributions the temperature may be inferred.

An alternate method of acquiring the steady state population is to use red and blue sideband transitions (see Section 5.2) to prepare the qubit population into the g and e states, respectively, then measure the subsequent decay into the steady state. The ratio of the amplitudes of decay from g and e into the steady state is equal

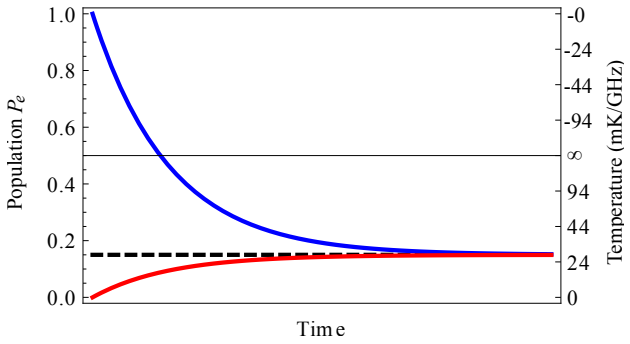

Figure 5.20: Illustration of the decay of red and blue sideband prepared states (in red and blue, respectively) into the steady state population, represented as the dashed black line. The left y-axis corresponds to P_e, the population of state e. The right y-axis shows the corresponding temperature for the steady state location, dependent on ν_{eg}.

to the ratio of P_g to P_e. This is illustrated in Figure 5.20. The initial response of the red and blue sideband prepared decays set the location of P_g and P_e, and both decay to the steady state. The sideband decays for sample 4 are shown in Figure 5.21. The temperature estimated using this method is 30.1 ± 0.3 mK, which is a few millikelvin away from the single shot measurement estimation of 38.2 ± 0.4 mK from Figure 5.19. The uncertainties in both of these temperature measurements come from the standard error of fits using the Levenberg-Marquardt algorithm, and do not take into account other sources of error such as readout fidelity, the qubit decaying before a measurement is taken, errors in the correction of the sideband decay data, or readout induced changes in the population. It is difficult to measure and quantify these errors, but the temperature estimations here are likely only accurate to several millikelvin at best.

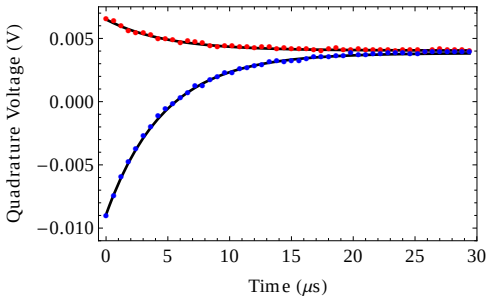

Figure 5.21: Red sideband prepared (red points) and blue sideband prepared (blue points) decays of sample 4, biased at $\Phi_{\text{ext}} = 0.477\Phi_0$ ($\nu_{eg} = 1.034$ GHz). The exponential fits are shown in black. The ground state population is 83.8%, and excited state poplulation is 16.2%. The ratio of the amplitudes of the fits give an effective temperature of 30.1 ± 0.3 mK. Uncertainty in the temperature is from the standard errors of the exponential fits to the data.

5.5 Population Transfer Using Stimulated Raman Adiabatic Passage (STIRAP)

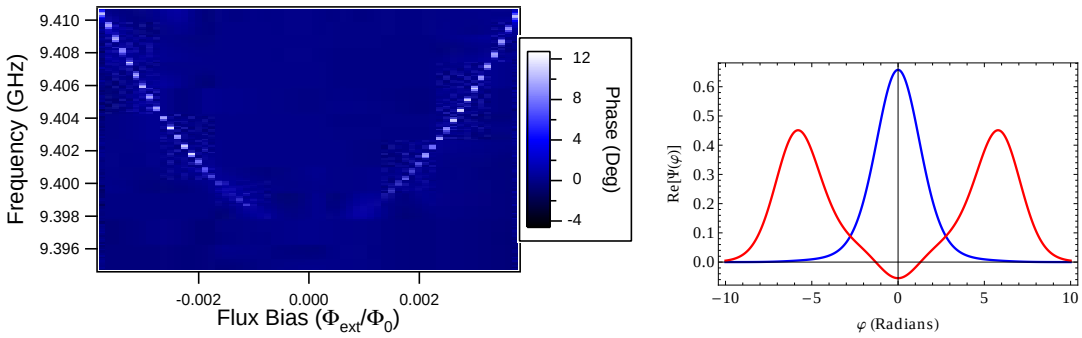

(a) (b)

Figure 5.22: (a) Spectroscopy of the g–f transition in sample 1, showing a hole around zero flux bias due to the symmetry of the states. (b) The wavefunctions of the g (blue) and f (red) states at zero flux bias are both even functions, forbidding single photon transitions between the states.

Due to the symmetry of the ground and second excited states of fluxonium when biased at zero flux, direct dipole transition between these states is forbidden. This forbidden transition is observed as a "hole" in spectroscopy near zero flux bias, as

seen in spectroscopic data of sample 1 in Figure 5.22. By sending an excitation tone directly connecting these states, the transition can be made to happen if enough power is sent, as the qubit is never biased at exactly zero flux. However, the f state can be more reliably populated through an auxiliary level via adiabatic transfer.

Such practices are standard in atomic physics for transitions between states which cannot be accessed directly with a single photon transition due to parity, and may be readily applied to fluxonium. In stimulated Raman adiabatic passage (STIRAP) two partially overlapping pulses allow for population transfer to a target state through an intermediate state, without significantly populating the intermediate state [106]. A Stokes pulse is first applied, which couples the intermediate and target states. As the Stokes pulse is reduced, a pump pulse is applied, connecting the initial and intermediate states. During the overlap of the Stokes and pump pulses, the population is transferred from the initial to the target state while keeping the intermediate state dark. The overlap between pulses must be long compared to the Rabi frequencies coupling the states to keep the sequence adiabatic. Because the qubit population is not transferred into the intermediate state, the intermediate state need not be long lived. Additionally, the Stokes and pump pulses may be detuned from the intermediate state so long as they are detuned by the same amount, at the cost of reduced efficiency (detuning results in slight population of the intermediate state) [107].

To demonstrate STIRAP in fluxonium, sample 1 was biased at zero flux to one part in ten thousand. The qubit is initially in the ground state g, and will be transferred into the second excited state f using the third excited state h as the intermediate state, as illustrated in Figure 5.23. The third excited state was chosen over the first excited state due to the small separation between e and f ($\nu_{fe} = 283$ MHz) which would be less experimentally convenient to work with. However, the third excited state is shorter lived ($T_1^{|h\rangle} = 210$ ns versus $T_1^{|e\rangle} = 440$ ns). With this

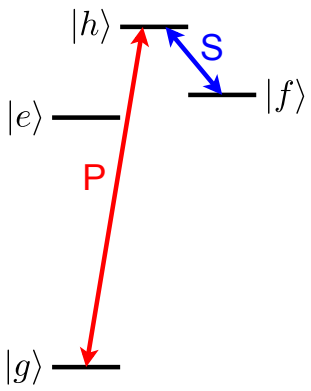

Figure 5.23: Illustration of fluxonium energy levels used to test the STIRAP protocol. Biased at zero flux quantum, the qubit is initially in the ground state g. The qubit is excited into the second excited state f through an intermediate state h without significantly populating the intermediate state. The Stokes pulse (red) connects the intermediate and target states, while the pump pulse (blue) connects the initial and intermediate states.

choice of states, on resonance the Stokes pulse is 1.672 GHz and the pump pulse is 11.070 GHz. Both pulses are modulated with Gaussian envelopes with FWHM = 235 ns ($\sigma = 100$ ns).

The signature of a STIRAP protocol can be observed by sweeping the overlap of the Stokes and pump pulses, shown as the black trace in Figure 5.24. The transfer efficiency to the f state cannot be directly measured, rather the dispersive shift of the readout resonator is observed. At large negative separation times, the pump pulse precedes the Stokes, and some fraction of the g population is coherently driven into h by the pump. The Stokes pulse then coherently drives the h population between the h and f states. What remains in the h state may then decay into f or g. The end result is inefficient transfer into any state, unless the Stokes and Pump pulses are both tuned to coincide with π pulses. At large positive separation times, the Stokes pulse precedes the pump, without overlap. Since the h and f states are both initially empty, the Stokes pulse has no effect. The pump pulse then coherently drives between the g and h state. For separation times where the pulses overlap, there is

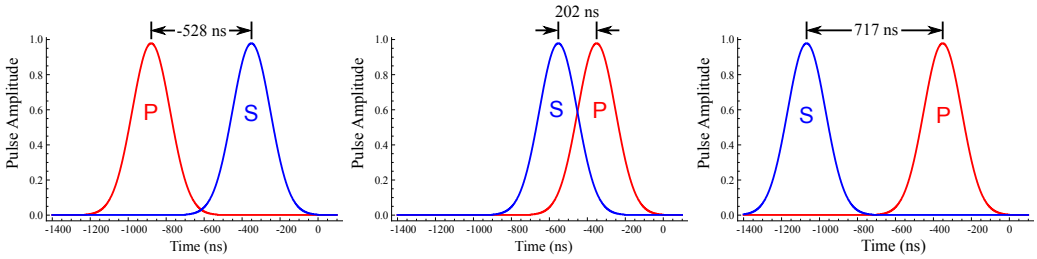

(a)

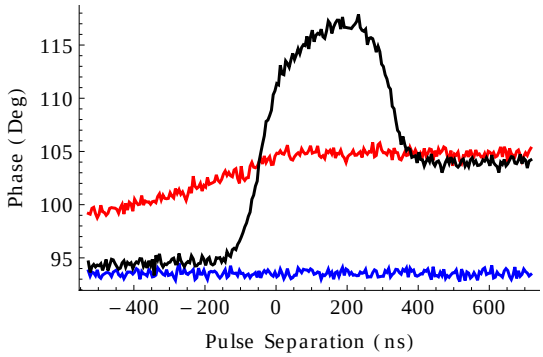

(b)

Figure 5.24: (a) Pulse sequence for testing the STIRAP protocol. The Stokes and probe pulses are both modulated with a Gaussian envelope of FWHM = 235 ns (σ = 100 ns). At positive pulse separation times, the Stokes pulse precedes the pump pulse, at zero pulse separation time they completely overlap, and the pulse order is reversed at negative times. After a time 3.5σ from the last pulse, the state of the qubit is read out (indicated as time 0 in the plots). (b) The signature of a STIRAP protocol as viewed in a dispersive measurement of the qubit state is shown in black. The red data is the same experiment with the pump pulse only (Stokes pulse generator turned off), while the blue data is with the Stokes pulse only. Because there is a variable time delay between the pump pulse and readout for pulse separation times below zero, the red data shows the result of energy relaxation.

a relatively flat region where maximum transfer into f occurs (in the experimental data of Figure 5.24 this happens with a pulse separations near 200 ns).

For comparison, the effect of lone Stokes and pump pulses are also shown in Figure 5.24. The exact same pulse sequence is used, however the microwave generators are selectively turned off. The blue trace shows the effect of the Stokes pulse, which as expected displays no response. The red trace shows the effect of the pump pulse,

which matches the black STIRAP signature at high pulse separation times when the pump no longer has significant overlap with the Stokes pulse (the slight offset is due to shifts in overall phase which can happen over the course of several minutes between experiments). The slope in the red trace at negative times is due to the variable time delay between the pump pulse and readout, and is due to the decay of the h population (this data is essentially showing a T_1 decay). Once positive separation times are reached, the pump pulse is always the last pulse, so the readout always follows immediately after the pump pulse.

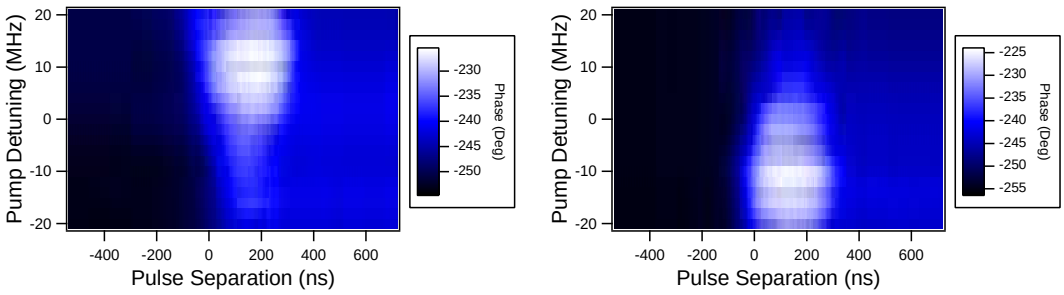

(a) Stokes pulse 10 MHz detuned

(b) Stokes pulse -10 MHz detuned

Figure 5.25: Response of the STIRAP signature when the Stokes pulse is detuned above (a) and below (b) resonance with the intermediate state. When the pump detuning matches the Stokes detuning the usual STIRAP signature is restored.

The adiabatic transfer may be achieved when detuned from the intermediate state, so long as the combined frequencies of the pump and Stokes pulse couple the initial and target states, as demonstrated in Figure 5.25.

Chapter 6

Concluding Summary

The work presented in this thesis has shown the successive reduction in losses in fluxonium over five different samples. The capacitive quality bound was $Q_{\text{cap}} > 6000$ in the initial fluxonium samples. By increasing the electrode gap in the qubit to readout resonator coupling capacitors, the dielectric surface participation ratio was reduced, resulting in a doubling of the capacitive quality factor bound. In switching to an inductive coupling between the qubit and readout resonator, the coupling capacitors were replaced with Josephson junctions, further improving the capacitive quality bound to $Q_{\text{cap}} > 32000$. In addition, the agreement between the basic theory of fluxonium and the five samples proves the robustness and repeatability of the qubit.

The detailed characterization of superinductances formed by an array of Josephson junctions in the regime $E_J \gg E_C$ was performed. The arrays exhibit internal losses less than 20 ppm, self-resonant frequencies greater than 10 GHz, and phase slip rates less than 1 mHz. These results show that systems containing a large number of junctions ($N \sim 100$) do not necessarily suffer from additional losses.

During compilation of this manuscript, work on the improvement of fluxonium

purity has continued, by changing to sapphire substrates, improving filtering and shielding of the sample from external radiation, and utilizing a three-dimensional cavity readout architecture. The sapphire substrate allows for more vigorous cleaning procedures during fabrication, while the cavity in bulk metal minimizes electrical energy stored in potentially lossy dielectrics. Preliminary results appear to be promising for the development of fluxonium samples with millisecond relaxation times.

At this point the understanding of qubit lifetimes and methods for further improvement appear to be well understood. However, long qubit lifetimes are not enough for implementing a useful qubit for quantum computation. While the limiting of the dephasing time due to phase slips in the array has been solved through the extremely low phase slip rates of the superinductances tested, flux noise in the typical 1 $\mu\Phi_0/\sqrt{\text{Hz}}$ @ 1 Hz range will limit fluxonium qubits to dephasing times to the order of 10 μs. Therefore, further research is required to design a topologically protected fluxonium qubit which is far more insensitive to flux noise. Such developments are likely not far off, with proposals in place for incorporating fluxonium in a gradiometric loop which will trap a fixed quantity of flux.

Appendix A

Resonant Circuits

In this appendix chapter, some useful resonant circuit results are derived.

A.1 LC Oscillator Equivalents to Transmission Line Resonators

A.1.1 The LC Oscillator

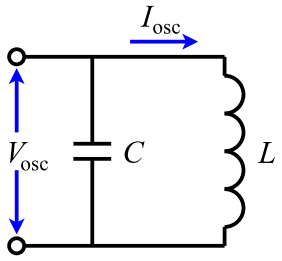

Figure A.1: Schematic of an LC oscillator.

A simple LC oscillator is shown in Figure A.1, with inductance L and capacitance C. When excited, the oscillator has a harmonically varying voltage of amplitude V_{osc} across the capacitor, and current amplitude I_{osc} through the inductor. The energy

E_{tot} stored in the oscillator is given by the sum of the inductive energy E_{ind} and capacitive energy E_{cap}

$$E_{\text{tot}} = E_{\text{ind}} + E_{\text{cap}}, \tag{A.1}$$

$$E_{\text{ind}} = \frac{1}{4} L I_{\text{osc}}^2, \tag{A.2}$$

$$E_{\text{cap}} = \frac{1}{4} C V_{\text{osc}}^2. \tag{A.3}$$

By the equipartition theorem, the capacitive and inductive energies are equal

$$\frac{1}{4} L I_{\text{osc}}^2 = \frac{1}{4} C V_{\text{osc}}^2, \tag{A.4}$$

$$\frac{L}{C} = \frac{V_{\text{osc}}^2}{I_{\text{osc}}^2}, \tag{A.5}$$

from which we see that the oscillator impedance $Z_{\text{osc}} = V_{\text{osc}}/I_{\text{osc}}$ is given by

$$Z_{\text{osc}} = \sqrt{\frac{L}{C}}. \tag{A.6}$$

A.1.2 The Quarter Wavelength Resonator

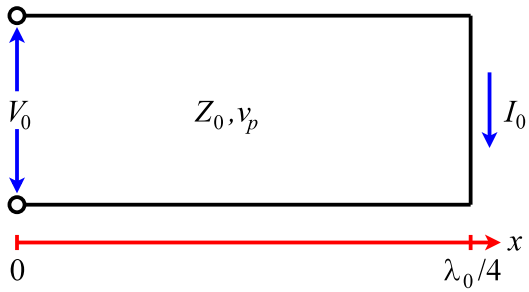

Figure A.2: Schematic of a quarter wavelength transmission line resonator.

A schematic of a quarter wavelength resonator is diagrammed in Figure A.2. It consists of a length $\lambda_0/4$ of transmission line of characteristic impedance Z_0 and

phase velocity v_p shorted at the end. When excited, a standing wave exists along the transmission line, with a voltage amplitude V_0 on the open end, and current amplitude I_0 on the shorted end. The fundamental angular resonant frequency is

$$\omega_0 = \frac{v_p}{\lambda_0}, \tag{A.7}$$

and the propagation constant is

$$\beta_0 = \frac{\omega_0}{v_p}. \tag{A.8}$$

From the impedance $Z_0 = \sqrt{L_l/C_l}$ and phase velocity $v_p = 1/\sqrt{L_l C_l}$, the inductance per unit length L_l and capacitance per unit length C_l of the transmission line are given by

$$L_l = \frac{Z_0}{v_p}, \tag{A.9}$$

and

$$C_l = \frac{1}{Z_0 v_p}. \tag{A.10}$$

The voltage and current along the resonator are given by

$$V(x) = V_0 \sin(\beta_0 x), \tag{A.11}$$

and

$$I(x) = I_0 \cos(\beta_0 x). \tag{A.12}$$

The inductive and capacitive energy stored in the resonator may be calculated by

integrating along the line. The inductive energy is given by

$$\begin{aligned} E_{\text{ind}} &= \frac{1}{4}\int_0^{\lambda_0/4} L_l I^2(x)\,\mathrm{d}x \\ &= \frac{1}{4}\int_0^{\lambda_0/4} \frac{Z_0}{v_p} I_0^2 \cos^2\left(2\pi\frac{x}{\lambda_0}\right)\,\mathrm{d}x \\ &= \frac{Z_0 I_0^2}{4v_p}\int_0^{\pi/2} \cos^2(y)\,\mathrm{d}y\,\frac{\lambda_0}{2\pi} \\ &= \frac{\pi Z_0 I_0^2}{16\omega_0}, \end{aligned} \tag{A.13}$$

and the capacitive energy is given by

$$\begin{aligned} E_{\text{cap}} &= \frac{1}{4}\int_0^{\lambda_0/4} C_l V^2(x)\,\mathrm{d}x \\ &= \frac{1}{4}\int_0^{\lambda_0/4} \frac{1}{Z_0 v_p} V_0^2 \sin^2\left(2\pi\frac{x}{\lambda_0}\right)\,\mathrm{d}x \\ &= \frac{V_0^2}{4Z_0 v_p}\int_0^{\pi/2} \sin^2(y)\,\mathrm{d}y\,\frac{\lambda_0}{2\pi} \\ &= \frac{\pi V_0^2}{16\omega_0 Z_0}. \end{aligned} \tag{A.14}$$

Applying the equipartition theorem ($E_{\text{ind}} = E_{\text{cap}}$), we see there are no surprises

$$\frac{\pi Z_0 I_0^2}{16\omega_0} = \frac{\pi V_0^2}{16\omega_0 Z_0} \tag{A.15}$$

$$Z_0 = \frac{V_0}{I_0}. \tag{A.16}$$

A.1.3 Equivalent LC Oscillators to the Quarter Wavelength Resonator

The purpose of an equivalent LC circuit is to create a simplified model for a resonator when only the fundamental mode is of importance. The equivalent LC inductance L and capacitance C are chosen such that the LC oscillator has a resonant frequency

matching the fundamental mode of the quarter wavelength resonator ($1/\sqrt{LC} = \omega_0$). The impedance of the LC oscillator is the remaining free parameter, which may be adjusted such that the inductor current matches the anti-node current (at the short), or the capacitor voltage matches the anti-node voltage (at the open).

In the case of capacitively coupled fluxonium, the readout resonator voltage is the important quantity, and therefore it is important that the equivalent LC oscillator have the same voltage when excited with a photon of energy. Similarly, in inductively coupled fluxonium the current is the important quantity, so the equivalent LC oscillator must have the same current as the transmission line resonator when excited with a photon. If both current and voltage are important in a particular application, then the LC oscillator may not be an appropriate approximation.

LC Oscillator with Matching Current and Frequency

Matching the inductive energies of the transmission line resonator and equivalent LC oscillator, and setting $I_{\text{osc}} = I_0$, we find the inductance of our equivalent LC oscillator

$$\frac{1}{4} L I_0^2 = \frac{\pi Z_0 I_0^2}{16 \omega_0}, \tag{A.17}$$

$$L = \frac{\pi Z_0}{4 \omega_0}, \tag{A.18}$$

and from $1/\sqrt{LC}$, the capacitance is given by

$$C = \frac{1}{\omega_0^2 L} = \frac{4}{\pi \omega_0 Z_0}. \tag{A.19}$$

The oscillator impedance is

$$Z_{\text{osc}} = \sqrt{\frac{L}{C}} = \frac{\pi}{4} Z_0. \tag{A.20}$$

The oscillator's voltage is related to the transmission line voltage by

$$V_{\text{osc}} = I_{\text{osc}} Z_{\text{osc}} = I_0 \frac{\pi}{4} Z_0 = \frac{\pi}{4} V_0. \tag{A.21}$$

LC Oscillator with Matching Voltage and Frequency

Matching the capacitive energies of the transmission line resonator and equivalent LC oscillator, and setting $V_{\text{osc}} = V_0$, we find the capacitance of our equivalent LC oscillator

$$\frac{1}{4} C V_0^2 = \frac{\pi V_0^2}{16 \omega_0 Z_0}, \tag{A.22}$$

$$C = \frac{\pi}{4 \omega_0 Z_0}, \tag{A.23}$$

and from $1/\sqrt{LC}$, the inductance is given by

$$L = \frac{1}{\omega_0^2 C} = \frac{4 Z_0}{\pi \omega_0}. \tag{A.24}$$

The oscillator impedance is

$$Z_{\text{osc}} = \sqrt{\frac{L}{C}} = \frac{4}{\pi} Z_0. \tag{A.25}$$

The oscillator's current is related to the transmission line current by

$$I_{\text{osc}} = \frac{V_{\text{osc}}}{Z_{\text{osc}}} = \frac{\pi V_0}{4 Z_0} = \frac{\pi}{4} I_0. \tag{A.26}$$

A.2 Parallel RLC with Capacitively Coupled Loads

Resonators used in quantum circuits are commonly coupled to resistive microwave lines for driving and measurement through a coupling capacitance. This section analyzes the modification to the resonant frequency and quality factor of the bare

RLC from the addition of a capacitively coupled resistor.

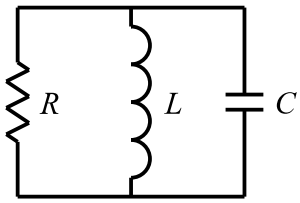

Figure A.3: Schematic of a parallel RLC circuit.

A bare parallel RLC oscillator is shown schematically in Figure A.3. When a harmonic current source drives the resonator, the maximum response (voltage across the resonator in the steady state) occurs when driven at the frequency

$$\omega_1 = \sqrt{\omega_0^2 - \frac{1}{2(RC)^2}}, \tag{A.27}$$

where $\omega_0 = 1/\sqrt{LC}$. The quality factor is given by

$$Q = R\sqrt{\frac{C}{L}}. \tag{A.28}$$

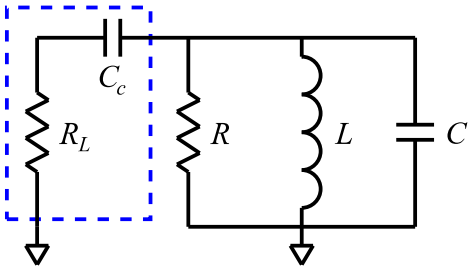

Figure A.4: Schematic of a parallel RLC circuit with a capacitively coupled load resistor R_L.

When the RLC circuit is coupled to a load resistor R_L (which in practice may be microwave drive and measurement lines) through coupling capacitance C_c, as shown in Figure A.4, R_L and C_c form a frequency dependent shunt admittance $Y_L(\omega)$. In

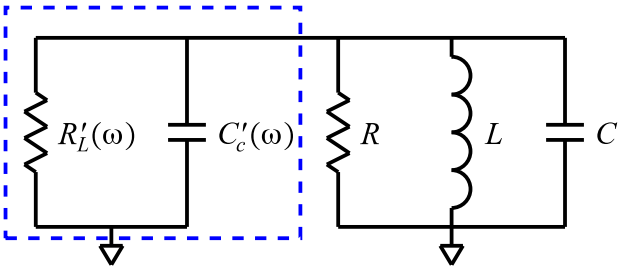

Figure A.5: Equivalent circuit to the parallel RLC with a capacitively coupled load resistor.

order to calculate the resonant frequency and Q of this circuit, the shunt admittance may be modeled as a frequency dependent resistance $R'_L(\omega)$ in parallel with a frequency dependent capacitance $C'_c(\omega)$, as shown in Figure A.5. By converting the circuit into a fully parallel representation, the capacitance and resistance provided by the load may be easily combined with C and R to give the modified resonant frequency and Q. Adjusting Equation (A.27), the driven resonant frequency is

$$\omega'_1 = \sqrt{\frac{1}{L(C + C'_c(\omega'_1))} - \frac{1}{2[(R||R'_L(\omega'_1))(C + C'_c(\omega'_1))]^2}}. \tag{A.29}$$

For an RLC oscillator which is well into the underdamped regime ($Q' \gg \frac{1}{2}$), $R'_L(\omega)$ and $C'_c(\omega)$ may be evaluated at ω_1, avoiding the need to solve for ω'_1. However, in the case of an actual experiment ω'_1 is what is measured, and this equation may be solved for some other unknown parameter. The quality factor is given by adjusting Equation (A.28)

$$Q' = (R||R'_L(\omega'_1))\sqrt{\frac{C + C'_c(\omega'_1)}{L}}. \tag{A.30}$$

We must now obtain $R'_L(\omega)$ and $C'_c(\omega)$ by ensuring they combine to form an admittance which is identical to that provided by R_L and C_c. We have a shunt load

admittance given by

$$Y_L(\omega) = \frac{1}{R_L + \frac{1}{j\omega C_c}}, \tag{A.31}$$

which we use to find the equivalent shunt resistance

$$R'_L(\omega) = \frac{1}{\mathrm{Re}[Y_L(\omega)]} = R_L + \frac{1}{R_L \omega^2 C_c^2}, \tag{A.32}$$

and equivalent shunt capacitance

$$C'_c(\omega) = \frac{1}{\omega}\mathrm{Im}[Y_L(\omega)] = \frac{C_c}{1 + (R_L \omega C_c)^2}. \tag{A.33}$$

Appendix B

Fabrication Recipes

B.1 Fluxonium Device Recipes

B.1.1 Substrate

Sample 1: 2 inch wafer of 300 μm thick silicon, 100 oriented, P-type boron doped, resistivity > 1 k$\Omega \cdot$ cm

Samples 2–4: 2 inch wafer of 500 μm thick silicon, 100 oriented, P-type boron doped, resistivity > 10 k$\Omega \cdot$ cm

Sample 5: 3 inch wafer of 250 μm thick silicon, 100 oriented, N-type phosphorus doped, resistivity > 2 k$\Omega \cdot$ cm, double sided polished with 1.2 μm of silver evaporated on the back

B.1.2 Substrate Cleaning

• Clean substrate with acetone, then methanol in ultrasound for 2 minutes

B.1.3 Resist Spinning

Samples 2–4:

- Spin EL13 @ 5000 RPM for 90 seconds (nominal thickness 500 nm)
- Bake @ 170 °C for 1 minute
- Spin A3 @ 4000 RPM for 90 seconds (nominal thickness 100 nm)
- Bake @ 170 °C for 30 minutes

Sample 5:

- Spin EL13 @ 5000 RPM 90 seconds (nominal thickness 500 nm)
- Bake @ 175 °C for 1 minute
- Spin A3 @ 4000 RPM 90 seconds (nominal thickness 100 nm)
- Bake @ 175 °C for 30 minutes

B.1.4 Development

Samples 2–5: Using tweezers, the written sample is dipped in a solution of MIBK:IPA 3:1 for 50 seconds at 25 °C, gently waving the sample in the solution, followed by 10 seconds in IPA. The sample is then blown off with dry nitrogen.

After development, the sample should be examined under an optical microscope for any faults. After an e-beam layout has been debugged and the doses have been honed in, the main problems which are likely to occur often are accidental scratches on the resist, dust in or on the resist during writing which scatters the beam, or collapsed Dolan bridges in the array or coupling junctions. All of these problems can be spotted after development under an optical microscope before aluminum deposition. Although the bridges are only about 200 nm wide, collapsed bridges are clearly visible as demonstrated in Figure B.1. Even a sample which is bad may

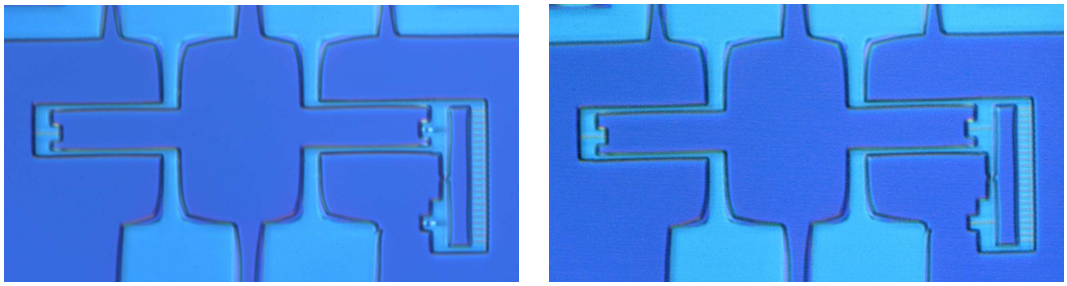

(a) (b)

Figure B.1: Optical microscope image of developed e-beam resist. The device in (a) has two collapsed bridges; the qubit coupling junction, and its symmetric large junction in the qubit loop. In comparison, the device shown in (b) is sample 5, and has no collapsed bridges.

have good test junctions that could be used to test aluminum deposition angles or oxidation parameters.

B.1.5 Aluminum Deposition

Samples 1–4 were evaporated in a Plassys MEB550S single-chamber e-beam evaporation system. Sample 5 was deposited in a Plassys UMS300 UHV multichamber e-beam evaporation system with base pressure of 10^{-9} Torr.

- Titanium sweep
- Evaporate 20 nm onto substrate surface
- Oxidation (15% oxygen, 85% argon)

Sample 1: 10 minutes @ 5 Torr

Sample 2–3: 20 minutes @ 30 Torr

Sample 4: 25 minutes @ 40 Torr

Sample 5: 5 minutes @ 30 Torr

- Evaporate 50 nm onto substrate surface
- Capping oxidation, 10 minutes @ 15 Torr

The time and pressure of the oxidation step between aluminum layers was adjusted such that the room temperature resistance of test arrays (43 junctions) was close to 110 kΩ after a few days of aging. This resistance served as an indicator for oxidation strength. The required oxidation time and pressure to get the same result varies with time, usage of the evaporator, cleanliness of the system, the humidity/weather, and perhaps other factors. Finding the correct parameters is a tedious process which generally requires the fabrication of several samples, adjusting the oxidation time/pressure until the optimal values are found. The test arrays are fabricated on the chip in conjunction with the fluxonium device, so when an array has the correct resistance, the device on that chip may be used. Once optimal oxidation parameters are found, other samples should be fabricated in as short a time frame as possible (preferably within 24 hours).

B.1.6 Lift-off

• Place sample in 65 °C acetone for 1 hour

• With a syringe, spray acetone at sample to fully remove resist and unwanted aluminum

• Without allowing sample to dry, place sample in fresh acetone, and sonicate for 10 seconds

• Rinse sample with acetone, methanol, then blow dry

B.2 Array Resonator Device Recipes

B.2.1 Substrate

2 inch wafer of 430 μm thick C-plane sapphire with 2 μm of silver evaporated on the back

B.2.2 Substrate Cleaning

- Acetone with sonication for 1 minute
- 5 minutes of oxygen plasma, 300 mBar, 300 Watts
- NMP @ 90 °C for 10 minutes
- NMP with ultrasound for 1 minute
- Rinse with acetone and methanol
- Blow dry

B.2.3 Resist Spinning

- Spin EL13 @ 2000 RPM for 100 seconds
- Bake @ 200 °C for 5 minutes
- Spin A4 @ 2000 RPM for 100 seconds
- Bake @ 200 °C for 5 minutes

B.2.4 Gold Film Deposition (for e-beam writing)

Cressington Sputter Coater 108, model number 6002-8

- Sputter for 45 seconds with Argon flow adjusted for 0.08 mBar and current at 30 mA (result is $\sim$ 10 nm of gold)

B.2.5 Development

- Place wafer in potassium iodide/iodine solution for 10 seconds to remove gold film
- Rinse with water
- Develop in 1:3 IPA:water @ 6 °C for 1 minute, without ultrasound
- Continue 15 seconds with ultrasound
- Continue 15 seconds without ultrasound

B.2.6 Oxygen Plasma Cleaning

30 seconds of oxygen plasma, 300 mBar, 100 Watts

B.2.7 Aluminum Deposition

Plassys MEB550S e-beam evaporation system

- 30 seconds oxygen/argon plasma
- Titanium sweep
- Evaporate 30 nm onto substrate surface
- Oxidation (15% oxygen, 85% argon) 10 minutes @ 100 Torr
- Evaporate 50 nm onto substrate surface
- Capping oxidation, 10 minutes @ 15 Torr

B.2.8 Lift-off

- NMP @ 90 °C for 1 hour
- sonicate in NMP for 2 minutes
- Methanol rinse
- Blow dry

B.2.9 Dicing

- Spin S1827 @ 1500 RPM for 120 seconds
- Bake @ 90 °C for 5 minutes
- Dice
- Acetone for 5 minutes
- Rinse with methanol
- Blow dry

Appendix C

Microwave IQ Modulator

An essential component in any superconducting qubit experiment is the equipment used for the generation of microwave pulses. The cost of commercial RF generators with appropriate IQ modulation abilities becomes prohibitively expensive as the number of required generators scale to meet the increasing complexity of multi-qubit experiments. In the course of this thesis work, several homemade IQ modulation schemes were explored to take the place of expensive commercial IQ microwave generators. The IQ modulator should have high carrier suppression (better than 70 dB, on par with commercial options), outputs which are linearly correlated with modulation input powers, and I and Q channels with phase which is independent of modulation power, and 90° apart regardless of modulation frequency. A wide modulation bandwidth is desired ($\sim$1 GHz), with carrier frequencies ranging over any possible qubit transitions (for fluxonium experiments, this can range from hundreds of megahertz up to 15 GHz). And lastly, the device should be simple to use, with minimal calibration steps required. Meeting all these goals is non-trivial, especially when a low-cost solution is desired.

One such device which was explored is explained in the appendix of the thesis

of Chad Rigetti [45], which utilized a string of three mixers in series to provide a high on/off ratio. However, because the modulation signal was simply split between the three mixers, the output amplitude was not linearly dependent on the modulation input. Additionally, the output phase depended on the modulation power. To overcome these artifacts requires a complicated calibration procedure, which must be done at every carrier frequency of interest.

In the implementation presented here, rather than have an IQ modulator which needs to be calibrated at every new frequency, we decided to take an IQ mixer and optimize it at a single carrier frequency, then mix this carrier up or down to the desired frequency. To suppress carrier leakage through the IQ mixer, DC biases are applied to the I and Q ports, and adjusted to obtain destructive interference of the leakage paths. Higher order products of the carrier can be easily filtered away. The carrier is then shaped with single-sideband modulation (SSB), of which the nulling of the suppressed sideband is maximized by adjusting the relative amplitudes of the I and Q modulation inputs either by adjustments from the AWG driving the ports, or with the adjustment of attenuation to the ports.

The mixer used for our test platform was an Analog Devices ADL5374, which allows for LO frequencies from 3–4 GHz, and has a modulation bandwidth of > 500 MHz. The I and Q ports are differential, and require a +0.5 VDC common mode bias. Additionally, the mixer requires a 5 V supply. Figure C.1 shows schematically the 5 V supply regulation and DC biases. In addition, the differential modulation inputs are converted to single ended through a balun transformer (Coilcraft WBC2-1TLB, 0.2–500 MHz). The DC bias is applied after the balun through an on-board bias-tee, which utilizes conical inductors rated for frequencies well beyond the 500 MHz bandwidth used in this particular application (Coilcraft BCS-652JLB). To keep the cancellation of LO leakage stable, a precision voltage reference (Linear Technology

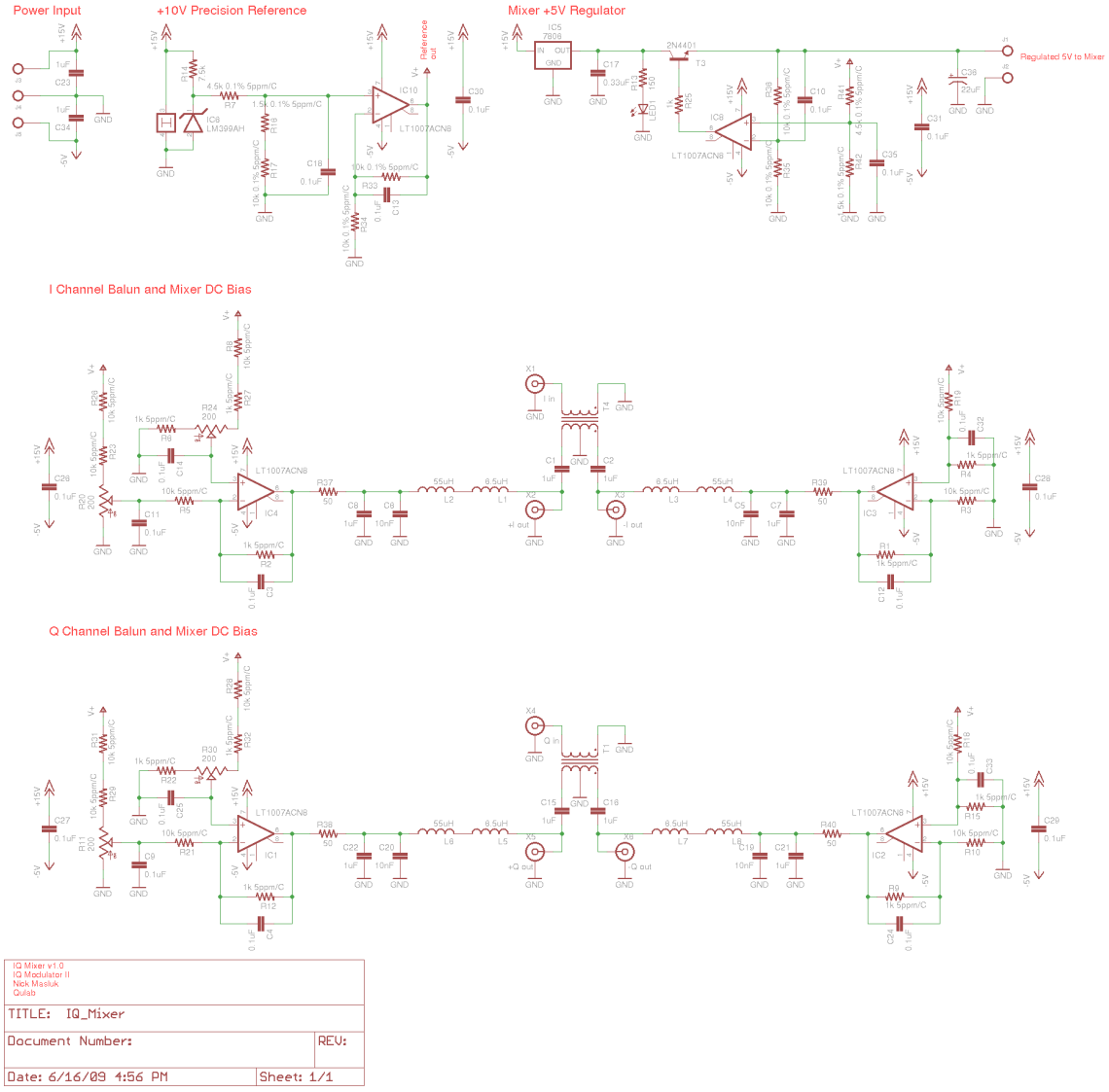

Figure C.1: Schematic for mixer balun and power supply with precision DC bias.

LM399AH) is used to stabilize the DC biases and supply voltage to the mixer. The DC bias is fixed to 0.5 V on one side of the differential bias lines to I and Q, while DC bias on the other differential line to I and Q is adjustable from 0.445–0.541 V through coarse and fine adjustment potentiometers (for the test setup used, coarse adjust is 4.1 mV/rev, fine adjust is 260 μV/rev, 22 revolutions each). Additional stability could be achieved by putting the mixer and associated components in a temperature stabilized environment. Temperature stabilization was not done, but where possible, low temperature coefficient components were used in critical areas. Suppression of the ADL5374 carrier is better than 80 dB, as shown in the data in Figure C.2. The location of the carrier cancellation can be tuned to any carrier frequency the ADL5374 supports by simultaneously adjusting the DC bias on the I and Q ports.

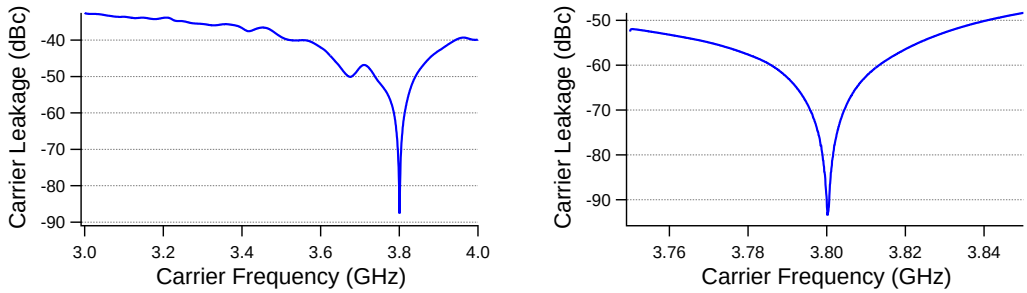

(a) Carrier suppression over mixer LO frequency range

(b) Closer view of suppression at 3.8 GHz

Figure C.2: Suppression of carrier with the DC bias of the I and Q ports of the ADL5374 mixer tuned to cancel 3.8 GHz. This allows for better than 80 dB of suppression of the carrier.

The modulated carrier from the ADL5374 must the be mixed up or down to the final desired frequency. An example layout is shown in Figure C.3, allowing for output frequencies from 6.15–6.25 GHz. The Spectrum mixer produces sidebands around 6.2 and 13.8 GHz, and the upper sideband is filtered away. A series of

filters along the chain eliminates unwanted harmonics and intermodulation products. Attenuators througout the chain reduce spurious signals due to imperfect matching between components. To compensate for loss along the chain, several amplifiers are used, with a 30 dBm power amplifier at the end. The actual implementation of this setup is shown in Figure C.4.

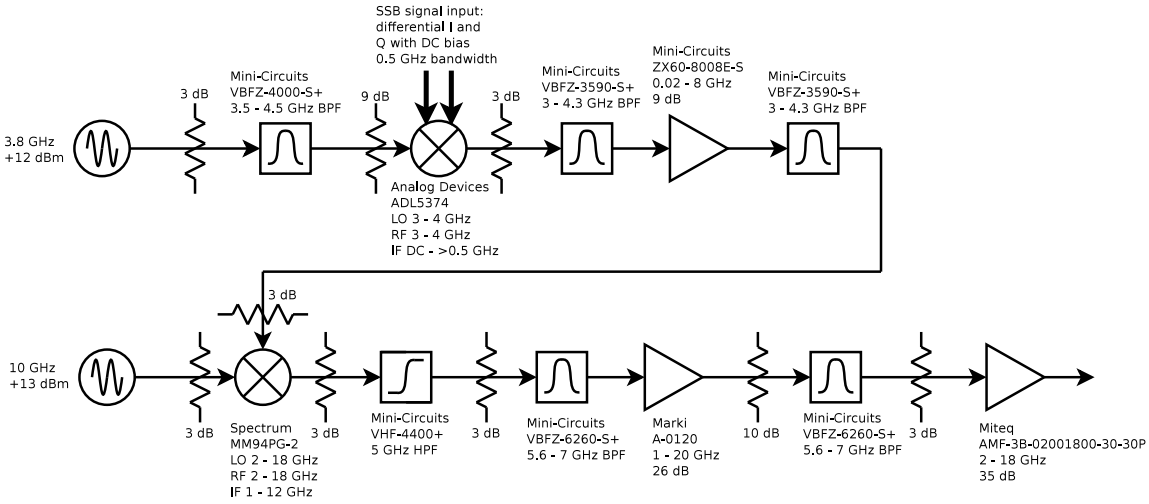

Figure C.3: Example IQ modulator layout.

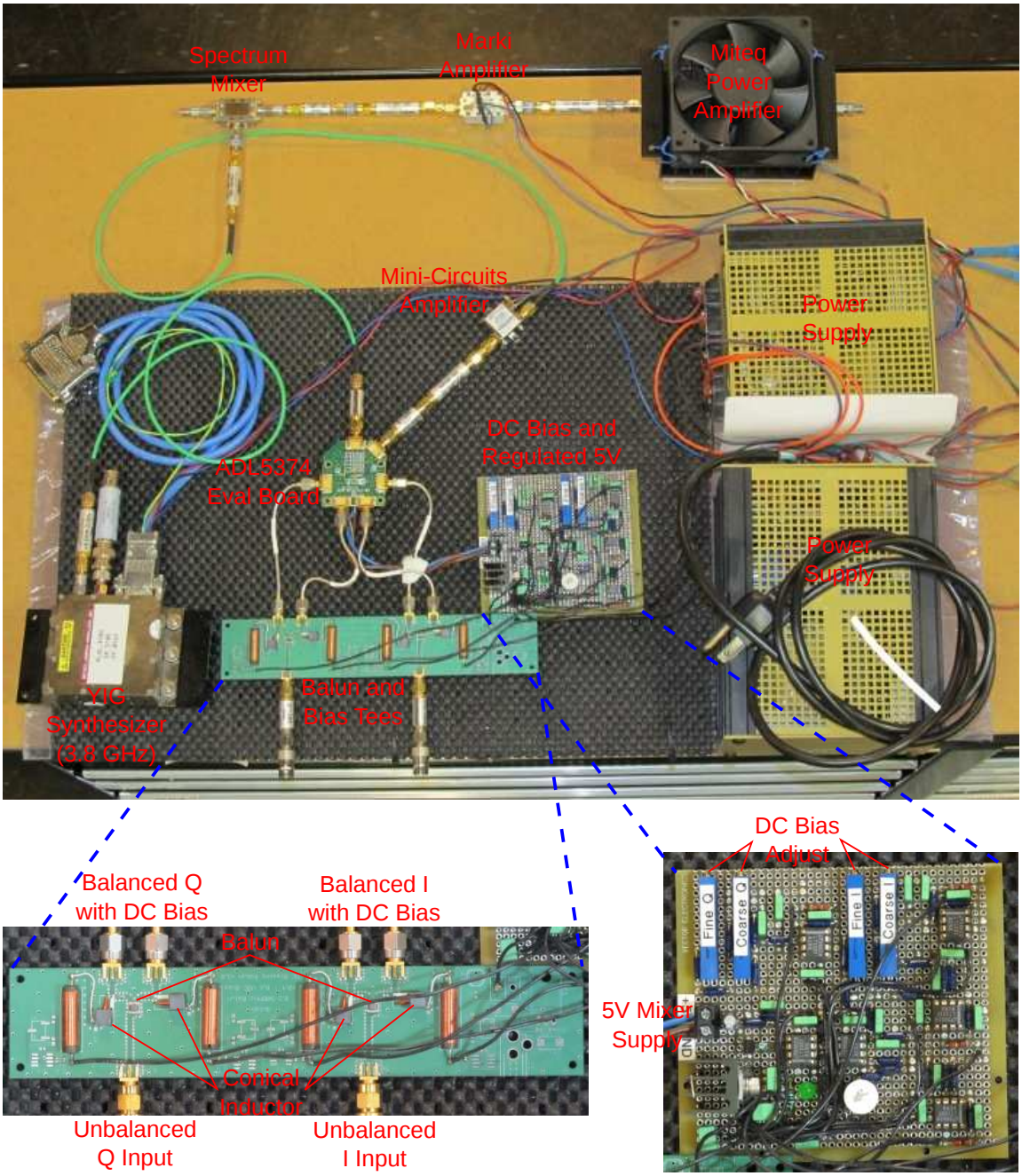

Figure C.4: Image of the IQ modulator setup diagrammed in Figure C.3.

Bibliography

[1] A. Wallraff, D. I. Schuster, A. Blais, L. Frunzio, J. Majer, M. H. Devoret, S. M. Girvin, and R. J. Schoelkopf. Approaching unit visibility for control of a superconducting qubit with dispersive readout. *Phys. Rev. Lett.*, 95:060501, Aug 2005. vii, 6

[2] J. Bylander, S. Gustavsson, F. Yan, F. Yoshihara, K. Harrabi, G. Fitch, D. G. Cory, Y. Nakamura, J.-S. Tsai, and W. D. Oliver. Noise spectroscopy through dynamical decoupling with a superconducting flux qubit. *Nat Phys*, 7(7):565–570, Jul 2011. viii, 10, 125

[3] M. Steffen, S. Kumar, D. P. DiVincenzo, J. R. Rozen, G. A. Keefe, M. B. Rothwell, and M. B. Ketchen. High-coherence hybrid superconducting qubit. *Phys. Rev. Lett.*, 105:100502, Sep 2010. viii, 3, 12, 13

[4] D. P. DiVincenzo. The Physical Implementation of Quantum Computation. *Fortschritte der Physik*, 48:771–783, 2000. 2

[5] B. Josephson. Possible new effects in superconductive tunnelling. *Physics Letters*, 1(7):251 – 253, 1962. 2

[6] B. D. Josephson. The discovery of tunnelling supercurrents. *Rev. Mod. Phys.*, 46:251–254, Apr 1974. 2

[7] J. E. Mooij and Y. V. Nazarov. Superconducting nanowires as quantum phase-slip junctions. *Nat Phys*, 2(3):169–172, Mar 2006. 2, 32

[8] V. Bouchiat, D. Vion, P. Joyez, D. Esteve, and M. H. Devoret. Quantum coherence with a single cooper pair. *Physica Scripta*, 1998(T76):165, 1998. 3, 5

[9] Y. Nakamura, Y. A. Pashkin, and J. S. Tsai. Coherent control of macroscopic quantum states in a single-cooper-pair box. *Nature*, 398(6730):786–788, Apr 1999. 3

[10] J. E. Mooij, T. P. Orlando, L. Levitov, L. Tian, C. H. van der Wal, and S. Lloyd. Josephson persistent-current qubit. *Science*, 285(5430):1036–1039, 1999. 3, 10

[11] D. Vion, A. Aassime, A. Cottet, P. Joyez, H. Pothier, C. Urbina, D. Esteve, and M. H. Devoret. Manipulating the quantum state of an electrical circuit. *Science*, 296(5569):886–889, 2002. 3, 7

[12] J. M. Martinis, S. Nam, J. Aumentado, and C. Urbina. Rabi oscillations in a large josephson-junction qubit. *Phys. Rev. Lett.*, 89:117901, Aug 2002. 3, 12

[13] J. Koch, T. M. Yu, J. Gambetta, A. A. Houck, D. I. Schuster, J. Majer, A. Blais, M. H. Devoret, S. M. Girvin, and R. J. Schoelkopf. Charge-insensitive qubit design derived from the cooper pair box. *Phys. Rev. A*, 76:042319, Oct 2007. 3, 7, 8

[14] V. E. Manucharyan, J. Koch, L. I. Glazman, and M. H. Devoret. Fluxonium: Single cooper-pair circuit free of charge offsets. *Science*, 326(5949):113–116, 2009. 3, 17

[15] M. H. Devoret, A. Wallraff, and J. M. Martinis. Superconducting Qubits: A Short Review. *eprint arXiv:cond-mat/0411174*, Nov. 2004. 4, 7

[16] J. Clarke and F. K. Wilhelm. Superconducting quantum bits. *Nature*, 453(7198):1031–1042, Jun 2008. 4

[17] Z. Kim, B. Suri, V. Zaretskey, S. Novikov, K. D. Osborn, A. Mizel, F. C. Wellstood, and B. S. Palmer. Decoupling a cooper-pair box to enhance the lifetime to 0.2 ms. *Phys. Rev. Lett.*, 106:120501, Mar 2011. 7, 24

[18] A. Cottet. *Implementation of a quantum bit in a superconducting circuit*. PhD thesis, Université Paris VI, Paris, France, 2002. 7

[19] A. Houck, J. Koch, M. Devoret, S. Girvin, and R. Schoelkopf. Life after charge noise: recent results with transmon qubits. *Quantum Information Processing*, 8:105–115, 2009. 10.1007/s11128-009-0100-6. 8

[20] J. A. Schreier, A. A. Houck, J. Koch, D. I. Schuster, B. R. Johnson, J. M. Chow, J. M. Gambetta, J. Majer, L. Frunzio, M. H. Devoret, S. M. Girvin, and R. J. Schoelkopf. Suppressing charge noise decoherence in superconducting charge qubits. *Phys. Rev. B*, 77:180502, May 2008. 8

[21] H. Paik, D. I. Schuster, L. S. Bishop, G. Kirchmair, G. Catelani, A. P. Sears, B. R. Johnson, M. J. Reagor, L. Frunzio, L. I. Glazman, S. M. Girvin, M. H. Devoret, and R. J. Schoelkopf. Observation of high coherence in josephson junction qubits measured in a three-dimensional circuit qed architecture. *Phys. Rev. Lett.*, 107:240501, Dec 2011. 9, 27

[22] C. Rigetti, S. Poletto, J. M. Gambetta, B. L. T. Plourde, J. M. Chow, A. D. Corcoles, J. A. Smolin, S. T. Merkel, J. R. Rozen, G. A. Keefe, M. B. Rothwell,

M. B. Ketchen, and M. Steffen. Superconducting qubit in waveguide cavity with coherence time approaching 0.1ms. *ArXiv e-prints*, Feb. 2012. 9

[23] J. Koch, V. Manucharyan, M. H. Devoret, and L. I. Glazman. Charging effects in the inductively shunted josephson junction. *Phys. Rev. Lett.*, 103:217004, Nov 2009. 9, 17

[24] I. Chiorescu, Y. Nakamura, C. J. P. M. Harmans, and J. E. Mooij. Coherent quantum dynamics of a superconducting flux qubit. *Science*, 299(5614):1869–1871, 2003. 10

[25] C. H. van der Wal, A. C. J. ter Haar, F. K. Wilhelm, R. N. Schouten, C. J. P. M. Harmans, T. P. Orlando, S. Lloyd, and J. E. Mooij. Quantum superposition of macroscopic persistent-current states. *Science*, 290(5492):773–777, 2000. 10

[26] J. R. Friedman, V. Patel, W. Chen, S. K. Tolpygo, and J. E. Lukens. Quantum superposition of distinct macroscopic states. *Nature*, 406(6791):43–46, Jul 2000. 11

[27] J. Martinis. Superconducting phase qubits. *Quantum Information Processing*, 8:81–103, 2009. 10.1007/s11128-009-0105-1. 11

[28] R. Ramos, M. Gubrud, A. Berkley, J. Anderson, C. Lobb, and F. Wellstood. Design for effective thermalization of junctions for quantum coherence. *Applied Superconductivity, IEEE Transactions on*, 11(1):998 –1001, mar 2001. 12

[29] K. Lang, S. Nam, J. Aumentado, C. Urbina, and J. Martinis. Banishing quasiparticles from josephson-junction qubits: why and how to do it. *Applied Superconductivity, IEEE Transactions on*, 13(2):989 – 993, june 2003. 12

[30] R. W. Simmonds, K. M. Lang, D. A. Hite, S. Nam, D. P. Pappas, and J. M. Martinis. Decoherence in josephson phase qubits from junction resonators. *Phys. Rev. Lett.*, 93:077003, Aug 2004. 12

[31] K. B. Cooper, M. Steffen, R. McDermott, R. W. Simmonds, S. Oh, D. A. Hite, D. P. Pappas, and J. M. Martinis. Observation of quantum oscillations between a josephson phase qubit and a microscopic resonator using fast readout. *Phys. Rev. Lett.*, 93:180401, Oct 2004. 12

[32] J. Q. You, X. Hu, S. Ashhab, and F. Nori. Low-decoherence flux qubit. *Phys. Rev. B*, 75:140515, Apr 2007. 12

[33] V. E. Manucharyan, N. A. Masluk, A. Kamal, J. Koch, L. I. Glazman, and M. H. Devoret. Evidence for coherent quantum phase slips across a josephson junction array. *Phys. Rev. B*, 85:024521, Jan 2012. 17, 38, 74

[34] V. E. Manucharyan. *Superinductance*. PhD thesis, Yale University, New Haven, Connecticut, 2011. 17, 32, 74

[35] E. Knill. Quantum computing with realistically noisy devices. *Nature*, 434(7029):39–44, Mar 2005. 18

[36] J. M. Chow, J. M. Gambetta, L. Tornberg, J. Koch, L. S. Bishop, A. A. Houck, B. R. Johnson, L. Frunzio, S. M. Girvin, and R. J. Schoelkopf. Randomized benchmarking and process tomography for gate errors in a solid-state qubit. *Phys. Rev. Lett.*, 102:090502, Mar 2009. 19

[37] J. M. Chow, L. DiCarlo, J. M. Gambetta, F. Motzoi, L. Frunzio, S. M. Girvin, and R. J. Schoelkopf. Optimized driving of superconducting artificial atoms for improved single-qubit gates. *Phys. Rev. A*, 82:040305, Oct 2010. 19

[38] J. M. Martinis, K. B. Cooper, R. McDermott, M. Steffen, M. Ansmann, K. D. Osborn, K. Cicak, S. Oh, D. P. Pappas, R. W. Simmonds, and C. C. Yu. Decoherence in josephson qubits from dielectric loss. *Phys. Rev. Lett.*, 95:210503, Nov 2005. 22

[39] Y. Shalibo, Y. Rofe, D. Shwa, F. Zeides, M. Neeley, J. M. Martinis, and N. Katz. Lifetime and coherence of two-level defects in a josephson junction. *Phys. Rev. Lett.*, 105:177001, Oct 2010. 22

[40] J. Gao, M. Daal, A. Vayonakis, S. Kumar, J. Zmuidzinas, B. Sadoulet, B. A. Mazin, P. K. Day, and H. G. Leduc. Experimental evidence for a surface distribution of two-level systems in superconducting lithographed microwave resonators. *Applied Physics Letters*, 92(15):152505, 2008. 22

[41] R. Barends, N. Vercruyssen, A. Endo, P. J. de Visser, T. Zijlstra, T. M. Klapwijk, P. Diener, S. J. C. Yates, and J. J. A. Baselmans. Minimal resonator loss for circuit quantum electrodynamics. *Applied Physics Letters*, 97(2):023508, 2010. 22

[42] M. Khalil, F. Wellstood, and K. Osborn. Loss dependence on geometry and applied power in superconducting coplanar resonators. *Applied Superconductivity, IEEE Transactions on*, 21(3):879 –882, june 2011. 22

[43] K. Geerlings, S. Shankar, E. Edwards, L. Frunzio, R. J. Schoelkopf, and M. H. Devoret. Improving the quality factor of microwave compact resonators by optimizing their geometrical parameters. *Applied Physics Letters*, 100(19):192601, 2012. 22, 36

[44] G. J. Dolan. Offset masks for lift-off photoprocessing. *Applied Physics Letters*, 31(5):337–339, 1977. 24, 61, 88

[45] C. T. Rigetti. *Quantum Gates for Superconducting Qubits*. PhD thesis, Yale University, New Haven, Connecticut, 2009. 25, 61, 92, 168

[46] F. Lecocq, I. M. Pop, Z. Peng, I. Matei, T. Crozes, T. Fournier, C. Naud, W. Guichard, and O. Buisson. Junction fabrication by shadow evaporation without a suspended bridge. *Nanotechnology*, 22(31):315302, 2011. 25, 61, 92

[47] A. A. Houck, J. A. Schreier, B. R. Johnson, J. M. Chow, J. Koch, J. M. Gambetta, D. I. Schuster, L. Frunzio, M. H. Devoret, S. M. Girvin, and R. J. Schoelkopf. Controlling the spontaneous emission of a superconducting transmon qubit. *Phys. Rev. Lett.*, 101:080502, Aug 2008. 26

[48] I. Pop. private communication, 2012. 27

[49] H. Paik. private communication, 2012. 27

[50] J. M. Gambetta. private communication, 2012. 27

[51] A. Bezryadin, C. N. Lau, and M. Tinkham. Quantum suppression of superconductivity in ultrathin nanowires. *Nature*, 404(6781):971–974, Apr 2000. 32

[52] M. T. Bell, I. A. Sadovskyy, L. B. Ioffe, A. Y. Kitaev, and M. E. Gershenson. Quantum superinductor with tunable nonlinearity. *Phys. Rev. Lett.*, 109:137003, Sep 2012. 32

[53] L. S. Kuzmin and D. B. Haviland. Observation of the bloch oscillations in an ultrasmall josephson junction. *Phys. Rev. Lett.*, 67:2890–2893, Nov 1991. 32

[54] D. Haviland, L. Kuzmin, P. Delsing, K. Likharev, and T. Claeson. Experimental evidence for the coulomb blockade of cooper pair tunneling and bloch

oscillations in single josephson junctions. *Zeitschrift fr Physik B Condensed Matter*, 85:339–347, 1991. 32

[55] W. Guichard and F. W. J. Hekking. Phase-charge duality in josephson junction circuits: Role of inertia and effect of microwave irradiation. *Phys. Rev. B*, 81:064508, Feb 2010. 32

[56] M. A. Castellanos-Beltran and K. W. Lehnert. Widely tunable parametric amplifier based on a superconducting quantum interference device array resonator. *Applied Physics Letters*, 91(8):083509, 2007. 32

[57] I. M. Pop, B. Douçot, L. Ioffe, I. Protopopov, F. Lecocq, I. Matei, O. Buisson, and W. Guichard. Experimental demonstration of aharonov-casher interference in a josephson junction circuit. *Phys. Rev. B*, 85:094503, Mar 2012. 32

[58] S. V. Lotkhov, S. A. Bogoslovsky, A. B. Zorin, and J. Niemeyer. Cooper pair cotunneling in single charge transistors with dissipative electromagnetic environment. *Phys. Rev. Lett.*, 91:197002, Nov 2003. 32

[59] S. Corlevi, W. Guichard, F. W. J. Hekking, and D. B. Haviland. Phase-charge duality of a josephson junction in a fluctuating electromagnetic environment. *Phys. Rev. Lett.*, 97:096802, Aug 2006. 32

[60] E. Chow, P. Delsing, and D. B. Haviland. Length-scale dependence of the superconductor-to-insulator quantum phase transition in one dimension. *Phys. Rev. Lett.*, 81:204–207, Jul 1998. 32

[61] W. Kuo and C. D. Chen. Scaling analysis of magnetic-field-tuned phase transitions in one-dimensional josephson junction arrays. *Phys. Rev. Lett.*, 87:186804, Oct 2001. 32

[62] Y. Takahide, H. Miyazaki, and Y. Ootuka. Superconductor-insulator crossover in josephson junction arrays due to reduction from two to one dimension. *Phys. Rev. B*, 73:224503, Jun 2006. 32

[63] A. Palacios-Laloy, F. Nguyen, F. Mallet, P. Bertet, D. Vion, and D. Esteve. Tunable resonators for quantum circuits. *Journal of Low Temperature Physics*, 151:1034–1042, 2008. 10.1007/s10909-008-9774-x. 32

[64] I. M. Pop, I. Protopopov, F. Lecocq, Z. Peng, B. Pannetier, O. Buisson, and W. Guichard. Measurement of the effect of quantum phase slips in a josephson junction chain. *Nat Phys*, 6(8):589–592, Aug 2010. 38

[65] S. Gladchenko, D. Olaya, E. Dupont-Ferrier, B. Doucot, L. B. Ioffe, and M. E. Gershenson. Superconducting nanocircuits for topologically protected qubits. *Nat Phys*, 5(1):48–53, Jan 2009. 40

[66] R. Shankar. *Principles of Quantum Mechanics*. Springer, 1994. 42

[67] I. Gradshteyn, I. Ryzhik, A. Jeffrey, and D. Zwillinger. *Table of Integrals, Series, And Products*. Academic Press. Academic, 2007. 43

[68] D. Griffiths. *Introduction to quantum mechanics*. Pearson Prentice Hall, 2005. 44

[69] R. J. Schoelkopf, A. A. Clerk, S. M. Girvin, K. W. Lehnert, and M. H. Devoret. Qubits as Spectrometers of Quantum Noise. *eprint arXiv:cond-mat/0210247*, Oct. 2002. 66

[70] E. M. Purcell. Proceedings of the american physical society. *Phys. Rev.*, 69:681, Jun 1946. 66

[71] D. Pozar. *Microwave Engineering*. John Wiley & Sons, 2004. 68

[72] G. Catelani, J. Koch, L. Frunzio, R. J. Schoelkopf, M. H. Devoret, and L. I. Glazman. Quasiparticle relaxation of superconducting qubits in the presence of flux. *Phys. Rev. Lett.*, 106:077002, Feb 2011. 71

[73] Y. Aharonov and A. Casher. Topological quantum effects for neutral particles. *Phys. Rev. Lett.*, 53:319–321, Jul 1984. 74

[74] K. A. Matveev, A. I. Larkin, and L. I. Glazman. Persistent current in superconducting nanorings. *Phys. Rev. Lett.*, 89:096802, Aug 2002. 74

[75] F. C. Wellstood, C. Urbina, and J. Clarke. Low-frequency noise in dc superconducting quantum interference devices below 1 k. *Applied Physics Letters*, 50(12):772–774, 1987. 75

[76] I. M. Pop. *Quantum Phase-Slips in Josephson Junction Chains*. PhD thesis, Université de Grenoble, Grenoble, France, 2011. 76

[77] A. D. O'Connell, M. Ansmann, R. C. Bialczak, M. Hofheinz, N. Katz, E. Lucero, C. McKenney, M. Neeley, H. Wang, E. M. Weig, A. N. Cleland, and J. M. Martinis. Microwave dielectric loss at single photon energies and millikelvin temperatures. *Applied Physics Letters*, 92(11):112903, 2008. 91

[78] S. Wartenberg and Q. H. Liu. A coaxial-to-microstrip transition for multilayer substrates. *Microwave Theory and Techniques, IEEE Transactions on*, 52(2):584 – 588, feb. 2004. 94

[79] J.-E. Roh, J.-W. Li, B.-C. Ahn, C.-S. Park, and E.-J. Cha. Novel approach to optimizing a broadband right-angle coaxial-to-microstrip transition. *Microwave and Optical Technology Letters*, 49(2):451–456, 2007. 94

[80] M. Morgan and S. Weinreb. A millimeter-wave perpendicular coax-to-microstrip transition. In *Microwave Symposium Digest, 2002 IEEE MTT-S International*, volume 2, pages 817 –820, 2002. 94

[81] D. F. Santavicca and D. E. Prober. Impedance-matched low-pass stripline filters. *Measurement Science and Technology*, 19(8):087001, 2008. 108

[82] A. D. Corcoles, J. M. Chow, J. M. Gambetta, C. Rigetti, J. R. Rozen, G. A. Keefe, M. B. Rothwell, M. B. Ketchen, and M. Steffen. Protecting superconducting qubits from radiation. *Applied Physics Letters*, 99(18):181906, 2011. 108

[83] J. M. Martinis, M. H. Devoret, and J. Clarke. Experimental tests for the quantum behavior of a macroscopic degree of freedom: The phase difference across a josephson junction. *Phys. Rev. B*, 35:4682–4698, Apr 1987. 110

[84] A. Fukushima, A. Sato, A. Iwasa, Y. Nakamura, T. Komatsuzaki, and Y. Sakamoto. Attenuation of microwave filters for single-electron tunneling experiments. *Instrumentation and Measurement, IEEE Transactions on*, 46(2):289 –293, apr 1997. 110

[85] P. Jarillo-Herrero, J. A. van Dam, and L. P. Kouwenhoven. Quantum supercurrent transistors in carbon nanotubes. *Nature*, 439(7079):953 – 956, Feb 2006. 110

[86] F. P. Milliken, J. R. Rozen, G. A. Keefe, and R. H. Koch. 50 omega characteristic impedance low-pass metal powder filters. *Review of Scientific Instruments*, 78(2):024701, 2007. 110

[87] J. J. A. Baselmans and S. J. C. Yates. Long quasiparticle lifetime in aluminum microwave kinetic inductance detectors using coaxial stray light filters. *AIP Conference Proceedings*, 1185(1):160–163, 2009. 110

[88] R. Barends, J. Wenner, M. Lenander, Y. Chen, R. C. Bialczak, J. Kelly, E. Lucero, P. O'Malley, M. Mariantoni, D. Sank, H. Wang, T. C. White, Y. Yin, J. Zhao, A. N. Cleland, J. M. Martinis, and J. J. A. Baselmans. Minimizing quasiparticle generation from stray infrared light in superconducting quantum circuits. *Applied Physics Letters*, 99(11):113507, 2011. 110, 114

[89] H. A. Haus. Waveguides and resonators. In *Electromagnetic Noise and Quantum Optical Measurements*, pages 84–88. Springer, 2000. 118

[90] A. Abragam. *The Principles of Nuclear Magnetism*. International Series of Monographs on Physics. Clarendon Press, 1961. 121

[91] C. Slichter. *Principles of Magnetic Resonance*. Springer Series in Solid-State Sciences. Springer, 1990. 121

[92] I. I. Rabi. Space quantization in a gyrating magnetic field. *Phys. Rev.*, 51:652–654, Apr 1937. 122

[93] N. F. Ramsey. A molecular beam resonance method with separated oscillating fields. *Phys. Rev.*, 78:695–699, Jun 1950. 123

[94] Y. Makhlin and A. Shnirman. Dephasing of solid-state qubits at optimal points. *Phys. Rev. Lett.*, 92:178301, Apr 2004. 123

[95] G. Ithier, E. Collin, P. Joyez, P. J. Meeson, D. Vion, D. Esteve, F. Chiarello, A. Shnirman, Y. Makhlin, J. Schriefl, and G. Schön. Decoherence in a superconducting quantum bit circuit. *Phys. Rev. B*, 72:134519, Oct 2005. 123

[96] E. L. Hahn. Spin echoes. *Phys. Rev.*, 80:580–594, Nov 1950. 124

[97] D. I. Schuster, A. Wallraff, A. Blais, L. Frunzio, R.-S. Huang, J. Majer, S. M. Girvin, and R. J. Schoelkopf. ac stark shift and dephasing of a superconducting qubit strongly coupled to a cavity field. *Phys. Rev. Lett.*, 94:123602, Mar 2005. 126

[98] H. G. Dehmelt. Entropy reduction by motional sideband excitation. *Nature*, 262(5571):777–777, Aug 1976. 128

[99] R. Van Dyck, P. Ekstrom, and H. Dehmelt. Axial, magnetron, cyclotron and spin-cyclotron-beat frequencies measured on single electron almost at rest in free space (geonium). *Nature*, 262(5571):776–777, Aug 1976. 128

[100] D. J. Wineland and W. M. Itano. Laser cooling of atoms. *Phys. Rev. A*, 20:1521–1540, Oct 1979. 128

[101] S. O. Valenzuela, W. D. Oliver, D. M. Berns, K. K. Berggren, L. S. Levitov, and T. P. Orlando. Microwave-induced cooling of a superconducting qubit. *Science*, 314(5805):1589–1592, 2006. 129

[102] J. Gambetta, W. A. Braff, A. Wallraff, S. M. Girvin, and R. J. Schoelkopf. Protocols for optimal readout of qubits using a continuous quantum nondemolition measurement. *Phys. Rev. A*, 76:012325, Jul 2007. 131

[103] S. Haroche and J. Raimond. *Exploring the Quantum:Atoms, Cavities, and Photons: Atoms, Cavities, and Photons*. Oxford graduate texts in mathematics. OUP Oxford, 2006. 132

[104] R. Vijay, D. H. Slichter, and I. Siddiqi. Observation of quantum jumps in a superconducting artificial atom. *Phys. Rev. Lett.*, 106:110502, Mar 2011. 132

[105] B. Abdo, F. Schackert, M. Hatridge, C. Rigetti, and M. Devoret. Josephson amplifier for qubit readout. *Applied Physics Letters*, 99(16):162506, 2011. 132

[106] K. Bergmann, H. Theuer, and B. W. Shore. Coherent population transfer among quantum states of atoms and molecules. *Rev. Mod. Phys.*, 70:1003–1025, Jul 1998. 145

[107] V. Romanenko and L. Yatsenko. Adiabatic population transfer in the three-level -system: two-photon lineshape. *Optics Communications*, 140(46):231 – 236, 1997. 145